DI 106675
Drs. G.H. van der KOLFF
EERSTE MEDEWERKER
BCRS PROGRAMMABUREAU

USP-2
99-36

MERILAND: MERIS potential for land applications

F.D. van der Meer
J.G.P.W. Clevers
S.M. de Jong
W.H. Bakker
G.F. Epema
A.K. Skidmore
K. Scholte

BCRS 99–36 MD

MISSIE REMOTE SENSING

31 DEC 2002

Informatiecentrum
Rijkswaterstaat
Meetkundige Dienst

MERILAND: MERIS potential for land applications

F.D. van der Meer
ITC
J.G.P.W. Clevers
Wageningen University
S.M. de Jong
Utrecht University
W.H. Bakker
ITC
G.F. Epema
Wageningen University
A.K. Skidmore
K. Scholte
ITC

USP-2 report 99-36
USP-2 project 3.1/AP-06

ISBN 90 54 11 307 3

June 2000

This report describes a project carried out in the framework of the National User Support Programme (USP-2) under responsibility of the Netherlands Remote Sensing Board (BCRS) and the Space Research Organization Netherlands (SRON)

Hyperspectral remote sensing is

the acquisition of images in hundreds of registered, contiguous spectral bands such that for each picture element of an image it is possible to derive a complete radiance or reflectance spectrum

with the objective

to measure quantitatively the components of the Earth System from calibrated spectra acquired as images for scientific research and applications. Thus we are interest in measuring physical quantities at the Earth surface such as upwelling radiance, emissivity, temperature and reflectance.

A.F.H. Goetz

ACKNOWLEDGEMENTS **6**

ABSTRACT **7**

SUMMARY **8**

CHAPTER 1 ..... **11**

MERILAND: MERIS' POTENTIAL FOR LAND APPLICATIONS **11**

1.1 INTRODUCTION 11
1.2 MERILAND AIMS AND OBJECTIVES 11

CHAPTER 2 ..... **13**

ESA'S MEDIUM RESOLUTION IMAGING SPECTROMETER **13**

2.1 INTRODUCTION 13
2.2 THE MERIS INSTRUMENT 15
2.2.1 Scanning *15*
2.2.2 Calibration *15*
2.2.3 Spatial characteristics *16*
2.2.4 Spectral characteristics *16*
2.3. MERIS DATA PRODUCTS 17

CHAPTER 3 ..... **19**

MERIS DATA SIMULATION **19**

3.1 INTRODUCTION 19
3.2 DATASETS AVAILABLE 19
3.2.1 GERIS *20*
3.2.2 DAIS-7915 ..... *21*
3.2.3 CASI *22*
3.2.4 AVIRIS *23*
3.3 MULTI-CRITERIA ANALYSIS (MCA) 24
3.4 SIMULATION PROCEDURE 25

CHAPTER 4 ..... **29**

MERISPEC: A SPECTRAL DATABASE FOR MERIS **29**

4.1 INTRODUCTION 29
4.2 MERILAND: THE FIELD CAMPAIGN 1998 31
4.3 MERISPEC CDROM INSTALLATION 33

CHAPTER 5 ..... **34**

MERIS' POTENTIAL FOR MAPPING (SOIL) MINERALOGY **34**

5.1 INTRODUCTION 34
5.2 MERIS MINERAL INDEX 34
MINERAL 36
5.3 MERIS DATA SIMULATION FOR MINERAL MAPPING; PRACTICAL APPLICATION 36
5.4 SURFACE (SOIL) MINERALOGY MAPPING USING CCSM 40
5.5 VALIDATION OF SURFACE MINERALOGY MAPS 41
5.6 RESULTS 42
5.7 CONCLUSIONS 43

CHAPTER 6 ..... **44**

VEGETATION INDICES FOR SIMULATED MERIS IMAGES **44**

6.1 INTRODUCTION 44
6.2 DATA SETS AND METHODOLOGY 46
6.3 VEGETATION INDEX 49
6.4 BIOMASS ESTIMATES 50
6.5 RESULTS 51
6.6 CONCLUSIONS 52

CHAPTER 7 54

THE RED EDGE INDEX USING THE MERIS STANDARD BAND SETTING 54

7.1 INTRODUCTION 54
7.2 METHODOLOGY FOR DETERMINING THE RED EDGE INDEX 55
7.3 DATA SETS 57
7.4 RESULTS AND DISCUSSION 58
7.4.1 Comparison of the linear method with the Lagrangian technique 58
7.4.2 Red edge index simulation with MERIS 60
7.4.3 Upscaling to the MERIS resolution 62
7.5 CONCLUSIONS 64

CHAPTER 8 67

SCALING TO THE MERIS RESOLUTION: MAPPING ACCURACY AND SPATIAL VARIABILITY 67

8.1 INTRODUCTION 67
8.2 MERIS IMAGE PRODUCTS 68
8.3 SPATIAL VARIABILITY 70
8.4 MAPPING ACCURACY: OPTIMAL SAMPLING SIZES. 72
8.5 CONCLUSIONS 73

CHAPTER 9 75

FINAL CONCLUSIONS AND RECOMMENDATIONS FOR FURTHER STUDIES 75

9.1 INTRODUCTION 75
9.2 FINAL CONCLUSIONS 75
9.3 OTHER RELATED SATELLITE MISSIONS 76
9.4 RECOMMENDATIONS FOR FURTHER STUDIES 78

ABBREVIATIONS AND ACRONYMS 79

SYMBOLS USED 81

REFERENCES 83

BIBLIOGRAPHY 92

APPENDIX 1 94

MERISPEC SPECTRAL DATABASE 94

A1.1 STRUCTURE 94
A1.1.1 The logical structure 94
A1.1.2 The directory structure 94
A1.2. THE FOREST GROUP 94
A1.2.1 The 1606 Theme 94
A1.2.2 The 1906 Theme 95
A1.3. THE GARRIGUE GROUP 95
A1.3.1 The 1806 Theme 95
A1.3.2 The 1906 theme 96
A1.3.3 The 2106 Theme 96
A1.3.4 The 2306 Theme 96
A1.4 THE MAQUIS GROUP 98

A1.4.1 The 1706 Theme *98*
A1.4.2 The 2106 Theme *98*

APPENDIX 2 ..... **99**

GEOMETRIC CORRECTION OF DAIS-7915 DATA **99**

A2.1 INTRODUCTION 99
A2.2 THEORY AND METHODS 100
A2.2.1 Geometric correction; current practice *100*
A2.2.2 Geostatistical approach *101*
A2.3 CONCLUSIONS 106

APPENDIX 3 ..... **108**

COLOR PLATES **108**

Acknowledgements

This research is conducted as part of the MERILand project (http://www.itc/nl/~MERIS/) partially funded by the Netherlands Remote Sensing Board (BCRS) under contract 3.1/AP-06. Advice by Mike Rast and Steve Delwart (ESA-ESTEC) and Ingrid Janssen (BCRS) was highly appreciated. HyMAP data was acquired during the HyEUROPE campaign under funding of the INCO-ELANEM project. We are grateful to Prof. Andrea Fabbri for permitting us to use the HyMAP data. Dr. Rolf Richter (DLR) is thanked for atmospheric correction of the HyMAP data using ATCOR4, Dr. Peter Strobl (DLR) performed the system correction of the data.

DAIS data over Le Peyne were kindly provided under the DEMON project. We thank Stefan Sommer and Joachim Hill for their assistance. Andreas Mueller, Peter Strobl, Andrea Haushold, Rolf Richter, Franz Lanzl and many other from DLR are thanked for their excellent work during the 1996-1998 DAIS LSF campaigns and the 1999 HyEUROPE campaign providing data that made this work possible.

We thank Stefan Sommer, Helen Preissler, Herve Bohbot of JRC for excellent collaboration on the MERISPEC spectral database.

Prof. Dr A. Stein, Dr J. Loedeman, Dr S. de Bruin and Drs J. Hendrikse reviewed an earlier manuscript of the geometric correction procedure (appendix 2).

We thank the "programmabureau" BCRS for their support in the project execution, for assistance in establishing contacts and in providing valuable information on MERIS in general and ESA activities. The critical review of the draft version of this manuscript by Ir. I.M.H. Janssen (BCRS) is highly appreciated.

Abstract

The use of ESA's Medium Resolution Imaging Spectrometer (MERIS) for various land applications has been investigated in this project. MERIS will provide 15 bands (although the system can be fully programmed) in the 400-900 nm. range at 300m resolution over land. The main objectives are directed toward oceanography, for land various vegetation products are envisaged. Existing airborne imaging spectrometer data sets including HyMAP (the Hyperspectral Mapper) data, DAIS (the Digital Airborne Imaging Spectrometer) and GERIS (the GER 63 channel imaging spectrometer) were used to simulate both spatially as well as spectrally the MERIS band set. None of these airborne sensors matches the spectral and radiometric characteristics of MERIS, hence the simulated image data sets provide a poor representation of the expected MERIS radiometric characteristics. The spatial characteristics can be optimally simulated. Furthermore, the study of simulation provides insights into up- and downscaling to the MERIS resolution. A MERIS spectral library containing field spectral measurements (at full and MERIS spectral resolution) of relevant ground cover has been compiled (MERISPEC) within the framework of the project. MERIS potential for land applications including soil mineralogy, vegetation indices and red edge positioning were examined. Soil mineralogical mapping, not a MERIS science objective, can yield relative abundance estimates of iron content and highlight iron bearing soils from non-iron bearing soils. No detailed mineralogical or soil constituent mapping can be done using MERIS. A large number of standard vegetation indices including those that correct for soil background effects were prototyped using the MERIS specifications. These indices, although they differ amongst eachother, provide relatively constant estimates at varying spatial resolutions from 12m. up to the MERIS spatial resolution. A comparison of the MERIS NDVI and the DAIS (airborne equivalent) NDVI shows a good correlation. Comparisons of the MERIS NDVI to above ground biomass measured at field scale allows broad ground cover types such as garrigue, maquis and mixed oak forests to be classified, however at a relatively low accuracy. A red edge positioning algorithm has been developed for MERIS using PROSPECT-SAIL simulations for a canopy with a varying leaf chlorophyll content as input and using Airborne Visible/Infrared Imaging Spectrometer data (AVIRIS). Both experiments show that the MERIS standard band set can be used for deriving red edge index values. When evaluating the relation between optimal spatial sampling and spatial resolution for various land products such as soil type and vegetation it is concluded that the optimal spatial resolution for characterizing these ground cover types is at smaller spatial resolutions than the 300m. provided by MERIS. However it should be noted that statistically optimal does not necessary has to be the mission goal of the instrument.

Summary

When light interacts with materials of interest, light of a certain wavelength is preferentially absorbed while at other wavelengths light is transmitted in the substance. Electronic transition- and vibrational processes determine the amount of absorbance and reflectance of a sample resulting in absorption features in the visible to short-wave infrared wavelength region of the electromagnetic (EM) spectrum. The shape (e.g., their position, depth, width etc) of diagnostic absorption features, that are typically 20 to 40 nanometer wide, is determined by the crystallography and chemical composition of the material. Thus reflectance spectra provide valuable information on the Earth surface composition. Currently operational Earth Observation Satellites acquire broad spectral information, which does not allow retrieving spectroscopic information.

Imaging spectrometry, is the acquisition of image data in many contiguous spectral bands, with the aim of producing laboratory-like reflectance spectra for each pixel in the scene which can be directly compared either qualitatively or quantitatively with spectra of known materials measured in the field or laboratory.

Currently available instruments are airborne, however within the lifetime of the proposal several spaceborne mission will be executed providing satellite-based spectroscopic information including NASA's ASTER on EOS-1/TERRA, NASA's Hyperion part of the New Millennium Program and ESA's MERIS on ENVISAT-1.

The main objective of the ENVISAT programme is to endow Europe with an enhanced capability for the observation of Earth from Space, with the aim of further increasing the capacity of Participating States to take part in the studying and monitoring of the Earth and its environment. Its primary objectives are:

- to provide for continuity of the observations started with the ERS satellites, including those obtained from radar-based observations;
- to provide for enhancement of the ERS missions, notably the ocean and ice mission
- to extend the range of parameters observed, to meet the need to increase knowledge of the factors determining the environment;
- to make a significant contribution to environmental studies, notably in the areas of atmospheric chemistry and ocean studies (including marine biology);

coupled with two linked secondary objectives:

- to allow more effective monitoring and management of the Earth's resources;
- to better understand solid Earth processes

MERIS is the Medium Resolution Imaging Spectrometer, one of the payloads of ENVISAT. MERIS' mission over land is dedicated to land surface processes: global scale vegetation monitoring, distribution, extent and condition. The primary mission goal, however, is bio-optical oceanography: assessment of surface optical properties and water constituents leading to phytoplankton biomass and productivity via the estimation of pigment concentrations. Secondary mission goals include atmospheric investigations of cloud and aerosol parameters and global scale monitoring of vegetation. Land applications form a modest contribution to the mission goal, although MERIS has large potential for such investigations. The MERILAND project aims at gaining insight in the possibilities that MERIS may offer for land applications and the development of algorithms that may lead to standard product formulation:

- To develop a database of spectral signatures of earth materials with MERIS specification,
- To develop simulated MERIS data sets for various land applications,
- To study MERIS simulated data and the potential for quantified land observation,
- To develop algorithms for information extraction from MERIS data,

- To develop an infrastructure for easy access to the simulated data and algorithms.

MERIS is a 15 band programmable imaging spectrometer, which includes the capability of changing the band position and bandwidths throughout its lifetime. It is designed to acquire data at variable bandwidth between 1.25 and 30 nm over the spectral range 390 – 1040 nm. Within the framework of the MERILAND project, algorithms for simulating MERIS data from existing airborne imaging spectrometer data sets were developed. Test sites included Le Peyne, southern France (DAIS data), Tabernas, southern Spain (HyMAP and DAIS data), Flevoland, the Netherlands (AVIRIS data) and Almaden, middle Spain (GERIS data). Using the simulated MERIS image data sets, algorithms and processing strategies were developed for the analysis of the data. We focused on the following issues: mineralogical mapping, MERIS vegetation indices, red edge detection and issue of scale. Contemporaneously, a interactive spectral data base for MERIS spectra of land targets typical for the Mediterranean environment was established.

MERIS data was simulated using existing airborne imaging spectrometer data sets of various systems (AVIRIS, DAIS, GERIS, HyMAP) over several test areas (Flevoland, La Peyne, Almeria) for different applications (soil properties, vegetation monitoring, biophysical parametrization, upscaling). We followed an essentially two-step procedure. Step 1 is the spectral resampling using convolution over the sensor's spectral response function (SRF) for each band in case of oversampled input data or band matching in case of undersampled input data. Step 2 being the spatial resampling using spatial degradation using the sensor point spread (response) function (PSF) for each band. Field spectral and ancillary data were collected over many sites including the La Peyne study area and a database of spectroscopic measurements was constructed: the MERISPEC interactive database and spectral library. To investigate the potential of MERIS for mapping soil mineralogy, HyMAP from Almeria (Spain) was resampled to MERIS and various minerals were mapped using the cross correlogram spectral matching technique. It was concluded that MERIS' can identify a suite of minerals with absorption features in the visible and near-infrared part of the wavelength spectrum. However, most of the minerals having a high MERIS mineral index were found to be ore minerals (or related alteration products) that are unlikely to be "seen" at the resolution of MERIS. Comparison of the mapping with the "true" mineral maps for hematite and goethite shows that the prediction accuracy decreases rapidly when increasing the spatial resolution. This may be attributed to the mixed nature of the pixels at higher field-of-views. The optimal sampling size in case of goethite was found to be between 20 and 30 m. while for the hematite a value of less than 10m. was obtained. This is related to the nature of occurrence of the minerals: goethite occurs as large, rather homogenous caps while the hematite occurs in a more disseminated manner. Simulated MERIS data from the La Peyne area was used to test the capabilities of the sensor to monitor vegetation (using vegetation indices) and to produce biomass estimates. When using various vegetation indices these produced vary stable results at various spatial resolutions using the MERIS band set, indicating the potential of the sensor for monitoring vegetation. Biomass estimates were less successful. As the correlation between biomass and NDVI for DAIS is modest, for MERIS imagery hardly a correlation is found ($r = 0.2$).

Synthetic data from the SAIL and PROSPECT model and AVIRIS data from Flevoland were used to assess the potential of MERIS to model the vegetation red-edge as a indicator of biophysical state of vegetation. Both data sets were found to exhibit more than one unique maximum in the first derivative reflectance spectrum, whereby different maximal values become dominant with changing LAI and with changing leaf chlorophyll content. These two variables are the main variables determining the position of the red edge. As a result, the maximum second derivative is not useful as a measure for the red edge index. Results show a linear relationship between the linear "Baret-Guyot" method of red-edge positioning using bands at about 700 and 740 nm. and the MERIS bands, albeit that it not coincides with the 1:1 line. Thus an instrument-specific red edge indices is proposed. For MERIS, the linear relationship may be used for translating red edge index values obtained with one method (using the MERIS bands) into values obtained with the other method (based on bands at 700 and 740 nm.). Deviations occur at high red edge index values matching

vegetation with a high chlorophyll content and with high LAI values. To cope with this, a non-linear function might be fitted. Optimalisation of sampling sizes is addressed using a geostatistical analysis, using variogram surfaces and fractional abundance estimates, from simulated MERIS data at various spatial scales. This allows gaining insight into the nature of the data and its spatial dependency showing, however, little noticeable changes even at a sub-pixel level. When evaluating mapping accuracy clearly different optimal sampling sizes are found for the different end members. For end-members derived, the optimal sampling size corresponding to the peak in the local variance curve is found at finer resolution than the pixel size proposed for MERIS.

Various recommendations for further studies arise from the project including:

- study of downscaling: translation and particularly linking of NOAA-AVHRR type of data to the MERIS scale level
- extrapolation of high spatial resolution classification results to larger areas using medium resolution data and co-kriging techniques.

Chapter 1

MERILand: MERIS' potential for land applications

1.1 Introduction

Quoting from ESA (1997) "the main objective of the ENVISAT programme is to endow Europe with an enhanced capability for the observation of Earth from Space, with the aim of further increasing the capacity of Participating States to take part in the studying and monitoring of the Earth and its environment. Its primary objectives are:

- to provide for continuity of the observations started with the ERS satellites, including those obtained from radar-based observations;
- to provide for enhancement of the ERS missions, notably the ocean and ice mission
- to extend the range of parameters observed, to meet the need to increase knowledge of the factors determining the environment;
- to make a significant contribution to environmental studies, notably in the areas of atmospheric chemistry and ocean studies (including marine biology);

coupled with two linked secondary objectives:

- to allow more effective monitoring and management of the Earth's resources;
- to better understand solid Earth processes.

The mission is aimed to continue and improve upon measurements initiated by ERS-1 and ERS-2, and to take into account the requirements related to the global study and monitoring of the environment. The mission is an essential element in providing long-term continuous data sets that are crucial for addressing environmental and climatological issues. The mission will at the same time further promote the gradual transfer of applications of Earth observation data from experimental to pre-operational and operational exploitation (end quote)"

1.2 MERILand aims and objectives

MERIS is the Medium Resolution Imaging Spectrometer, one of the payloads of ENVISAT. MERIS' mission over land is dedicated to land surface processes: global scale vegetation monitoring, distribution, extent and condition. The primary mission goal, however, is bio-optical oceanography: assessment of surface optical properties and water constituents leading to phytoplankton biomass and productivity via the estimation of pigment concentrations (Rast & Bezy, 1990). Secondary mission goals include atmospheric investigations of cloud and aerosol parameters and global scale monitoring of vegetation. Land application form a modest

contribution to the mission goal, although MERIS has large potential for such investigations. The MERILAND project aims at gaining insight in the possibilities that MERIS may offer for land applications and the development of algorithms that may lead to standard product formulation. In line with this the objectives as originally defined in 1997 of the MERILand project were:

- To develop a database of spectral signatures of earth materials with MERIS specification,
- To develop simulated MERIS data sets for various land applications,
- To study MERIS simulated data and the potential for quantified land observation,
- To develop algorithms for information extraction from MERIS data,
- To develop an infrastructure for easy access to the simulated data and algorithms.

MERIS is designed to acquire data at variable bandwidth ranging from 1.25 nm. to 30 nm., over the spectral range of 390 nm. to 1040 nm. depending on the width of the spectral feature to be resolved and the amount of energy needed for adequate observation (Rast & Bezy, 1990). The position, width and gain of each band can be set separately for each of the 15 bands that can be down loaded simultaneously. Thus MERIS is a fully programmable system that has the capability of in-flight selection of bands, the repositioning of bands based on new findings or to cope with partial instrument failures or deficiencies and exploration for new issues. Due to difficulties of achieving these band adjustments it seems not likely that in many studies these special MERIS' band settings can be exploited, thus in the project we focused on the standard band set for the instrument. Note that atmospheric calibration of MERIS data is not included in the objectives of the project because ESA has intended not to release raw data to the users. An atmospheric correction algorithm over land for MERIS is given by Santer *et al.* (1999).

Land applications explored under the MERILAND project concentrated on the following crucial fields:

- Surface mineralogy mapping for soil and geological surveying,
- Soil chemistry and degradation studies,
- Vegetation indices for biomass estimations,
- Red edge detection for crop vitality studies, and
- A preliminary investigation on the effect of scale on the observations.

Chapter 2

ESA's Medium Resolution Imaging Spectrometer

2.1 Introduction

Within the framework of ESA's Earth Observation Programme, the Medium Resolution Imaging Spectrometer (MERIS) is developed as one of the payload components of the ENVISAT-1, proposed for launch on the first European Polar Platform scheduled for June 2001 (Rast *et al.*, 1991; Bézy *et al.*, 1996; ENVISAT homepage). MERIS is an advanced optical sensor with high spectral and moderate spatial resolution designed to acquire remote sensing data of relevance to environmental management and to the understanding of regional to global scales (Verstraete *et al.*, 1995; Bézy *et al.*, 1996). MERIS' primary mission goal embraces biophysical oceanography (phytoplankton biomass and productivity) and the secondary mission goals of MERIS include atmospheric investigations as well as land surface processes (Rast *et al.*, 1991; Morel *et al.*, 1993).

MERIS objectives are (Bézy *et al.*, 1996):

Primary mission objectives:

- the measurement of photosynthetic potential by detection of phytoplankton (algae);
- detection of yellow substance (dissolved organic material);
- detection of suspended material (re-suspended or river borne sediments);

Secondary mission objectives:

- atmospheric investigations on cloud and aerosol parameters;
- land surface processes: global scale vegetation monitoring, distribution, extent and condition.

Recently (Rast *et al.*, 1999) these objectives were re-interpreted. MERIS' main applications objectives for oceanography are the measurement of phytoplankton, yellow substance and suspended matter. Atmospheric applications include cloud properties (top height and optical depth) and the measurement of water vapour column content and aeosols. The combination of the fine radiometric resolution and the 3 day repeat cycle also make MERIS a promising instrument for various land applications with a global change mission.

The capabilities of MERIS for oceanic studies have been widely investigated, here we study the use of MERIS for land applications. Some work on this topic has been conducted. Verstraete *et al.* (1995) described MERIS' potential to monitor pressing issues such as the cycling of carbon in the Earth System (e.g. Bolin *et al.*, 1986), destruction of habitats and the loss of biodiversity (Wilson, 1988), erosion of the topsoil (Brown and Wolf, 1984), deforestation (Hecht and Cockburn, 1989) and desertification (UNCOD, 1977). Because of its fine spectral and moderate spatial resolution, MERIS will increase significantly the present capability to monitor terrestrial environments at regional to global scales. The repetitive

acquisition of such measurements should allow a much improved description of the dynamics of ecosystems, the quantification of deforestation and desertification processes, the monitoring of biomass burning and agricultural production and the documentation of land cover changes (Verstraete *et al.*, 1995).

MERIS	Specification	Cutter et al. (1989)	Rast et Al. (1991)	Rast & Bézy (1995)	Web site
SYSTEM					Level 1B-Product
	Lifetime			4 years	
	Reduced Resolution Mode (RR)		1.5 Mbits/s	1.6 Mbits/s	
	Full Resolution Mode (FR)		22.5 Mbits/s	24.0 Mbits/s	
GEOMETRIC					
	Instrument Field of View (IFOV)	82°	81.52°	68.5° (nadir)	68.5°
	Swath width Envisat-1 orbit	1500 km	1450 km	1150	1150
	Spatial Resolution: RR		1200	1200	1200
	FR	260 m	250	300	300
	Localisation Accuracy without			< 2 km	
	use of Landmarks				
SPECTRAL	Spectral range	400-1050 nm.	400-1050 nm.	390-1040 nm.	400-1050 nm.
	Spectral Sampling Interval	1.25 nm. - 40 n	1.25 nm.	1.25 nm.	1.25nm.
	Number of Transmitted/Programmab Bands	30	15	15	15
	Spectral Bandwidth		10 nm.; 685 = nm.	1.25 - 30 nm.	2.5-20 nm.
	Registration Between Bands			0.12 RR IFOV	
	Band Centre knowledge			< 1 nm.	
RADIOMETRIC	Polarisation Sensitivity	<1%	< 1%	< 0.4	
	Radiometric Accuracy	400-1000<2% relative to sun		390-900<2% relative to sun	400-900<2%
					900-1050<5%
	Dynamic Range	albedo=1		up to albedo = 1	
	S/N (over open ocean)		778 (b2); 1 (b8); 54 (15)	from 1500 (b1) 200 (b14)	
OTHER	Depointing Angle	20° along track			
	Orbit Envisat-1		sun synchronous polar	Sun Synchronous Polar	
	Inclination		98.5°	98.5°	
	Nodal Crossing Time (descending)		9:55 AM	10:00 AM	
	Mean Orbital Altitude		800 km	800 km	

Table 1. MERIS system performance parameters.

In order to evaluate the potential of MERIS for land applications and to guide in the development of algorithms for data analysis, existing airborne imaging spectrometer data sets will form the basis for generating simulated MERIS data products. Available existing datasets for MERIS simulation are: DAIS-7915 (La Peyne, 1997, Tabernas, 1999); HyMAP (Tabernas, 1999); GERIS (Almaden, 1989); CASI (Kenya, 1997); MAIS (China, 1994) and AVIRIS (Flevoland, 1991, Ardèche, 1991). Those existing datasets will be spectrally and spatially resampled towards MERIS specifications. Some difficulties are encountered using data sets having a coarser spectral range than MERIS (e.g. DAIS and GERIS) because no exact spectral response can be simulated. The rather simple approach 'nearest neighbour resampling' or 'band

matching' is used to overcome this problem. Spatial degrading is carried out using gaussian filters. In addition to understanding the spatial and spectral behaviour of MERIS, in this chapter we discuss MERIS properties and capability for land applications on basis of literature. Hence the selection of a feasible data set is carried out based on 'multi-criteria analysis' of the available data sets.

2.2 The MERIS instrument

The MERIS main performance requirements are shown in Table 1. This Table is based on former published papers from Cutter *et al.* (1989), Rast *et al.* (1991, 1999), Rast and Bézy (1995) and the ENVISAT homepage. A review of MERIS' current status is provided in Rast *et al.* (1999). MERIS is a pushbroom imager that will acquire 15 bands (despite of being fully programmable) in the 390-1040nm range of the electromagnetic spectrum with a variable spectral bandwidth between 1.25 and 30nm. The pixel sizes at nadir are 260m across-track and 300m along-track which will be re-sampled (on board) to 1040m by 1200m over open ocean. The instrument has a 68.5 degree field of view providing a swath of 1150km on the ground, where the field of view is divided between five identical cameras each having a 14 degree field of view. On-board Envisat, MERIS is put into a sun-synchronous polar orbit with a mean altitude of 800km and a time of overpass of 10:00 a.m.

2.2.1 Scanning

The instrument scans the Earth's surface using the 'pushbroom' method. The MERIS *optical arrangement* is set up in such a way that six contiguous optical modules view the earth through a deflecting mirror, thus subdividing the 1150 km. total field of view into six slightly overlapping sub-scenes (each module covering approximately 14°; Rast *et al.*, 1995). Each module images an across-tracking strip of the earth's surface onto the entrance of the imaging spectrometer while the satellite's motion provides scanning in the along-track direction.

In the imaging spectrometer the radiation is dispersed and imaged onto radiation-sensitive arrays (CCDs) providing spatial and spectral data at the same time. This design will limit the distortion of the pixel shape and size, as the only major source of geometric deformation will be the curvature of the Earth and topography (Verstraete *et al.*, 1995). The design of the imaging chain favours the selection of individual bands for transmission as well as the possibility to switch from 'full' spatial resolution mode (FR), i.e. 300 m., to the reduced spatial resolution mode (RR) of 1200 m. (Rast *et al.*, 1995). An additional advantage of combining sixteen detector element signals into one is the increase in the signal to noise ratio (SNR) of the imaged scene.

Due to its spectral configuration (MERIS operates in the visible and near infrared) the radiometric quality of the data acquired will depend on the illumination of the Earth. A solar zenith angle of less than 80 degrees is needed for effective recovery of geophysical data from MERIS (Bézy *et al.*, 1995; Merheim-Kealy *et al.*, 1995; Van der Woerd & Dekker, 1997; Verstraete *et al.*, 1995; MERIS website).

2.2.2 Calibration

Relative spatial calibration is carried out when the spacecraft is over-pathing the Antarctic and the sun illuminates the instrument in a vertical angle to its nadir (Rast *et al.*, 1991; ENVISAT homepage). The relative calibration between the six optical modules will be carried out by comparing the neighbouring module responses in the areas of overlap.

For absolute radiometric calibration, diffuser planes attached to the instrument will be inserted into the field of view in front of the two outside optical modules. The relative to absolute calibration will be determined by normalising the ratio of integrating sphere and the

diffuser plate response. Wavelength calibration is also foreseen to use the sun illuminated integrating sphere through an aperture with an optical filter. Dark current calibration is achieved by measuring either the masked CCD elements or the response of the array under full frame observation, provided by tilting the deflecting mirror.

Spectrometric calibration will be performed every three months by first performing a radiometric calibration with appropriate band settings for the spectral calibration under consideration, and deploying the Erbium doped diffuser with the same band settings the second orbit.

Further technical details on the electrical and mechanical structure of MERIS can be found in Cutter *et al.* (1989), Bézy *et al.* (1990) and Rast *et al.* (1991), Verstraete *et al.* (1995), Van der Woerd and Dekker (1997) and on MERIS homepage.

Band Nr	Band centre nm.	Bandwidth nm.	Potential Applications
1	412.5	10	Yellow substance, Turbidity
2	442.5	10	Chlorophyll absorption maximum
3	490	10	Chlorophyll, pigments, polarisation measurement
4	510	10	Turbidity, Suspended sediment, Red tides
5	560	10	Chlorophyll reference, Suspended sediment
6	620	10	Suspended sediment
7	665	10	Chlorophyll absorption
8	681.25	7.5	Chlorophyll fluorescence
9	705	10	Atmospheric correction, Red Edge
10	753.75	7.5	Oxygen absorption reference
11	760	2.5	Oxygen absorption R-branch
12	775	15	Aerosols, vegetation
13	865	20	Aerosols corrections over ocean
14	890	10	Water Vapour Absorption Reference
15	900	10	Water Vapour Absorption

Table 2. MERIS final 15 spectral bands.

2.2.3 Spatial characteristics

MERIS products will be in full resolution (FR) mode (300 m) or reduced resolution (RR) mode (1200m). MERIS itself, produces data at the 300 m. scale: on-board processing bins this data using a 4x4 average to produce the 1.2 km. data. Product partition for archiving purposes is performed by segment: 43.5 minutes for the MERIS reduced resolution RR corresponds to 17400 km. along track (taking the sun illumination limitations into account). A MERIS FR segment corresponds to a maximum of 7960 km. along track, equivalent to 20 minutes- not necessarily continuous - on average, with the same sun illumination limitations. The FR mode provides detailed information which allows the study of processes at scales much closer to those characteristic of human activities. Individual pixels may be more homogeneous horizontally than at the 1.2 km. resolution providing better validation of the models and procedures of data analysis. The disadvantages of the FR mode are the very large amount of available data and the earlier mentioned 20 minutes along track segment due to power and data transmission constraints (Verstraete *et al.*, 1995).

2.2.4 Spectral characteristics

MERIS is a fully programmable, high-spectral-resolution, imaging spectrometer operating in the solar reflective spectral range (400-1040 nm.; Morel *et al.*, 1993; Verstraete *et al.*, 1995).

The position, width, and gain of each band can be set separately for each of the 15 bands that can be downloaded simultaneously. The spectral bandwidth is variable between 1.25 and 20 nm. depending on the width of the spectral feature to be observed and the amount of energy needed in a band to perform an adequate observation (Bézy *et al.*, 1996). Over open ocean an average bandwidth of 10 nm. is required for the bands located in the visible part of the spectrum. To resolve spectral features of the 760 nm. oxygen absorption band a minimum spectral bandwidth of 2.5 nm. is required. Table 2 describes the final 15 spectral bands in detail. In these final settings the 765 nm. band (described in former publications: Doerffer *et al.*, 1995; Bézy *et al.*, 1996) is excluded (pers. comm. Mike Rast, 1998).

The MERIS instrument proposes significant advances over its precursors (NOAA AVHRR, SPOT HRV or Landsat TM) because MERIS samples the spectral reflectance of the targets in 15 narrow bands (Verstraete *et al.*, 1995) and provides an intermediary spatial resolution between Landsat TM (30 m.) and AVHRR (1100 m.).

The large FOV ensures complete global coverage in three days. However, a large FOV results in very broad pixels at the edges of the image and may cause serious problems when interpreting land surface properties. Probably only the scanned surface at nadir can be used.
The features of the fully programmable MERIS instrument allow for:

- in-flight band selection, repositioning of bands based on new findings or to cope with partial instrument failures or deficiencies and exploration of new scientific issues as well as the documentation of the performance of these new technologies.
- increase of the signal to noise ratio in comparison with current satellite sensors. MERIS data will be acquired with a S/N ratio of 50 to 1500, depending on the spectral band, target type and the illumination conditions.

Disadvantages are:

- in-flight band selection is limited by the operation constraints: a solid scientific motif may result in a re programming of MERIS configuration for projects during one-two weeks. Note that no atmospherically corrected products will be provided for non-standard band sets.

2.3. MERIS data products

The radiometric requirements and radiometric accuracy of MERIS are far in excess of that of sensors currently operational and are set to allow discrimination of 30 classes of pigment concentration over open ocean each smaller or equivalent of 1 mg m^{-3}. On-board band-to-band calibration utilizing sun illuminated spectralon diffuser panels yields spectral calibration. MERIS' data levels and products that are defined by ESA include (Merkheim-Kealy et al. 1999):

- Level 0 products:

These are raw instrument data not to be provided to the use community

- Level 1b products:

These are geolocated and calibrated data resampled to equal-area MERIS product grids. Top-Of-Atmosphere (TOA) radiance in $mWm^{-2}sr^{-1}nm^{-1}$ will be provided for all 15 standard bands. Algorithms are being developed to convert this to TOAA reflectances.

- Level 2 products:

Level 2 products include geolocated geophysical products as surface radiance and surface reflectance. Santer et al. (1999) provide a review of the atmospheric correction procedure over land. These atmospheric correction routines produce cloud-top height, cloud albedo, and water vapor column abundance as "by-products".

- Level 3 products:

Level 3 products are geometrically resampled level 2 products to an appropriate coordinate geometry, are presently not foreseen by ESA. Other derived products that are under development (Verstraete *et al.* 1999) include the MERIS Global Vegetation Index (Gobron *et al.* 1999) and a MERIS Normalized Difference Vegetation Index. In addition, ESA is also considering the Fraction of Absorbed Photosynthetically Active Radiation (FAPAR) in vegetated areas as described by Govaerts *et al.* (1999) and a red-edge index as presented by Curran *et al.* (1995).

Chapter 3

MERIS data simulation

3.1 Introduction

Former investigations by Doerffer *et al.* (1995) to develop algorithms for monitoring coastal water constituents have shown the potential use of airborne spectra for MERIS simulation. An inverse modelling method has been applied to MERIS' spectral bands which have been calculated from aerial measurements with a high resolution (2 nm. resolution) spectrometer.

In general, image or spectral simulation is only possible when the source sensor has a spatial and spectral resolution higher and better respectively than the target simulated sensor (Justice *et al.*, 1989). The *Spectral Resampling* of existing airborne/spaceborn data sets towards the MERIS spectral properties are not described in detail in the literature. Investigators mention a simulation of MERIS data (Doerffer *et al.*, 1995; Verstraete *et al.*, 1995), however without details on the resampling procedure of the existing wavebands and centres towards the MERIS specifications. *Spatial resampling* methods are described by Justice *et al.* (1989) and Teillet & Staenz (1992). Both use a spatial filter (gaussian blur filter) and sampling mechanism (Fast Fourier Transforms) to simulate coarse resolution data. Simulation procedures are described in more detail in a subsequent paragraph.

Available European datasets for MERIS simulation are from the GERIS, DAIS-7915, AVIRIS and CASI sensors. The latter two have a higher spectral resolution than MERIS; GERIS and DAIS-7915 in some bands have a coarser bandwidth than MERIS (Figure 1). In Figure 1 a typical atmospheric transmittance curve is shown in the 400-1100 nm. wavelength region. Above this figure MERIS, GERIS, DAIS, CASI and AVIRIS spectral properties are displayed using bars. In each bar, the spectral properties of the imaging spectrometer is plotted band by band. For example the MERIS bar's black parts indicate its spectral bandwidth. In the white parts no measurement takes place. Within these black parts the verticle lines give the bandcentres. Some sensors have overlapping spectral bands resulting in a total black line. In the next sessions, each airborne sensor will be discussed according to its feasiblity to simulate MERIS.

3.2 Datasets available

Data sets from the following airborne instruments are available to conduct MERIS simulation: GERIS, AVIRIS, CASI, DAIS-7915, MAIS. Table 1 describes some airborne imaging spectrometers and the available bands to simulate MERIS spectral bands using the principle of direct band matching.

MERIS		GERIS		DAIS		CASI			AVIRIS		
Band	Nm.	band	Nm.	band	Nm.	Band	MERIS	Nm.	Band	MERIS	Nm.
1	0.4125	-		-		4 to 10	7	0.4121	5,6	5	0.41175
2	0.4425	-		-		22 to 27	24	0.4417	8,9	8	0.4408
3	0.49	2	0.489	1	0.501	49 to 54	52	0.4907	13,14	13	0.48967
4	0.51	4	0.514	2	0.517	60 to 66	63	0.5101	15,16	15	0.50934
5	0.56	8	0.564	5	0.567	88 to 94	91	0.5595	20,21	20	0.55874
6	0.62	13	0.625	8	0.621	122 to 128	125	0.6198	26,27	26	0.61824
7	0.665	16	0.662	11	0.671	148 to 153	150	0.6644	30,31	31	0.66779
8	0.68125	18	0.687	12	0.689	157 to 162	159	0.6805	34,35	35	0.68491
9	0.705	19	0.699	13	0.705	170 to 175	173	0.7055	37,38	37	0.70398
10	0.75375	23	0.749	16	0.756	198 to 202	200	0.7539	42,43	42	0.75174
11	0.76	24	0.761	16		203, 204	203	0.7593	43	43	0.7613
12	0.775	25	0.774	17	0.773	208 to 216	212	0.7755	44,45	44	0.77086
13	0.865	-		22	0.86	256 to 267	262	0.8653	53,54,55	54	0.86665
14	0.89	-		24	0.895	273 to 278	276	0.8905	56,57	56	0.88583
15	0.9	-		24		279 to 284	281	0.8995	57,58	57	0.89542

Table 3. Available bands to simulate MERIS spectral bands.

3.2.1 GERIS

The GERIS sometimes referred to as GER-63 or GERAIS, is an airborne 63-channel imaging spectrometer designed for environmental studies and acquisition of spectral information pertinent for geological studies (Kramer, 1996). It contains three spectrometers which cover the spectrum contiguously from the visible to the short-wave infrared range. The spectral specifications of the GERIS are determined by design models tailored within system parameters to specific customer requirements.

The available GERIS dataset from Spain is flown over the Almaden area in 1989 and it covers 512 spatial pixels of 12m. One problem is the poor quality of the data. After a Minimum Noise Fraction (MNF) transform there still remains some salt-and-pepper noise in all the bands. GERIS band 24 (to simulate MERIS band 11) show a moving in the verticle direction of some 5 pixels. The MNF transformation rotates the original data to the principal component space and orders the principle components according to the amount of noise. The use can now eliminate noise MNF bands or filter noise fractions using fourier techniques and when finished rotate the 'cleaned' MNF bands back to the original data space. For a more detailed dscription of the MNF rotation see Green *et al.*. (1988).

It is obvious from Figure 1 and Table 1, that the Almaden data set has some simulation constraints because not all MERIS bands (1=412.5 nm., 2=442.5 nm., 13=865 nm., 14=890 nm. and 15= 900 nm.) fall in the spectral range of the GERIS sensor. The other simulation constraint is the coarser spectral bandwidth of the GERIS. Only one band can be selected for MERIS simulation, which is the nearest neighbour spectral band. For the simulation of MERIS band 3 (490 nm.) GERIS band 2 (489 nm.) is choosen, which is more precise in comparison with the simulation of MERIS band 8 (681.25 nm.) using GERIS band 18 (687 nm.).

However the GERIS spectral bandwidth (25 nm) is much coarser than the MERIS spectral bandwidth (10 nm) thus incorporating more spectral information into the desired spectral band. This is best illustrated when simulating the two very narrow MERIS band 10 (753.75 nm. with bandwidth of 7.5 nm.) and 11 (760 nm. with bandwidth of 2.5 nm.). Both bands can be simulated with GERIS band 24, however the bandcentre of GERIS band 24 has its nearest neighbour for MERIS band 11 and hence GERIS band 23 is used for

simulating MERIS band 10. Also in this case the GERIS bandwidth is far too coarse to simulate MERIS.

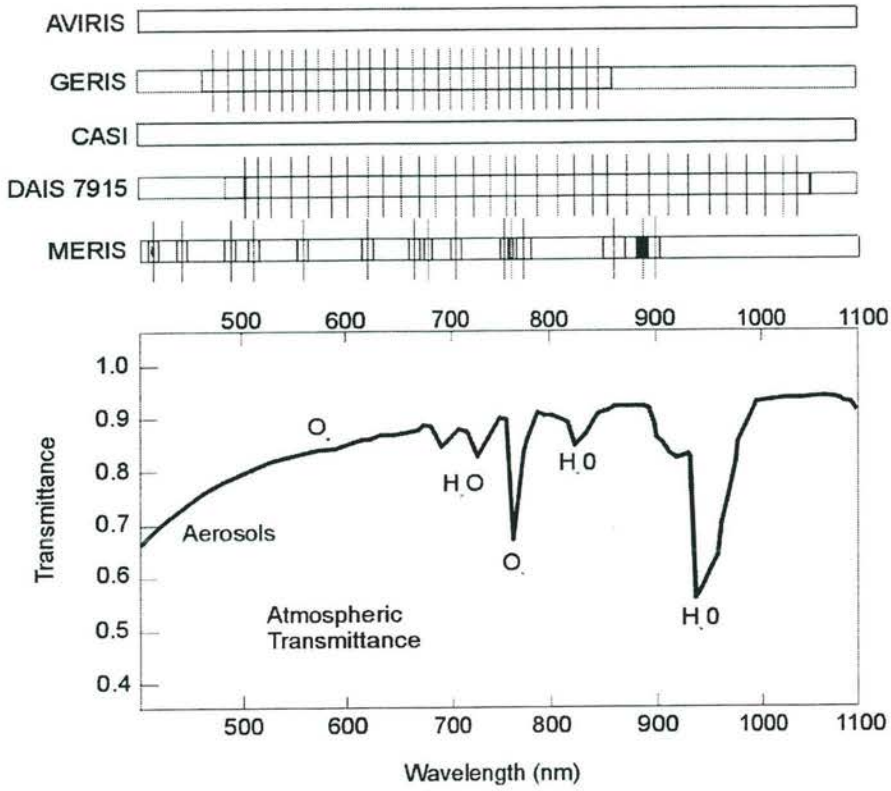

Figure 1. Atmosphere spectrum with main gas absorption bands indicated. The topmost part of the figure shows the wavelength coverage (bar) and the channels center wavelengths (vertical lines) for MERIS and four airborne imaging spectrometer systems which can be used to simulate MERIS data.

A regression analysis is carried out to compare the spectral matching properties of the simulating datasets. Plotting MERIS spectral band positions against those of GERIS a regression line through the data points expresses the similarity between the band positions. In the ideal situation all points would lie on the line y=x. If the band positions are perfectly related, then R^2 (regression coefficient) will be 1. R^2 is interpretable in the following manner: when R^2 is 0.9 this means that there is 90 % resemblance between the spectral band positions.

Figure 2 is a graph of a regression analysis in which the spectral band center positions of MERIS and GERIS are pointed out. Bandwidth is not taken into account. According to the regression coefficient of 0.9986 a good fit is obtained and it can be concluded that GERIS can be used to simulate MERIS.

3.2.2 DAIS-7915

DAIS-7915 (Digital Airborne Imaging Spectrometer) is a 79 channel scanner that covers the spectral range from the visible to thermal infrared wavelength at a variable spatial resolutions from 5-15 m. for flight altitudes of 15-4500 m. (Kramer, 1996). The system is integrated and operated by DLR and has been flown since mid-1994. DAIS' applications are environmental monitoring of land and marine ecosystems, vegetation stress research,

agriculture and forestry resource mapping, geological mapping, mineral exploration and provision of data for geographic information systems. The available DAIS dataset is flown in the La Peyne area in France in 1997.

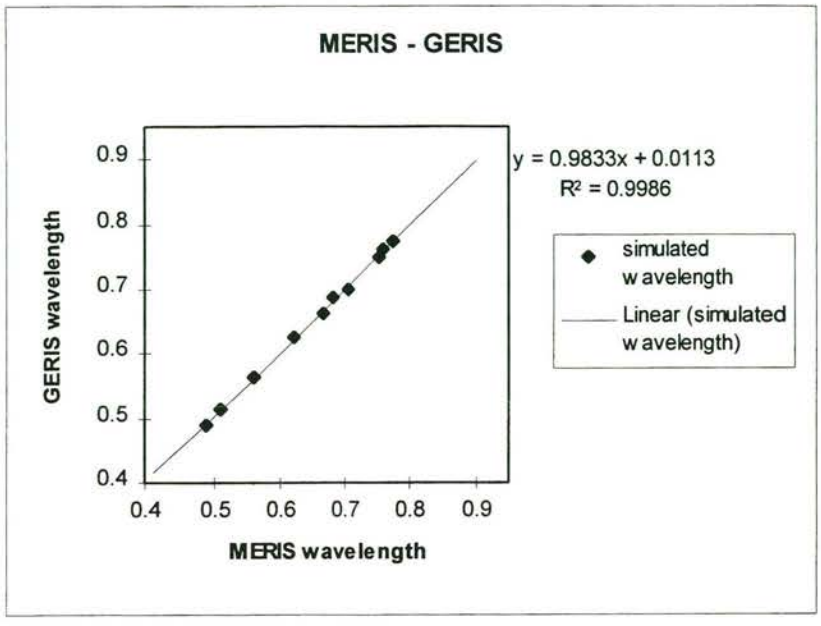

Figure 2. Regression analysis between GERIS and MERIS spectral matching positions.

Figure 1 shows DAIS spectral properties. Like the GERIS, DAIS cannot simulate all MERIS bands. MERIS bands 1 and 2 cannot be simulated because DAIS starts measuring at 486 nm. Simulation of MERIS bands 11 and 15 is difficult because the spectral resolution of DAIS is too coarse. For example DAIS band 16 (756 nm.) is used to simulate MERIS band 10 (753.75 nm.) and DAIS band 17 (773 nm.) for MERIS band 12 (775 nm.). In theory MERIS band 11 must be simulated with DAIS band 16 but this band is already used for MERIS band 10. Therefore DAIS band 16 is used to simulate either MERIS bands 10 and 11.

In Figure 3 the regression analysis parameters are pointed out. The resulting R^2 is higher than the regression of GERIS data thus DAIS provides a better spectral matching than GERIS.

3.2.3 CASI

CASI (Compact Airborne Spectrographic Imager) is a spectrometer/multispectral pushbroom (CCD) imager system which covers the visible and near infrared spectrum (400-1000 nm.) with 1.8 nm. sample intervals (288 spectral bands) and 512 spatial pixels (Kramer, 1996). The main advantage of the use of CASI to simulate MERIS is the very narrow spectral bandwidth of the CASI. Each MERIS band can be simulated using between 2 and 12 CASI bands. For example, MERIS band 1 ranges from 407.5 - 417.5 nm. The CASI wavelengths that cover this range include band 4 (centre 406.9 nm.) until band 10 (417.3 nm.) where band 4 and band 10 lie somewhat outside MERIS band 1 wavelength range. To simulate MERIS wavelength a weighted average can be carried out:

tempory band a-1 :((406.9+(0.5*1.8)-407.5)/1.8) * CASI band 4
tempory band a :CASI band 5 +6+7+8+9
tempory band a+1:((417.5-417.3-(0.5*1.8))/1.8) * CASI band 10

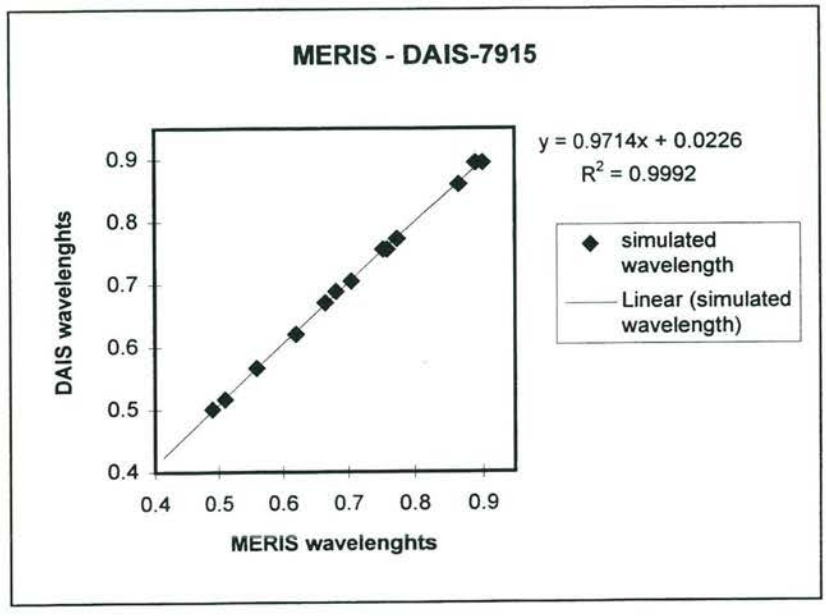

Figure 3. Regression analysis between DAIS-7915 and MERIS spectral matching positions.

Band 4 lies for 33.33 % in the range of the MERIS band 1 and band 10 for 62.28 %. Band 5 to 9 are completely covered by the MERIS band. An essential feature upon this approach is the spectral position of the bandcentre. CASI band 10, for example, has its bandcentre at 417.3 nm., which lies inside MERIS range.

Therefore you can state that the whole spectral response of this band can be used to simulate MERIS, because the same is carried out using GERIS or DAIS data.

For CASI the selected spectral matching bands result in a R^2 of 1 (Figure 4). This is an ideal situation and hence CASI is a very good dataset to simulate MERIS.

3.2.4 AVIRIS

AVIRIS is a NASA/JPL instrument which measures transmitted, reflected and scattered solar energy from the Earth's surface and atmosphere in 224 channels over extended regions at high spatial resolutions (Kramer, 1996). AVIRIS uses scanning optics and a group of four spectrometers to image a 614 pixel swath width simultaneously in 224 contiguous spectral bands ranging from 380 - 2500 nm.

AVIRIS data has, like CASI data, a higher spectral resolution than MERIS which means that every MERIS band can be simulated using one or more spectral bands of AVIRIS. Available AVIRIS imagery of 1994 on the internet (AVIRIS homepage) can be used to simulate MERIS and mostly 2 AVIRIS bands are available to simulate a MERIS band. Only MERIS band 11 (2.5 nm. bandwidth) and MERIS band 13 (20 nm. bandwidth) use 1 and 3 AVIRIS bands respectively (Figure 5).

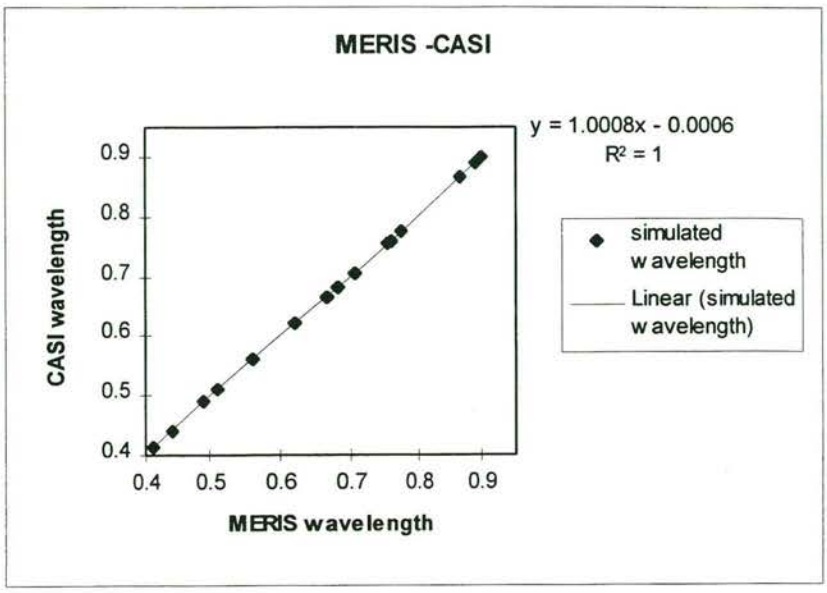

Figure 4. Regression analysis between CASI and MERIS spectral matching positions.

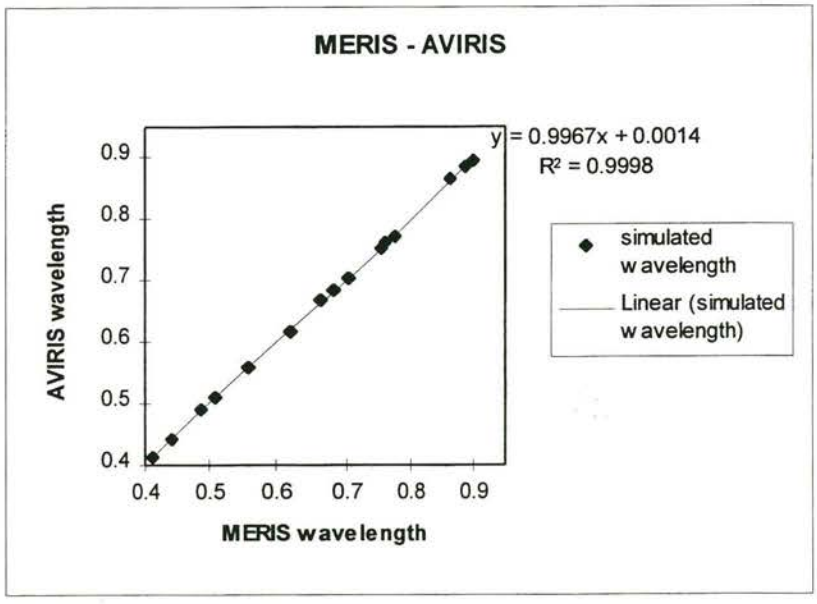

Figure 5. Regression analysis between AVIRIS and MERIS spectral matching positions.

3.3 Multi-Criteria Analysis (MCA)

According to the spectral matching positions the best available dataset is still not known. However, no spectral resolution is taken into account. Therefore a multi-criteria analysis is carried out to define the most appropriate dataset to simulate MERIS. The following variables yielding input for this analysis: spatial resolution, spectral resolution of each band, spectral matching of each band, dataset source, data quality. The final summed up values are described in Table 2 and 3. Each criteria is given a 'weight' and the sum of the 'weights' results in a sensor having the best properties to simulate MERIS.

	GERIS	DAIS	CASI	AVIRIS	Maximum
Spatial Resolution	10	10	10	10	10
Spectral Resolution	9.5	14.25	30	29	30
Spectral Matching	16.5	15.5	30	29.5	30
European Dataset	10	10	0	10	10
Data Quality	5	15	15	15	15
TOTAL	51	64.75	85	93.5	95
RANKING	4	3	2	1	
ACCURACY	53.68	68.15	89.47	98.42	100

Table 2. Multi-Criteria-Analysis result of the available data sets.

Criteria/Variables Spatial Resolution, European Dataset and Data Quality are of minor importance than the Spectral parameters and are therefore assigned with minor weights. In the final ranking AVIRIS is the best data set to simulate with, but this is an incorrect result. CASI's spectral and spatial properties are respectively higher and equal according to AVIRIS spectral and spatial properties but Criteria 'European Dataset' gives AVIRIS the final 'winning' weight.

The Spectral Resolution and Spectral Matching Criteria are given 'weights' in the following manner. CASI's spectral resolution is that accurate that all MERIS bands can be simulated using between 2 or 12 bands and hence each band is given a weight of '2' summing up a total of 60 points. For example criteria Spectral Resolution: DAIS band 22 for simulation MERIS band 13 is given a weight of '2' because of the similarity between the spectral bandwidths of the particular sensors. However DAIS band 16 is given '0.25' to simulate MERIS most narrow band 11.

This MCA is subjective, and the different weights depend on the relative position among each other. The latter means that if for example GERIS-MERIS band 4 is thought to be less accurate than DAIS-MERIS band 4, GERIS 'band 4' is given a weight of '1' whereas DAIS 'band 4' is given weight '1.5'.

3.4 Simulation procedure

Image (or spectral) simulation is only possible when the source sensor has a spatial and spectral resolution finer and better respectively than the target simulated sensor (Justice *et al.*, 1989). The *Spectral Resampling* of existing airborne/spaceborne data sets towards the MERIS spectral properties are not described in detail in the literature. Investigators mention a simulation of MERIS data (Doerffer *et al.*, 1995; Verstraete *et al.*, 1995), however without details on resampling procedures of the existing wavebands and centres towards the MERIS specifications. *Spatial resampling* methods are described by Justice *et al.* (1989) and Teillet & Staenz (1992). Both use a spatial filter (gaussian blur filter) and sampling mechanism (Fast Fourier Transforms) to simulate coarse resolution data. Some simulation studies have been conducted to aid in the understanding of other future spaceborn imaging spectrometers including MODIS (Kaufman *et al.* 1997) and ASTER (Abrams & Hook, 1995) again without documenting details on processing strategies.

VARIABLES		GERIS	DAIS	CASI	AVIRIS
Spatial Resolution		10	10	10	10
Spectral Resolution	band 1	0	0	2	2
	band 2	0	0	2	2
	band 3	1	0.5	2	2
	band 4	1	1.5	2	2
	band 5	1	1.5	2	2
	band 6	1	1.5	2	2
	band 7	1	0.5	2	2
Narrow	band 8	0.5	0.5	2	2
	band 9	1	1.5	2	2
Narrow	band 10	0.5	0.5	2	2
very narrow	band 11	0.5	0.25	2	1
Medium	band 12	2	2	2	2
Coarse	band 13	0	2	2	2
	band 14	0	1	2	2
	band 15	0	1	2	2
Spectral Matching	band 1	0	0	2	2
	band 2	0	0	2	2
	band 3	2	0.5	2	2
	band 4	2	1	2	2
	band 5	2	1	2	2
	band 6	2	2	2	2
	band 7	2	1	2	2
Narrow	band 8	1	1	2	2
	band 9	1	2	2	2
Narrow	band 10	0.5	1	2	2
very narrow	band 11	2	1	2	2
Medium	band 12	2	2	2	1.5
Coarse	band 13	0	1	2	2
	band 14	0	1	2	2
	band 15	0	1	2	2
European Dataset		10	10	0	10
Data Quality		15	15	15	15
	sum	61	64.75	85	93.5
	ranking	4	3	2	1

Table 3. Scores for the sensor multi-criteria analysis.

We followed a essentially two-step procedure (Figure 6):

- Step 1: Spectral resampling
  - convolution over the sensor's spectral response function (SRF) for each band in case of oversampled input data
  - or band matching in case of undersampled input data
- Step 2: Spatial resampling
  - spatial degradation using the sensor's point spread (response) function (PSF) for each band

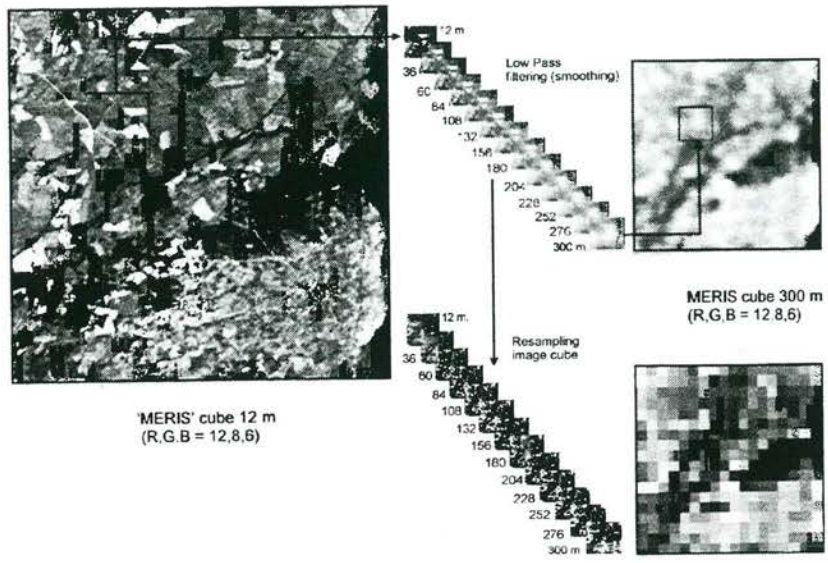

Figure 6. Synthetic example of the simulation procedure (color plate 1).

As a general rule in simulation it can be stated that only spectrally oversampled image data cubes can be used to generate channels of future sensor data types. The procedure of simulation involves estimating the gaussian spectral response function (SRF) of each MERIS channel using the band center and width (in full-width-half-maximum). This SRF is of the type

$$R_i(\lambda) = \frac{1}{\sigma\sqrt{2\pi}} e^{-0.5(\lambda-\mu)^2/\sigma^2}$$

where μ is the band centre, σ the standard deviation (equivalent to the FWHM) of the channel and λ the wavelength relative to μ and $R_i(\lambda)$ the spectral response. The integral over the SRF is 1. For each MERIS channel the spectral response curve is calculated using the gaussian approximation. The channels of the higher spectral resolution airborne imaging spectrometer data set that are within the wavelength range of the selected MERIS channel are integrated by dividing them into the derived SRF assuming that the initial SRF of the input data channels are a single bright source (i.e., a continuous input spectrum). This is done as follows

$$\rho_{res}(\lambda_i) = \frac{\int_{\lambda_1}^{\lambda_2} \rho(\lambda) R_i(\lambda) d\lambda}{\int_{\lambda_1}^{\lambda_2} R_i(\lambda) d\lambda}$$

where $\rho_{res}(\lambda_i)$ is the re-sampled spectrum using the continuous spectrum $\rho(\lambda)$ and the SRF $R_i(\lambda)$. This deconvolution is achieved by integrating between the lower (λ_1) and upper (λ_2) wavelength limit of the designated (i.e., to be simulated) image channel. Since the gaussian SRF only asymptotically approaches zero, we truncated the SRF at 1.5 times the FWHM. In case the spectral resolution of the image data to be simulated is equivalent to or less than that of the input data, band matching has to be applied. In this technique, the bands which position, in terms of wavelength of the band center, is closest to the channel to be simulated are used for the simulation process.

Spatial degradation is essentially a two-step process. The first step requires modelling the transfer function between the initial data and the desired data and deriving a spatial filter that allows simulation of the coarse resolution imagery. The second step involves re-sampling to the desired pixel size. As is the case in spectral re-sampling with the spectral response function, the sensor's Point Spread Function (PSF) gives the spatial response of the sensor. The PSF is defined as (Schowengerdt, 1997)

$$e_b(x,y) = \int_{\alpha_{\min}}^{\alpha_{\max}} \int_{\beta_{\min}}^{\beta_{\max}} s_b(\alpha,\beta) PSF(x-\alpha, y-\beta) d\alpha d\beta$$

where $e_b(x,y)$ is the resulting electronic signal for band b at location given by coordinate (x,y), $s_b(\alpha,\beta)$ is the input signal, whereas the limits of the integral determine the spatial extend in two dimensions, α and β, over which the physical signal is weighted. A common model for the PSF is given by

$$PSF(x,y) = \frac{1}{2\pi ab} e^{-x^2/2a^2 e^{-y^2/2b^2}}$$

where a and b determine the width of the optics of the PSF in the cross- and along track direction. In the absence of details on the PSF for MERIS, we used a normalized detector PSF which is equivalent to applying a square moving average filter of the desired spatial resolution

$$PSF(x,y) = \frac{1}{ab} \sum_{a=1}^{a} \sum_{b=1}^{b} s_b$$

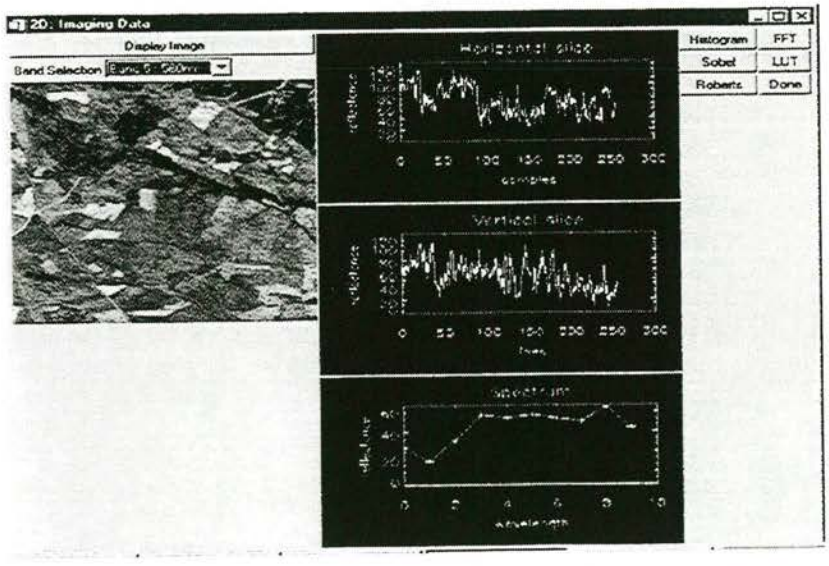

Figure 7. Example of the interface of the simulator package.

A software tool to simulate and analyse MERIS data was developed: Simulator (Figure 7). The simulator package is written in IDL (the Interactive Data Language); a 4GL. It allows the user to simulate spectral response (1 dimensional) and image data (2 dimensional) for various operational and planned earth observation satellite systems including LANDSAT MSS and TM, SPOT, ASTER and MERIS. Available components are *1 dimensional:* deconvolution: spectral re-sampling and plotting and *2 dimensional:* mixture modelling, MERIS create, upscaling, show images and spectra and cross correlogram spectral matching.

Chapter 4

MERISPEC: A spectral database for MERIS

4.1 Introduction

MeriSpec is a Microsoft Access® database application designed to store and ease consultation of spectral reflectance data, in full (350 – 2500 nm.) and Medium Resolution Imaging Spectrometer (MERIS, payload instrument of ESA's Envisat-1) (412 - 900 nm.) resolution. The spectral database consists of reflectance data and ancillary observations on sites in the Mediterranean area which are thought to be representative for this and similar environmental settings. The software allows new spectra/observations to be included. MeriSpec is developed to establish MERIS spectral data, on top of the full resolution data, of minerals, rocks, soils, vegetation and man-made structures using gaussian resampling of the full resolution spectral data. Spectral Response Functions have been estimated using fixed band centers of variable band-width as provided by ESA. These cover the MERIS' standard band-set.

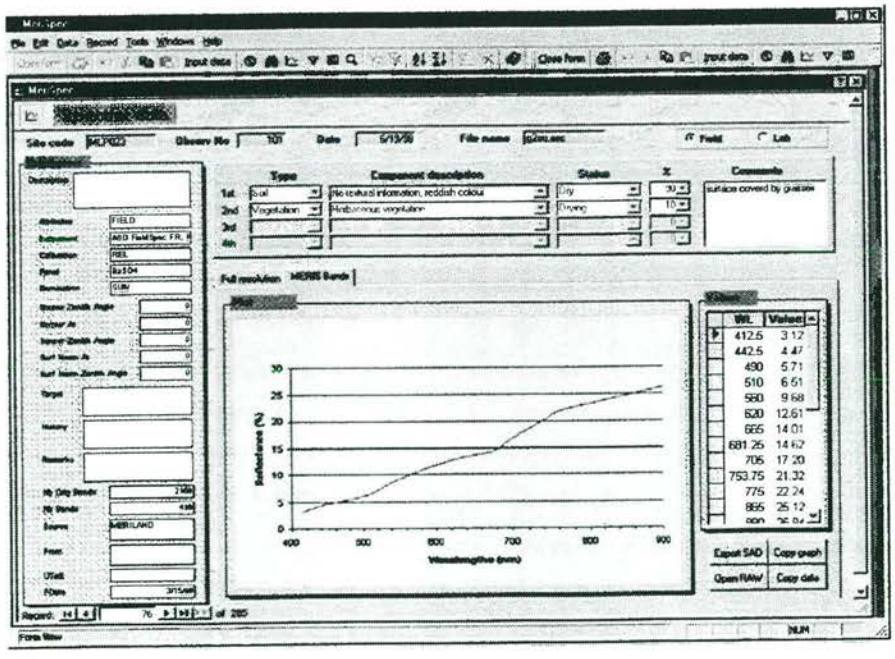

Figure 1. MeriSpec spectral data sheet and MERIS resampled spectrum of a mixed soil-vegetation target.

MeriSpec is based on the MedSpec database, the spectral database of Mediterranean environments prepared by the Joint Research Center. The MedSpec database is a tool to support the assessment and monitoring of desertification processes in the Mediterranean yielding spectral reflectance data in the range from 350 – 2500 nm. of natural surfaces together with specific parameters describing the environmental setting in a physiographic context (e.g. underlying geology, vegetation community, eco-zone). Data of the La Peyne area acquired in 1997 within the framework of the DeMon-2 project are complemented by field spectral measurements acquired in 1998 for the MERILand Project (BCRS) and biomass parameters (1997) calculated by students of the Utrecht University.

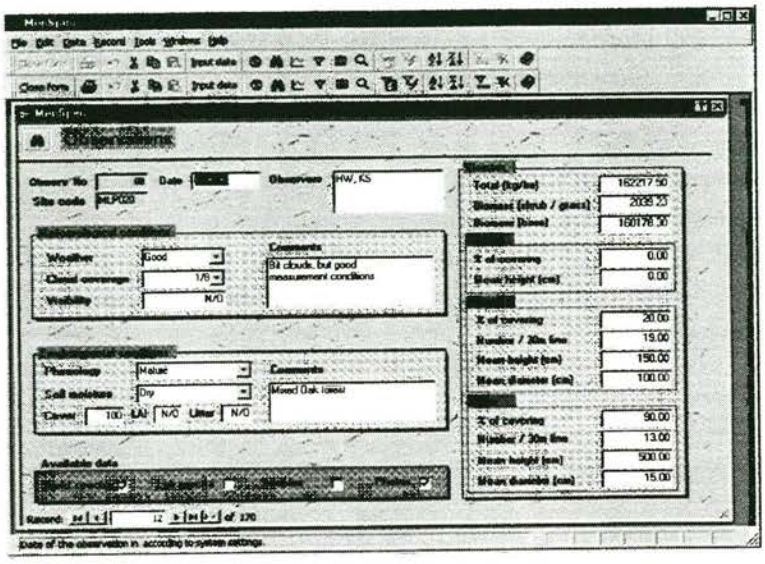

Figure 2. MeriSpec observation sheets.

MeriSpec is designed to browse and query data using graphical user interfaces. Data can be exported in ASCII format. Different levels of query are available to suit multiple spatially and thematically contextual searches, such as geographic coordinates and physiographic eco-regions. MeriSpec is based on a classic relational database model. Tables grouping thematic contents are linked to each other with common key fields. Two different types of tables are distinguished: data tables themselves (accessible and updated by users) and look-up tables which contain predefined values to standardize the input of some parameters of data tables and are not modifiable by the user. The information that is stored in the database is divided into 6 tables, which are the core of the database. These tables hold information about sites, observations, spectra, samples, photo's and object descriptions. These tables are linked to each other to ensure consistency of data. Mandatory parameters in MeriSpec are the date of an observation and the object description when adding a spectrum, a sample or a photo to the database. Important codes (e.g. the site code or the observation number), linking the tables, are generated automatically when new data is added. All other parameters are optional. The data tables structure is supplemented by so called look-up tables (LUT), which consist of pre-defined keyword lists. Controlled keywords allow a hierarchical structure of keywords and provide a limited number of entries for these parameters. This ensures consistency in the database and enables efficient query results. Such keyword lists were set up for the definition of the rock, soil and vegetation surfaces as well as for the land cover description of the sites. New data, spectral information and ancillary information on the sites, can be imported into the

database by the user. Examples of a MeriSpec spectral data sheet and observation sheet are given in Figures 1 and 2, respectively. More details on MERISPEC can be found in Appendix 1, a CDrom with the MERISPEC software and spectral data base is attached.

4.2 MERILand: The Field Campaign 1998

The La Peyne catchment is a key area in the DeMon project (DEsertification MONitoring), supported by the Environment and Climate Programme of the EU-DGXII, to develop and test methods to survey and to model land degradation processes in the Mediterranean part of Europe. Much data is therefore available: field spectral measurements on soil and vegetation in 1996 and 1997 and biomass estimations for different vegetation covers throughout the upper part of the catchment.
The aims of the fieldwork were:

- Collecting reference spectra for later image calibration of DAIS 98 flight.
- Collecting spectra of soil and vegetation for MERIS' spectral library (Figure 3).
- Collecting reference spectra and accurate description of the 1997 biomass estimation sites
- Collecting Difference Global Positioning System (DGPS) data for later geometric image correction of the DAIS 97 and 98 flights.

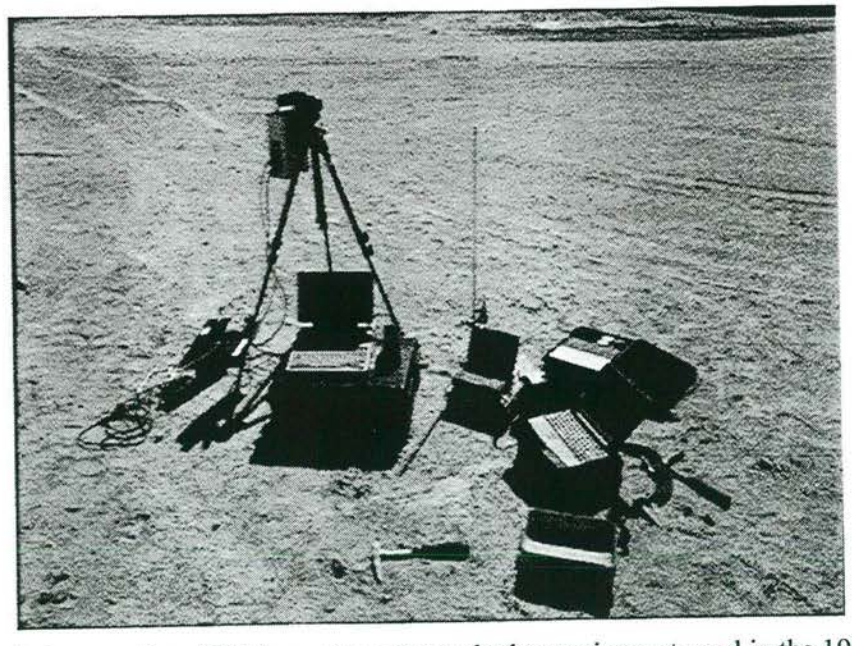

Figure 3. Impression of field spectrometer and other equipment used in the 1998 field campaign.

La Peyne test area (Figure 4) is located in southern France, roughly between Montpellier and Béziers. The upper part of the study area is characterised by a hilly terrain covered by a mixed oak forest of Mediterranean sclerophylous species which botanists assumed being the natural climax Mediterranean vegetation. The dominant species are holm oak (*Quercus Ilex*), the downy oak (*Quercus Puberscens*), the strawberry tree (*Aburtus Unedo*) and the Erica tree (*Erica arborea*). Various disturbances of the forest coverage are found due to open mining of dolomite and bauxite. The lower part, which is more flat, is dominated by agricultural land (especially vineyards. Thus, La Peyne area shows, on a very short distance, a variety of soil types with mixed land use and semi-natural vegetation as well as open mine pits and lakes.

Spectral measurements are carried out using the ASD FieldSpec FR or GER2100 mini-IRIS RT (Figure 3). These spectrometers measure reflected energy from an object on the

earth surface, either in raw DN or reflectance values in the visible, near infrared and shortwave infrared parts of the spectrum (0.35 to 2.5 μm). Before taking measurements a calibration plate is used to determine the incoming radiation. Resulting spectral curves are very accurate duo to the fine spectral resolution (512 wavebands) so discrimination of chlorophyll, internal plant structure and minerals is possible. Ground Control Points (GCPs) are collected using the Differential GPS (Trimble: GeoExplorer II) or Garmin GPS 12XL. All data are stored in a Toshiba notebook.

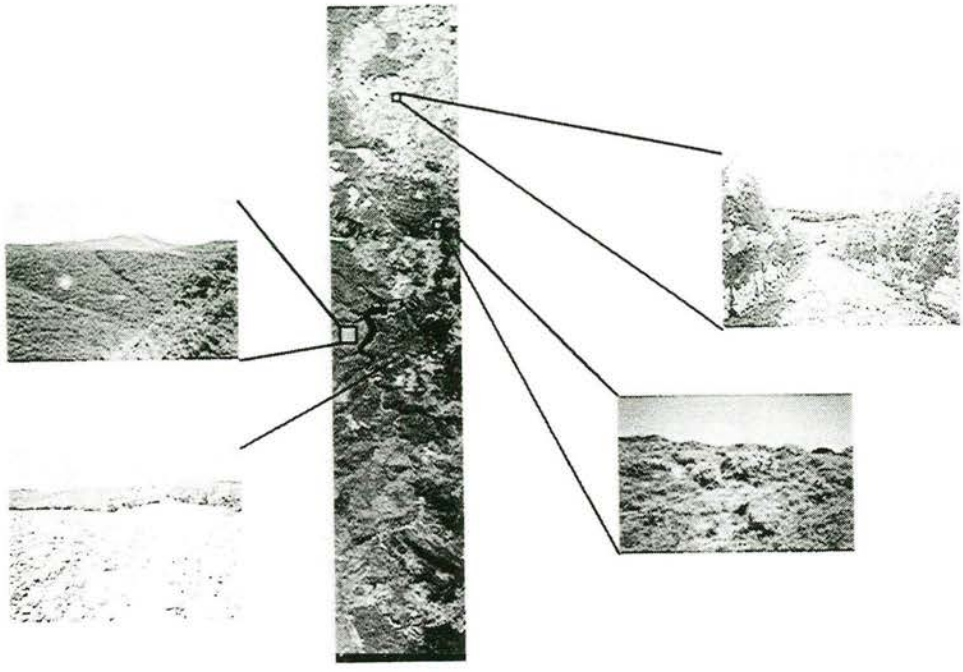

Figure 4. Impression of the Le Peyne test area. Middle part is the DAIS fcc image (RGD= bands 12, 7, 5). Inset photographs show the various target endmembers (left upper is a mixed oak forest, left lower is a bare agricultural field, right upper is a vineyard, right lower is garrigue; color plate 2).

A total of 1004 spectral measurements (350 to 2500 nm.) are stored into a spectral library. These accurate spectral reflectance curves can be used to simulate MERIS' spectral bands and may lead to standard product formulation (red edge and vegetation indices algorithms).

Instrument / Method	Object	No. Measurements
ASD FieldSpec FR	canopy	28
	Shrub	19
	Herbs	20
	Stones	39
	Other	22
	Transects	861
Laboratory chemical analysis	XRD-analysis	15
Method Pereira *et al.* (1994) and Floret *et al.* (1989)	Biomass	125
Trimble: GeoExplorer II	DGPS	69
Garmin 12XL	GPS	13

Table 1. Available data.

Transects along a line are measured to apply geostatistical analysis of the data in terms of spatial distribution of the existing ecosystems. To apply a geometric correction of the DAIS 69 ground control points (GCP) are collected. 15 XRD analysis of soil and rock samples are carried out to define the mineralogical content. All field data available to the project is summarized in Table 1.

4.3 MERISPEC CDrom installation

A Cdrom with the MERISPEC data base and software including detailed installation instructions can be obtained on request from:
Prof. Dr. F.D. van der Meer
ITC
Division of Geological Survey
Hengelosestraat 99
P.O. Box 6
7500 AA Enschede, the Netherlands
email: vdmeer@itc.nl
phone: +31-53-4874353
fax: +31-53-4874336
A description of the MERISPEC data base is provided in annex 1.

Chapter 5

MERIS' potential for mapping (soil) mineralogy

5.1 Introduction

Reflectance spectra have been used for many years to obtain compositional information of the Earth surface. It has been shown that spectral reflectance in visible and near-infrared offers a rapid and inexpensive technique for determining the mineralogy of samples and obtaining information on chemical composition. The MERIS standard band-set, with 15 narrow spectral bands in the 400 to 900nm. wavelength region potentially allows for the discrimination of minerals with absorption features due to electronic transition and charge transfer processes. Electronic transition and charge transfer processes (e.g., changes in energy states of electrons bound to atoms or molecules) associated with transition metal ions such as Fe, Ti, Cr, etc., determine largely the position of diagnostic absorption features in the visible- and near-infrared wavelength region of the spectra of minerals (Burns, 1970; Adams, 1974; 1975). Electronic transitions produce broad absorption features that require high energy levels and therefore take place at shorter wavelengths (Hunt, 1977). The position, shape, depth, and width of these absorption features are controlled by the particular crystal structure in which the absorbing species is contained and by the chemical structure of the mineral. Thus, variables characterising absorption features can be directly related to the mineralogy of the sample. The reflectance spectra of minerals are well known (for example Hunt & Salisbury, 1970, and subsequent papers in Modern geology). Reflectance spectra of minerals measured by different spectroradiometers with different spectral resolution are stored in spectral libraries that are available in digital format (e.g., Grove *et al.*, 1992; Clark *et al.*, 1990).

5.2 MERIS mineral index

We investigated the spectral properties of 160 minerals in the spectral library of Grove *et al.* (1992). In total, 74 of the 160 minerals investigated have absorption features in the wavelength range of MERIS. These were tabulated and the three most prominent absorption features in the 400-900 nm. wavelength range (covered by the MERIS sensor) were derived. These features were characterized in terms of their position, depth and area covered (we excluded width and asymmetry). The total area of an absorption feature is derived from the summation of the area left and right of the point of maximum absorption (position) measured

relative to the Hull following Green & Graig (1985). The upper convex Hull is an envelope curve fitted over the original reflectance spectrum having no absorption features. The absorption spectrum known as hull-quotient is given by taking the ratio between the reflectance spectrum and the enveloping curve. The result is a re-scaling of the reflectance spectra to 100% if no absorption features occur. The three most prominent absorption features for these minerals in the 400-900 nm. wavelength range were characterised by their position, depth and area covered. A MERIS mineral index was calculated by the summation of the depth and area products of the features and all 74 minerals were finally sorted in descending order on basis of the MERIS mineral index (MMI) value. Minerals having a high MMI value were expected to have high potential (from a spectral characteristics perspective) for mapping using MERIS. Examples of spectra of minerals with a high MMI are shown in Figure 1.

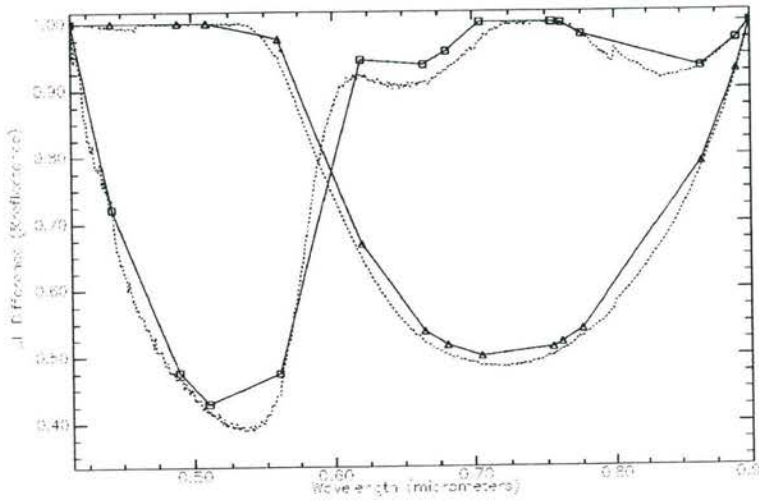

Figure 1. Example of Hull removed spectra for MERIS (solid line with indicating band center positions) and full range (dotted line) for spectra with a high MMI (square is hematite, triangle is stibnite).

The results are shown in Table 1 in which the top 26 minerals are portrayed. When reviewing this it is obvious that many of these are ores which have no relevance to the mission of MERIS nor do they have any likeliness of being mapped at the spatial resolution as foreseen for MERIS. Examples are stibnite (principal ore of antimony), malachite (minor ore of copper), beryl (ore of beryllium occurring in granitic pegmatites), realgar, azurite (ore of copper), siderite (iron ore often found as nodules), ferroxaxinite (iron ore), molybdenite (principal ore of molybdenum), sulfur, antophyllite (amphibole of the asbestos-group), brucite (mineral of the serpentine-group), rhodochrosite (principal ore of manganese) and talc (hydration of magnesium silicates such as olivine). Some are rock-forming minerals which are not likely to be found in substantial amounts at the resolution imaged by MERIS. Example are sodalite (blue feldspar occurring in igneous rocks), enstatite (pyroxene and primary mineral of basic igneous rocks), cordierite (common mineral of metamorphic rocks), and hypersthene (pyroxene occurring in many igneous rocks). Alteration minerals appear that have potential and are significant in soil mineralogy: hematite (iron mineral and ore of iron that occurs in many rocks as primary mineral but also as alteration product in soils), goethite (iron mineral that occurs as weathering product often in gossans) and jarosite (an hydrothermal alteration product found in copper deposits). Thus in the remainder of the paper we emphasise the use of MERIS for mapping surface (soil) mineralogy using the examples of goethite and hematite. As jarosite is an alteration mineral associated with copper/sulphide waste deposits, it is not further analyzed since it reflects an applications outside the MERIS science objectives.

Mineral	Class	1_pos	1_depth	1_area	2_pos	2_depth	2_area	3_pos	3_depth	3_area	Index
Stibnite	Sulphides	0.737	30.7989	7.7835							239.7232
Malachite	Carbonates	0.456	1.056	0.0381	0.665	24.46	8.28				202.569
Enstatite	Inosilicates	0.503	1.6367	0.019	0.547	1.4545	0.0295	0.904	25.22	6.508	164.2058
Beryl	Cyclosilicates	0.425	1.274	0.0186	0.808	23.986	5.8218				139.6654
Sodalite	Tectosilicates	0.646	24.8	5.1656							128.1069
Realgar	Sulphides	0.558	28.38	3.5153							99.76421
Hematite	Oxides	0.556	14.13	1.74	0.653	4.217	0.307	0.9	19.26	3.83	99.64662
Lithiophilite	Phosphates	0.469	8.15	0.17	0.603	14.38	0.93	0.908	17.3	3.21	70.2919
Azurite	Carbonates	0.676	13.6547	4.84							66.08875
Crysoprase	Tectosilicates	0.651	19.85	3.116							61.8526
Antlerite	Sulphates	0.456	2.0318	0.1343	0.65	12.59	4.147				52.4836
Siderite	Carbonates	0.484	4.3695	0.1972	0.515	4.478	0.188	0.884	15.196	3.341	52.47337
Ferroaxinite	Cyclosilicates	0.437	3.77	0.109	0.59	9.52	1.955	0.944	13.353	2.1549	47.79691
Atacamite	Halides	0.677	11.199	4.182							46.83422
Rhodonite	Inosilicates	0.411	6.0217	0.1743	0.554	11.116	0.9572	0.964	13.23	2.32	42.38342
Gahnite	Oxides	0.459	4.014	0.0924	0.621	17.16	2.28	0.792	9.56	0.133	40.76717
Cordierite	Cyclosilicates	0.588	6.3996	1.1418	0.932	12.863	2.5074				39.55975
Hypersthene	Inosilicates	0.912	14.04	2.336							32.79744
Jarosite	Sulphates	0.444	2.683	0.164	0.58	3.214	0.2897	0.908	11.57	2.5468	30.83758
Molybdenite	Sulphides	0.653	9.7243	0.5995	0.589	8.9269	0.8836	0.701	8.6156	1.9728	30.71438
Sulfur	Elements	0.44	22.6451	1.095							24.79638
Anthophyllite	Inosilicates	0.928	10.97	2.178							23.89266
Brucite	Hydroxides	0.515	1.2417	0.0243	0.731	3.0868	0.046	0.994	11.56	2.049	23.85861
Rhodochrosite	Carbonates	0.406	18.45	0.1366	0.446	8.33	0.3	0.551	15.054	0.915	18.79368
Goethite	Hydroxides	0.503	8.156	0.7789	0.665	2.4675	0.2197	0.932	7.3	1.52	17.99082
Talc	Phyllosilicates	0.647	3.45	0.2667	0.852	7.713	2.0445				16.68934

- A1, A2 and A3 are the three most prominent absorption features in the MERIS wavelength range with position, depth and area given.
- INDEX is the sum of the area and depth for the features occurring, minerals are sorted on the basis of the index value.

Table 1. Classification of minerals from Grove et al. (1992) according to potential for identification by MERIS.

5.3 MERIS data simulation for mineral mapping; practical application

In this study, airborne imaging spectrometer data from the Australian sensor HyMAP were used acquired during the HyEUROPE 99 campaign over the Tabernas area of SE Spain. The Tabernas area is located 20 km. north of Almería in southern Spain. The Tabernas basin (Kleverlaan, 1989; Figure 2) is a structural depression in the Alpine nappes of the Betic Cordilleras of southern Spain bounded by major strike-slip faults. The mountain ridges on each side of the basin prevent precipitation and have lead to pronounced desertification. The terrain is relatively flat and devoid of vegetation. During the Tortonian to Pleistocene the Tabernas basin tectonically subsided causing the development of an alluvial fan system grading southward into a submarine fan system. The alluvial fan system is characterized by progressive southward decrease of grain size of clastics from cobble size to sand and clay size. The submarine fan system has a variety of lithologies ranging from shallow marine carbonate reef and platform limestones through marls to turbidites and debris flows.

Metamorphic rocks of the Nevado Filabride and Alpujarride complexes form the basement of the Tabernas basin. Overlying these are Serravalian-Quaternary deposits grouped into five formations recognized throughout many Tertiary basins in southern Spain: the Chozas formation, Turre formation, Yesares formation, Abrioja formation, and Gador formation.

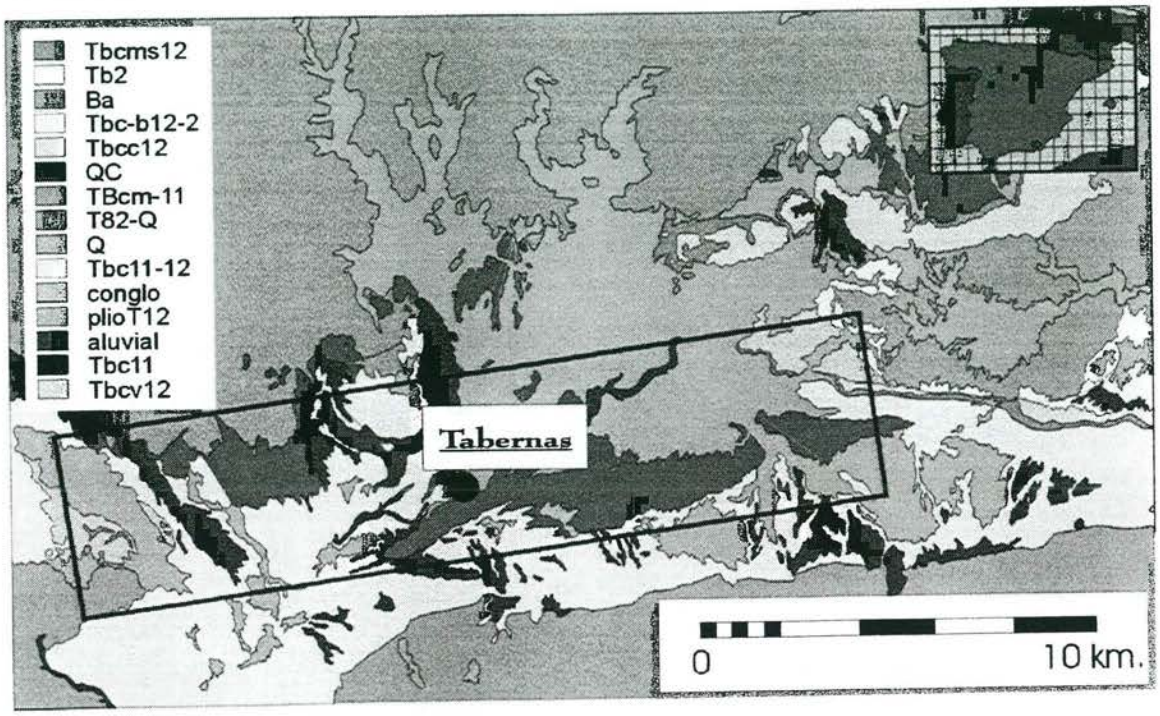

Figure 2. Geological map of the Tabernas area (Almeria province, SE Spain). Legend to the codes (corresponding to the 1:50.000 geological map sheet), Tbcms12=Sandstone and marls (Early Andalucian), Tb2=Sandstones (Middle Pliocene), Ba=Basement of Malaguide and Alpujarride unites, Tbc-b12-2=Calcarenites (Early Pliocene), Tbcc12=Limestones (Middle Andalucian), Qc=Colluvial (Quaternary), Tbcm-11=Conglomerates and marls (Middle Tortonian), T82-q=Conglomerates, sandstones and siltstones (Quaternary), Q=Alluvial material (Quaternary), Tbc11-12=Marls and sandy marls (Late Tortonian-Early Andalucian), Conglo=Conglomerates (Tortonian), Pliot12=Conglomerates (Pliocene), Aluvial=Alluvial (Quaternary), Tbc11=Conglomerates and sandstones (Early-Middle Tortonian), Tbcv12=Gypsum (Late Andalucian). HyMAP data strip is indicated with box (color plate 3).

The Serravalian-Early Messinian Chozas formation unconformably overlies the basement which formed a pronounced relief from Serravalian times onward. The northern coastline of the basin contained steep cliffs fringed by coral reefs which were locally breached by conglomerate-filled depressions and a channel complex feeding a small submarine fan system. This system overlies starved basin muds and continental coarse detritus of a fan delta and alluvial fan. During the deposition of the sediments of the Turre formation of Early Messinian age, rapid basement uplift gave rise to deposition of conglomerates and limestone reefs at the basin margin and mudstone laminites in the centre of the basin.

The Yesares formation of Messinian age consists of selenitic gypsum with laminite intercalations recording an evaporitic phase due to continued rise of the basin and eventually subaerial exposure. During the start of the Pliocene the Tabernas basin experienced renewed subsidence and subsequent uplift and folding resulting in subaerial exposure and erosion of older units. The Abrioja formation of Pliocene age unconformably overlies older units and consists of pebbly mudstones overlying a basal conglomerate. Local interfingering with laminated mudstones indicate deposition in a shallow warm sea of maximally 75m. depth. Continued basement rise in Plio-Pleistocene resulted in continental deposits of the Gador

formation which are contemporaneous with the deposits of the Abrioja formation. Sediments of the Gador formation were deposited on alluvial fans and coastal plains grading southward into a fan delta system. Quaternary deposits show two conspicuous levels of river terraces. Figure 3 shows a field photograph to illustrate the remote sensing potential of the area.

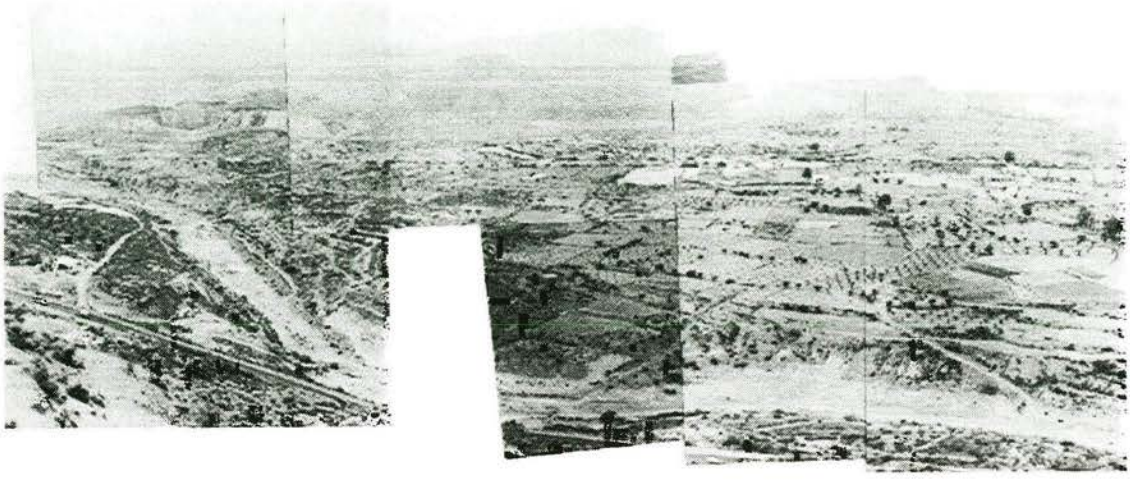

Figure 3. Field photograph of the desert around Tabernas (SE Spain, Almeria Province; color plate 4).

On June 2, 1999 flights were conducted over the Tabernas area with HyMAP (Figure 4). The bandwidth (measured as FWHM) of the HyMAP which is in the range of 12 to 20 nm. is broader than those for MERIS which lie between 2.5 and 20 nm. This implies that only band matching (i.e., selecting the band which center is closest in wavelength to the center of the channel to be simulated) can be used. The channel mismatch occurring is plotted in Figure 5 for all simulated MERIS channels.

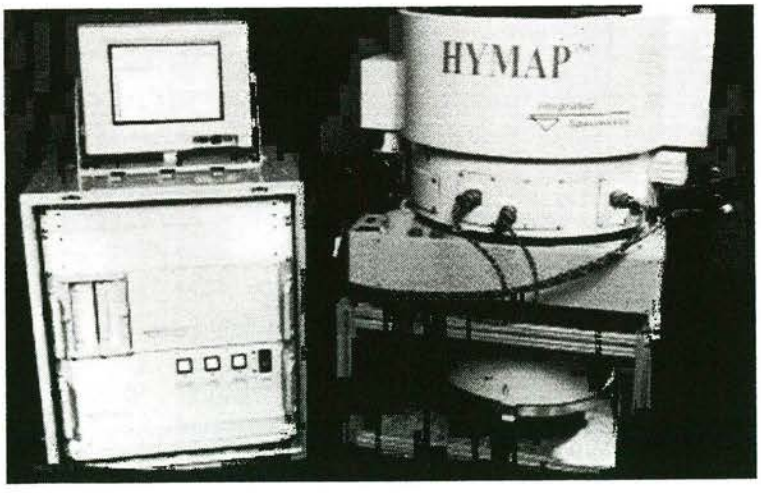

Figure 4. Photograph of the HyMAP sensor (Courtesy of Integrated Spectronics Ltd.).

The Hyperspectral Mapper (HyMAP) is a 128 channel imaging spectrometer that has spectral coverage in VIS,NIR, SWIR, bandwidths generally in 10 - 20 nm. range, a high signal to noise ratio (>500:1), 2 - 10 m. spatial resolution and a 60-70 degree swath. Table 2 shows the first 35 channels of the HyMAP (position and FWHM) and the matching with the 15 MERIS channels. The HyMAP data was corrected to reflectance using ATCOR4 which uses the MODTRAN RT code. The procedure is not further discussed, the interested reader is

referred to Richter (1996). A "MERIS" data cube with spectral dimensions of the MERIS sensor was extracted from the HyMAP data by band matching. This data set was subsequently coarsenend by spatial degradation from the original 10 m. FOV to the MERIS resolution of 300 m. At the various spatial resolutions, surface mineralogy maps for two endmembers, goethite and hematite, were derived using the CCSM (see section below) algorithm. The results were validated using the original HyMAP estimated goethite and hematite mineral maps (i.e., with all 128 channels at the full resolution of 10m, assuming this to be the "true" mineralogy or "best" estimate). Furthermore, the results were validated using an internal approach in CCSM. The CCSM will be further explained below.

HyMAP			MERIS		
Band	Wavelength	FWHM	Band	Wavelength	FWHM
1	0.403	0.0130000	1	0.4125	0.01
2	0.447	0.0140000	2	0.44250	0.01
3	0.457	0.0147000			
4	0.472	0.0159000			
5	0.487	0.0180000	3	0.49000	0.01
6	0.503	0.0160000			
7	0.517	0.0163000	4	0.51000	0.01
8	0.533	0.0170000			
9	0.549	0.0159000			
10	0.563	0.0140000	5	0.56000	0.01
11	0.580	0.0146000			
12	0.594	0.0152000			
13	0.609	0.0163000			
14	0.624	0.0186000	6	0.62000	0.01
15	0.641	0.0152000			
16	0.656	0.0156000			
17	0.671	0.0156000	7	0.66500	0.01
18	0.685	0.0147001	8	0.68125	0.0075
19	0.702	0.0172000	9	0.70500	0.01
20	0.716	0.0162000			
21	0.731	0.0155000			
22	0.747	0.0155000	10	0.75375	0.0075
23	0.761	0.0156000	11	0.76000	0.0025
24	0.777	0.0164000	12	0.77500	0.015
25	0.792	0.0160000			
26	0.807	0.0161000			
27	0.823	0.0167000			
28	0.837	0.0154001			
29	0.854	0.0190000			
30	0.868	0.0164000	13	0.86500	0.02
31	0.883	0.0166000			
32	0.885	0.0192000	14	0.89000	0.01
33	0.896	0.0137000			
34	0.900	0.0210000	15	0.90000	0.01
35	0.918	0.0158000			

Table 2. Comparison of the band matching of HyMAP and MERIS.

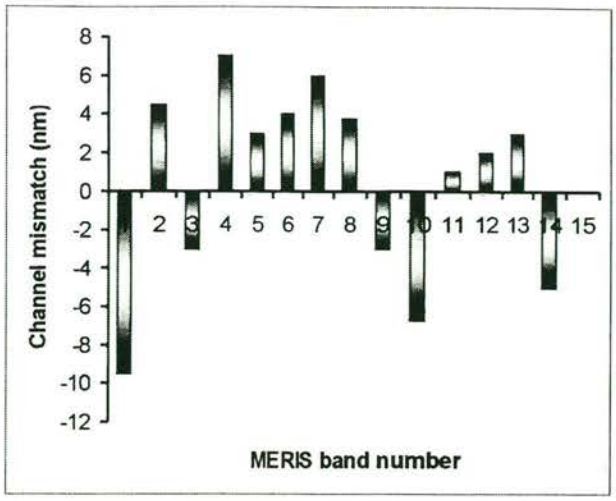

Figure 5. Channel mismatch (HyMAP center position subtracted from the MERIS center position) for the 15 simulated MERIS channels (see also Table 2).

5.4 Surface (soil) mineralogy mapping using CCSM

The Cross Correlogram Spectral Matching algorithm (CCSM; Van der Meer & Bakker, 1997a+b) allows to match unknown pixel spectra with known laboratory or field spectra by deriving statistics from single pixel correlogram functions. Reference spectra can be selected from a spectral library with the same spectral dimensions as the data cube or from the scene itself. A pixel cross correlogram is constructed by calculating the cross correlation coefficient between a test spectrum (a pixel spectrum) and a reference spectrum (a laboratory or pixel spectrum known to characterise a material of interest) at different match positions. By convention, the reference spectrum is moved and negative match positions are referred to when shifting toward shorter wavelengths while positive match positions indicate a shift towards longer wavelengths. The cross correlation is calculated as

$$r_m = \frac{n\Sigma\lambda_r\lambda_t - \Sigma\lambda_r\Sigma\lambda_t}{\sqrt{[n\Sigma\lambda_r^2 - (\Sigma\lambda_r)^2][n\Sigma\lambda_t^2 - (\Sigma\lambda_t)^2]}}$$

where r_m is the cross correlation at match position m, λ_t is the test spectrum, λ_r is the reference spectrum, n is the number of overlapping positions (spectral bands), and m the match position. The statistical significance of the cross correlation coefficient can be assessed by the following t-test

$$t = r_m\sqrt{\frac{n-2}{1-(r_m)^2}}$$

which has (n-2) degrees of freedom. This statistical measure tests the null hypothesis which states that the correlation between the two spectra at a specific match position is zero. A pixel cross correlogram is calculated for n match positions.

From the cross correlogram images the significance is derived, the t-values are calculated and averaged and re-scaled from 0 to 1 by dividing them by the t-value obtained at the reference pixel, and the skewness is calculated and re-scaled between 0 and 1 by taking the absolute value of the sum of the correlation at m=2 and m=-2 divided by 2 and subtracted from 1. Thus, pixels having a low skewness (i.e., a symmetric cross correlogram) have a re-scaled value near to 1 while pixels with a skewed cross correlogram have values near to 0 on this scale. We have extracted the pixels with values exceeding 0.9 in all three of these parameters (i.e., cross correlation at m=0, significance, skewness) and assigned them to the

reference pixel material to obtain surface (soil) mineralogy maps. The procedure was applied to the endmembers goethite and hematite.

In order to evaluate the surface mineralogy maps, a root mean square (RMS) is calculated from the difference between the calculated pixel cross correlogram and the ideal cross correlogram calculated for the reference as:

$$RMS = \sqrt{\frac{\sum_0^M (R_M - R'_M)}{N}}$$

where R_M is the pixel cross correlation at match position m, R'_M is the reference cross correlation at match position m, N is the number of match positions, M is the match number.

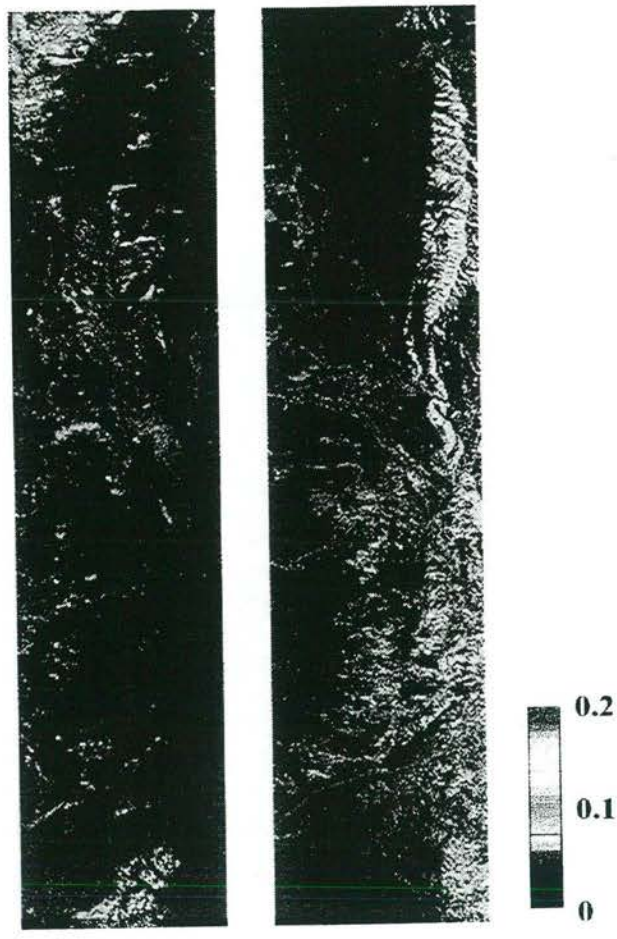

Figure 6. Surface mineralogy maps, endmember goethite (left) and hematite (right), derived from CCSM using MERIS simulated data at 10m. resolution. The classified pixels are color coded using the CCSM calculated pixel RMS values (values in bar; color plate 5).

5.5 Validation of surface mineralogy maps

Surface (soil) mineralogy maps for the endmembers goethite and hematite were derived using the CCSM procedure applied to "MERIS" 15 channel imaging spectrometer data at spatial resolutions ranging from 10 to 300 m. Surface mineralogy maps for goethite and hematite are shown in Figure 6. The results were validated using three criteria:

1. The misclassification was calculated by comparing the derived surface mineralogy maps with a standard set derived from the original HyMAP data for goethite and hematite. This standard set was perceived as the "best estimate" or "true surface mineralogy" in the

absence of field observations. The ratio of the areal extent of misclassified pixels over the areal extent of classified pixels was calculated for the purpose.

2. The average RMS value for the classified pixels derived from the CCSM algorithm was calculated.
3. The local variance following the procedure of Woodcock & Strahler (1987) was derived to retrieve the optimal spatial sampling for mineral mapping. In this method $z(x_{ij})$ is the value of the pixel located at x_{ij} in the ith row and the jth column of an image. The local variance is computed over a (2n+1) x (2m+1) window by

$$\sigma_{ij}^2 = 1/(2n+1)(2m+1)\sum_{k=i-n}^{i+n}\sum_{l=j-m}^{j+m}\{z(x_{kl}) - u_{ij}\}^2$$

where u_{ij} is the mean of the (2n+1) x (2m+1) window centered on x_{ij}. The local variance can be computed for varying pixel sizes using degraded image products. A plot of local variance versus pixel size allows selection of the optimal pixel size corresponding to the peak in variability in the curve.

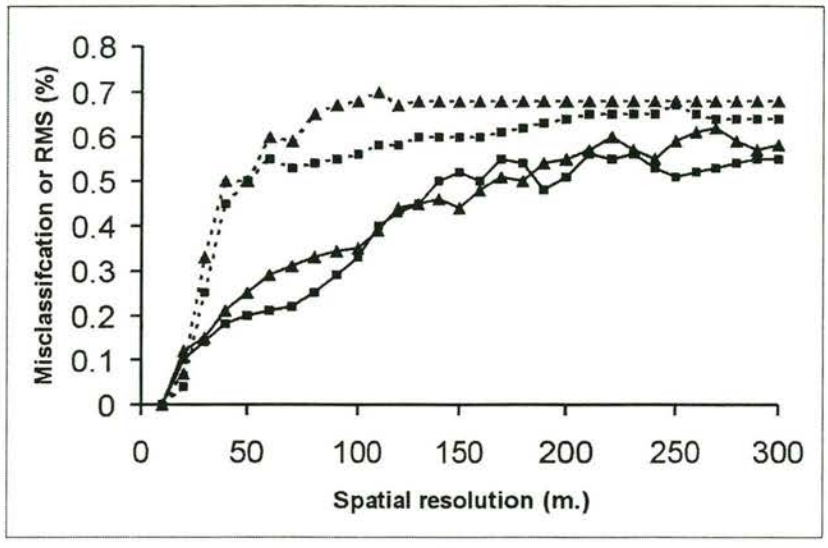

Figure 7. Plots of misclassification (ratio of misclassified over total classified area) and average RMS from CCSM for goethite and hematite (solid lines are RMS, dotted lines are misclassification, square is goethite, triangle is hematite).

5.6 Results

The derived misclassification and RMS values for the goethite and hematite mineral maps at the various resolutions are presented in Figure 7. The results show that the accuracy of the predictions decrease rapidly with resolution. Although up to expert judgement, we feel that unacceptable large errors occur for resolutions of 50m. and larger. Thus using MERIS for mineral identification in search for pure targets is meaningless, although the sensor from a spectroscopic perspective offers potential for locating areas of higher and lower iron oxide mineral features. The local variance plots (Figure 8) for goethite and hematite show that in both cases the optimal sampling size is much lower than the 300 m. resolution of MERIS. Obviously at the 300 m. resolution it is unlikely to find single-mineral homogenous areas covering the FOV of the sensor, most pixels will be a mixture containing some mineral percentage. The goethite endmember has a larger (20-30 m.) optimal sampling interval due to the type of occurrences in the area. Goethite occurs as weathered caps whereas the hematite occurs in disseminated form in soil and rock, hence the lower (<10m.) optimal pixel size.

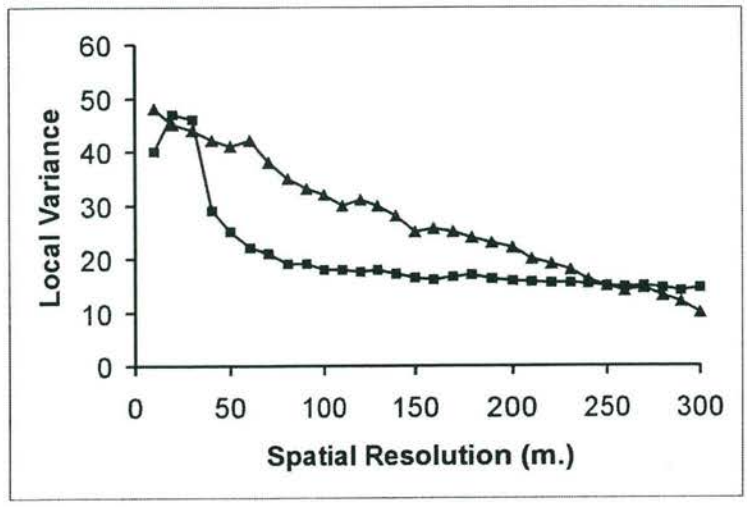

Figure 8. Plots of local variance versus spatial resolution for goethite and hematite. The peaks in the curves indicate the optimal sampling interval (square is goethite, triangle is hematite).

5.7 Conclusions

Based on the definition of the channels (position and FWHM) MERIS' is able to identify a suite of minerals with absorption features in the visible and near-infrared part of the wavelength spectrum. However, most of the minerals having a high MERIS mineral index were found to be ore minerals (or related alteration products) that are unlikely to be "seen" at the resolution of MERIS. Thus it was decided to concentrate the research on hematite and goethite which do occur in soil and weathered caps. The HyMAP, airborne hyperspectral sensor, has an excellent spectral co-registration with the proposed MERIS channels and as such can be used to simulate MERIS data. The average misfit of the channels from HyMAP and MERIS is only in the order of 3-5 nm. with a maximum of 9 nm. Although the FWHM of the HyMAP does not allow convolution but merely band matching, a reliable simulation was performed. In the absence of point spread functions (PSF) for MERIS, spatial degradation was done assuming a gaussian PSF. Comparison of the mapping (using the CCSM algorithm) with "true" mineral maps for hematite and goethite (derived from the 10m. HyMAP data) shows that the prediction accuracy decreases rapidly when increasing the spatial resolution. This may be attributed to the mixed nature of the pixels at higher field-of-views. The optimal sampling size in case of goethite was found to be between 20 and 30 m. while for the hematite a value of less than 10m. was obtained. This is related to the nature of occurrence of the minerals: goehite occurs as large, rather homogenous caps while the hematite occurs in a more disseminated manner.

Chapter 6

Vegetation indices for simulated MERIS images

6.1 Introduction

Vegetation Indices (VI) derived from satellite images are one of the important sources for the monitoring of vegetation conditions and mapping land cover changes on regional, continental and global scales. Especially global vegetation monitoring is a main issue for the European Union because physically based vegetation indices may retrieve key variables in modelling plant productivity (and thus carbon sequestration), surface-atmosphere gas exchanges and energy transfers at the land surface.

The repetitive acquisition of vegetation index measurements should allow to much improved description of the dynamics of ecosystems, the quantification of deforestation and desertification processes, the monitoring of biomass burning and agricultural production and the documentation of land cover changes (Verstraete *et al.*, 1995). Reflectance characteristics of vegetation in the visible region of the spectrum are dominated by the absorption properties of photosynthetic pigments (Asrar, 1989; Curran *et al.*, 1991). This is especially true in the red region, where chlorophyll in the leaves strongly absorbs energy. In the near infrared part of the spectrum, reflectance increases due to the internal structure of the leaves. Sensors with spectral bands in the red (*red*) and near infrared (*NIR*) lend themselves well to vegetation monitoring since vegetation indices are based on ratios of the radiance in red and near-infrared bands, chosen to maximize the reflectance contrast between vegetation absorption and reflection. Vegetation indices have been shown to be a strong indicator of the amount of photosynthetically active green biomass (PAGB; Teillet *et al.*, 1997). The most popular and wide spread used vegetation index is the Normalized Difference Vegetation Index (NDVI) defined as

$$NDVI = (NIR - red) / (NIR + red)$$

Various authors investigated NDVIs from remote sensing imagery with the purpose of assessing biophysical plant canopy properties (Pinty *et al.*, 1993), establishing its relationship to biomass (Tucker, 1979; Elvidge & Lyon, 1985) and leaf area index (LAI; Clevers, 1988). Although commonly used, several drawbacks of the NDVI were found. Hill (1995) points out that the vegetation index is influenced by the state of the atmosphere, illumination and observation geometry and background reflectance of soils and rocks. The perpendicular vegetation index (PVI; Richardson & Wiegand 1977) was introduced to incorporate background effects. The index assumes that the perpendicular distance between pixels from the soil line (in the red-near infrared space) is linearly related to the vegetation cover.

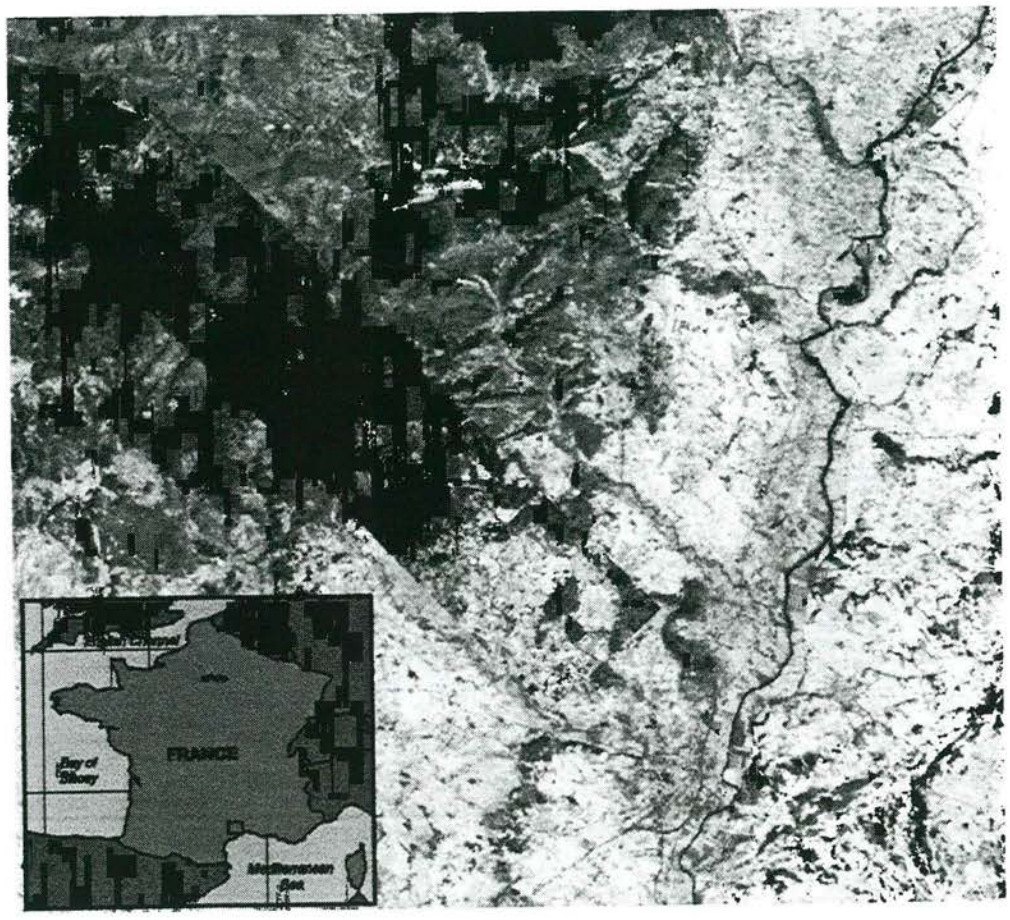

Figure 1. Location of the Le Peyne test site. Landsat TM color composite (1 May 1995, upper left corner is N 43° 38', E 03° 12', lower right corner is N 43° 19', E 03° 35') with DAIS strip plotted. River on the Landsat image is the Herault, the lake is Lac du Salagou (color plate 6).

For a given soil, the red (*red*) and near infrared (*NIR*) reflectances are related by the equation of the soil line as

$$NIR = a \cdot red + b$$

where a is the slope and b is the offset of the soil line. An index related to the PVI is the Weighted Difference Vegetation Index (WDVI) of Clevers (1988). Alternative indices have thus been developed using near infrared and red bands. Pinty & Verstraete (1991) developed the Global Environmental Monitoring Index (GEMI) to compensate for atmospheric and illumination conditions. Huete (1988) introduced the Soil Adjusted Vegetation Index (SAVI) to take into account the reflectance contributions from background substrates. The initial construction of this index was based on measurements of cotton and range grass with dark and light soil backgrounds, and the adjustment factor L was found that gave equal vegetation index results for the dark and light soils. The standard value typically used in most applications is 0.5, which was established for intermediate vegetation densities. An alternative vegetation index is developed by Baret *et al.* (1989) and Baret & Guyot (1991): the Transformed Soil Adjusted Vegetation Index (TSAVI). This index assumes that the soil line has an arbitrary slope and intercept. The parameter 'X' was 'adjusted to minimize the soil background effect (Baret *et al.*, 1989)'. The X-value reported in Baret & Guyot (1991) is 0.08. Qi *et al.* (1994) introduced the Modified Soil Adjusted Vegetation Index (MSAVI) to provide a variable correction factor L instead of the rigid L factor of the SAVI. The second Modified Soil Adjusted Vegetation Index (MSAVI2; Qi *et al.*, 1994) uses an

iterative process to substitute the MSAVI(n-1) as the L factor in MSAVI(n). For MERIS, a Global Vegetation Index (MGVI) is developed following a physical and mathematical model description using three MERIS bands (Gobron *et al.* 1999). Here we restrict to the known near infrared and red band vegetation indices and compare their performance at the various spatial scales of observation.

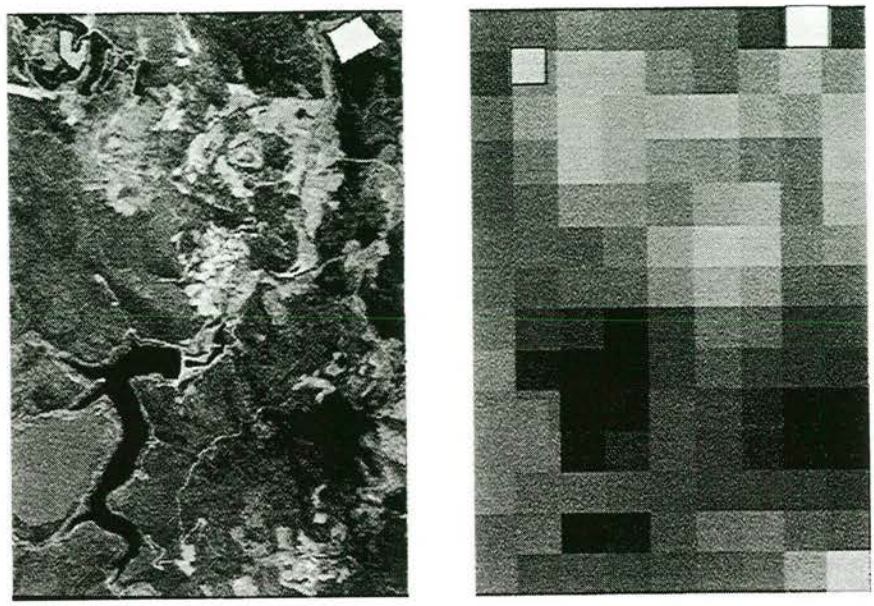

Figure 2. Selection of regions of interest (ROIs) on basis of land cover units and available biomass data for mixed oak forest (red), garrigue (yellow), and pine forest (green). Not shown are the ROIs for maquis and agricultural fields (color plate 7).

In this Chapter attempts are made to investigate the accuracy of different vegetation indices on different spatial image scales using spatially degraded DAIS7915 image cubes to simulated MERIS images. A second aim of this chapter is to estimate the amount of above ground biomass out of MERIS images using MERIS' best vegetation index. The third aim is to develop a Red Edge algorithm which can be used as standard MERIS product (i.e. ecosystem monitoring) formation as well as global vegetation condition monitoring. This will be discussed in the next chapter.

6.2 Data sets and methodology

The DAIS data used for this study were acquired over the Peyne catchment area in southern France, roughly between Montpellier and Béziers (Figure 1). The area consists of two different parts: an upper part and a lower part. The upper part is characterised by a hilly terrain covered by a mixed oak forest of Mediterranean sclerophylous species. The dominant species are holm oak (Quercus ilex), the downy oak (Quercus pubescens), the strawberry tree (Arbutus Unedo) and the Erica tree (Erica arborea). Various disturbances of the forest coverage are found due to open mining of bauxite and dolomite. The lower part, which is more flat, is dominated by agricultural land (especially vineyards).

The Peyne river is a tributary of the Hérault river and is located in central southern France, roughly between Montpellier and Béziers. The catchment is located at the edge of the Massif Central, the 'Montagne Noir' and the coastal plain of the Mediterranean sea. As a result of this, the Le Peyne catchment displays a large variety of soil and rock types from north to south. The flight lines of DAIS were chosen in such a way that they cover as much as possible variation in geology, soils and vegetation. The physiographic sections that can be

distinguished from south-east to north-west are as follows. The southern part consists of Tertiary marl and limestones. The rivers Peyne and Hérault have locally deposited recent fluvial material on top of these formations. Moving north-west Triassic marls and sandy dolomites are surfacing. Next, a complex area of Paleozoic flysch and conglomerates is situated around the artificial lake of Vailhan. The northern part of the DAIS flight strips are covered by Permian reddish clayey marls. At various locations in the study area, basalt and tuff formations are found documenting volcanic activities dated Pliocene.

The land use in the southern flat part of the Le Peyne catchment is predominantly vineyards. The northern part is characterized by a hilly terrain covered by a mixed oak forest of Mediterranean sclerophylous species. Depending on water availability, forest fire and human disturbance the forest is a closed Maquis type of forest or a more open Garrigue type of vegetation. Various disturbances of the forest coverage are found due to open mining of bauxite and dolomite. The landscape of the abandoned mines is not restored by afforestation but the areas are simply left behind and natural re-growth occurs slowly.

Five strips with the DAIS were flown in the Le Peyne catchment on 8 July 1997. The strips were located in such that they covered most the significant variation in the lithological and vegetation setting of the area. Three flight tracks were located between the 'Basin de Thau' in the South-West (N:43°19', E:03°35') and the dolomite mine of Carlenças in the North-East (N:43°38', E:03 °12') and two tracks were located between the town of Montblanc in the south (N:43°22', E:03°20') and over Lac du Salagou in the North (N:43°44', E03°20'). The weather conditions were very good during the flight. Mistral winds in the preceeding days had blown away aerosols and moisture. The last significant rain occurred 10 days before the date of the flight. In June of 1998 additional experimental flights were carried out over the Peyne area.

The 79-channel Digital Airborne Imaging Spectrometer (DAIS 7915; Chang *et al.* 1993) built by the Geophysical Environmental Research corp. (GER) is the successor of the 63-channel imaging spectrometer GERIS (Collins & Chang 1990). The instrument covers the spectral range from the visible to the thermal infrared wavelengths at variable spatial resolution from 3 to 20 m. depending on the carrier aircraft flight altitude. Six spectral channels in the 8 - 12 µm. region could be used for the retrieval of temperature and emissivity of land surface objects. These and 72 narrow band channels in the atmospheric windows (e.g. those wavebands that pass relatively undiminished through the atmosphere) between 0.450 and 2.45 µm. are sensed using four spectrometers:

spectrometer 1: 0.4 - 1.0 µm. 32 Bands Bandwidth = 15-30 nm. Detector: Si
spectrometer 2:1.5 - 1.8 µm. 8 Bands Bandwidth = 45 nm. Detector: InSb
spectrometer 3: 2.0 - 2.5 µm. 32 Bands Bandwidth = 20 nm. Detector: InSb
spectrometer 3: 3.0 - 5.0 µm. 1 Band Bandwidth = 200 nm. Detector: InSb

The main radiometric and geometric parameters include:

Dynamic range: 15 bit

Sensitivity	VIS/NIR:	NER < 0.025 mW/cm²sr µm.
	SWIR:	NER < 0.025 mW/cm²sr µm.
	MIR/TIR:	NET < 0.1 K.
FOV:	0.894 rad. (26 degrees) on DO 228, depending on aircraft max. 39	
IFOV:	3.3 mrad. (0.189 degrees)	
GIFOV:	depending on aircraft altitude 5 - 20 m.	
Scan-frequency:	adjustable according to aircraft altitude between 6 and 24 Hz.	
Image pixels per line:	512	

More details can be found in Strobl *et al.* 1996).

The DAIS image was calibrated to radiance at DLR and radiometric corrected using the empirical line method (Kruse *et al.,* 1990) with dolomite, water, bauxite and a bare agricultural field spectrum. Geometric correction was more complex (De Jong *et al.*, 1998; Scholte *et al.*, in press). Usually airborne datasets are not oriented towards the north because of disk space requirements, but rather stored in a file in the flight direction of the aircraft. In order to match the geometric projection of the dataset, two corrections should be applied:

(1) an image rotation from the aircraft heading towards the north and (2) image to map registration using ground control points and polynomial warping. Variations in platform altitude, attitude and velocity (pitch, roll and yaw) can be very large for aircraft. For satellite imagery (recorded from stable platforms), first order geometric transformation functions are sufficient, aircraft data, however, sometimes require higher order polynomials and hence more ground control points (GCPs). For this purpose a geostatistical approach using Moving Neighbourhood Kriging (see Appendix 2) is developed and applied to predict GCPs from a set of measured DGPS samples. Another advantage is that the geostatistical approach gives information about the direction of the error and thus flight direction (this information was missing due to failure of a gyroscope). The resulting RMS-error decreased with almost 20% to 8.85 pixel which seemed to be as accurate as possible (for more details see appendix 2). In 1996, 1997 and 1998 field spectral measurements of soil and vegetation are collected using the ASD FieldSpec-FR. The 1996 and 1997 field campaign is carried out on behalf of the DeMon project, in which the latter one only exists of soil and bedrock samples. In June 1998 spectral measurements are taken for the BCRS MERILand project.

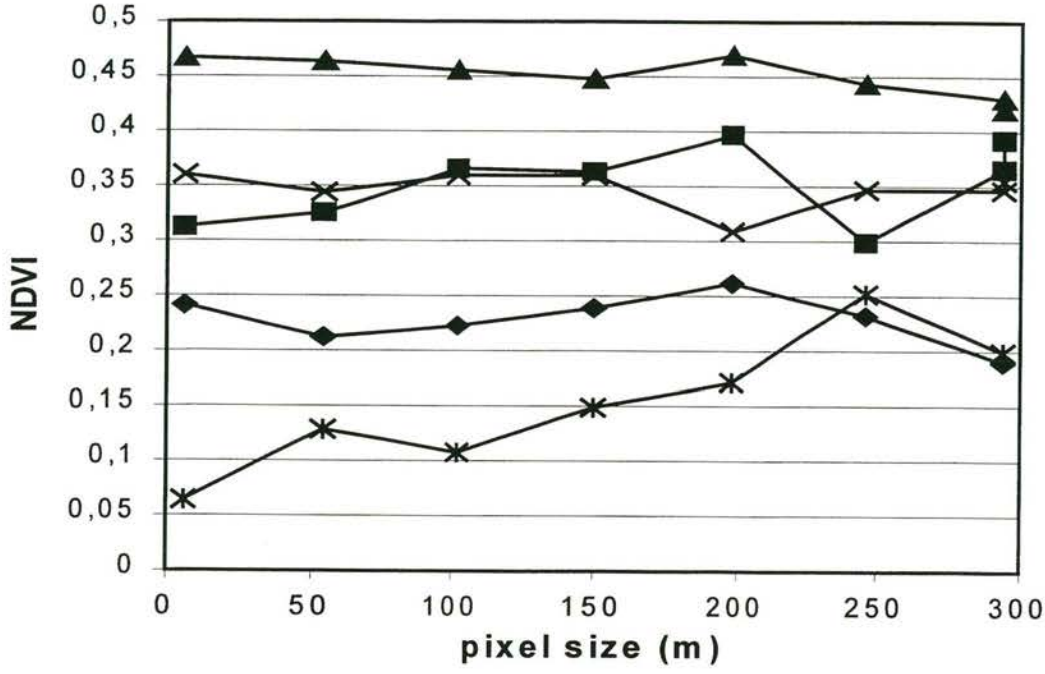

Figure 3. NDVI results emphasizing the spectral domain for garrigue, maquis, mixed oak forest, pine forest and a bare agricultural field (abandoned vine yard, ploughed) at different spatial scales (symbol for the endmembers: garrigue = diamond, maquis = square, mixed oak forest = triangle, pine forest = cross, bare agricultural field = star).

The ASD FieldSpec FR measures the reflected energy from an object on the earth surface, either in raw DN or reflectance values. Before taking measurements a calibration ($BaSO_2$) plate is used to determine the incoming radiation. The FieldSpec FR spectroradiometer combines three spectrometers to cover the entire solar reflected portion of the spectrum, 350 to 2500 nm. in 512 wavebands. A photo diode array spectrometer is used to cover the 350 to 1000 nm. spectral range (UV/VNIR), while two fast scanning spectrometers provide coverage for the wavelength range from 1000 to 2500 nm. (SWIR 1 and 2). The probe end has an 18° field-of-view, so the target area can be calculated.

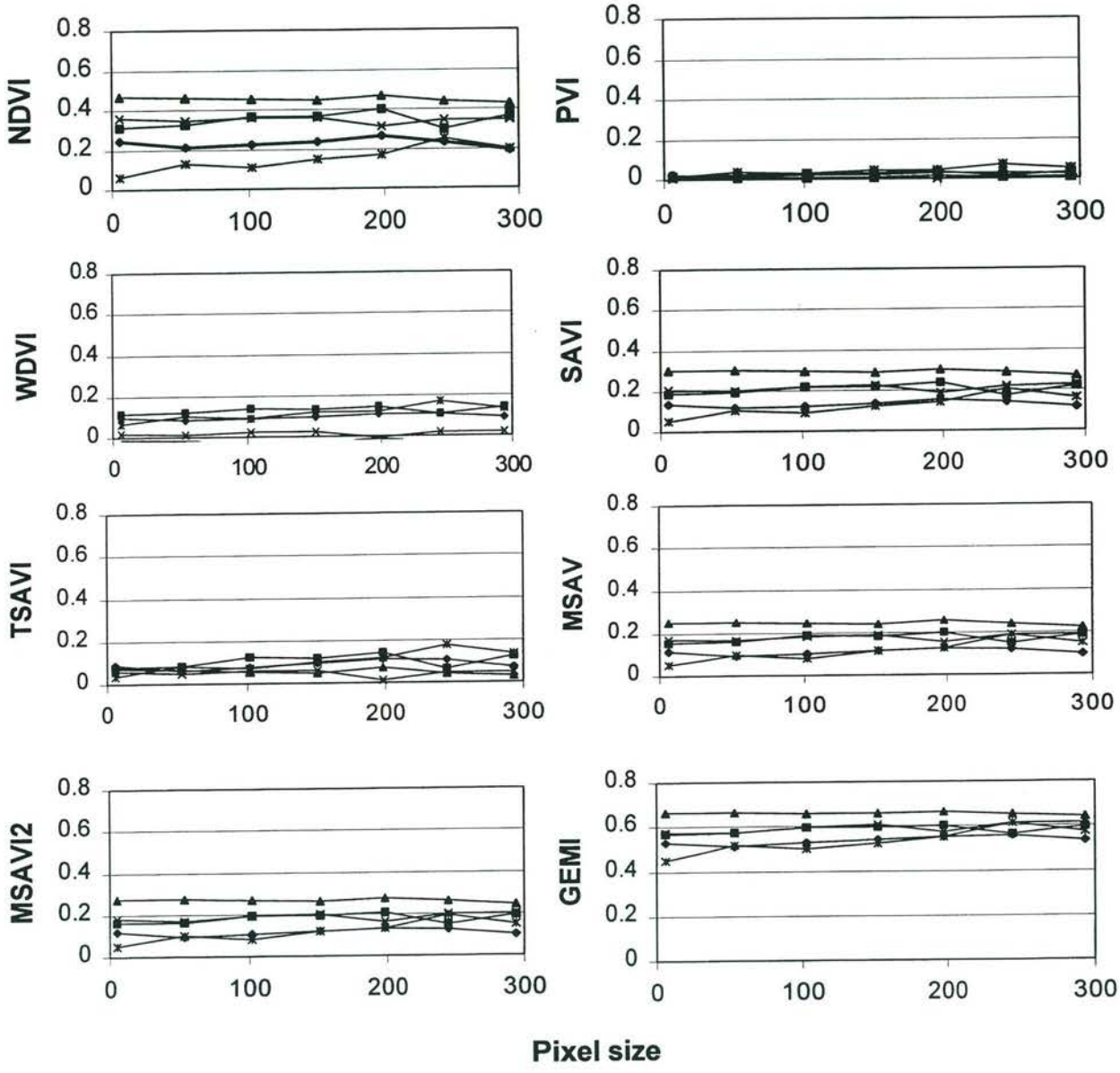

Figure 4. Vegetation indices for different target types at different spatial resolutions ranging from 6m. up to 294 m. (legend: garrigue = ◆, maquis = ■, mixed oak forest = ▲, pine forest = ×, bare agricultural field = ✳).

6.3 Vegetation index

Five regions of interest (ROI; Figure 2) were defined in the DAIS scene for selected target endmembers: garrigue, maquis, mixed oak forest, pine forest and bare agricultural field. For

each of these endmembers the vegetation index values were calculated using the following equations, respectively:

$$\text{NDVI} = \frac{NIR - red}{NIR + red}$$

$$\text{PVI} = \left[\frac{1}{\sqrt{a^2 + 1}}\right] * (NIR - a * r - b)$$

$$\text{WDVI} = NIR - a * red$$

$$\text{SAVI} = \left[\frac{NIR - red}{NIR + red + L}\right] * (1 + L)$$

$$\text{TSAVI} = \frac{a * (NIR - a * red - b)}{(b * NIR + red - b * a + X * (1 + a * a))}$$

$$\text{MSAVI} = \left[\frac{NIR - red}{NIR + red + (1 - 2 * a * NDVI * WDVI)}\right] * [1 + (1 - 2 * a * NDVI * WDVI)]$$

$$\text{MSAVI2} = \left[\frac{2NIR + 1 - \sqrt{(2NIR + 1)^2 - 8(NIR - red)}}{2}\right]$$

$$\text{GEMI} = [eta * (1 - 0.25 * eta)] - \left[\frac{red - 0.125}{1 - red}\right]$$

where NIR is the near infrared reflectance (MERIS band 12 at 775nm., DAIS band 17 at 773nm.), red is the red reflectance (MERIS band 7 at 665nm., DAIS band 11 at 671nm.), a is the slope angle between the soil line and the near infrared axis, b is the offset of the soil line, X is the x factor described earlier, L is the L factor described earlier, and *eta* is defined as

$$eta = \frac{2 * [(NIR)^2 - (red)^2] + (1.5 * NIR) + (0.5 * red)}{NIR + red + 0.5}$$

6.4 Biomass estimates

Biomass estimates were derived in the field from 120 transects of 30 meters. For shrubs, the method of Pereira *et al.* (1993) was used which applies the following formula to calculate biomass:

$$shrubs = 0.642 * (h_s)^{0.075} * (d_s)^{2.4901} * 166.67 * N_s$$

For trees we used the method of Floret *et al.* (1989) which applies the following equation:

$$trees = \frac{(-16.6845 + (0.65729(d_t)^2 * h_t))}{6} * N_t$$

where h is height in cm., d is diameter in cm. and N is the counts. To assess above ground biomass (AGB) from spectral information a spreadsheet database was created with geographic co-ordinates, cover types and AGB for trees, shrubs and their totals. All sample points were located in the DAIS and MERIS imagery and were added to the database. The database allowed statistical analysis of the spectral and biomass information, which enabled to create transfer models to assess AGB from spectral information.

6.5 Results

Comparing the different vegetation index values from the different ROIs at the different spatial resolutions (Figure 4) the following can be seen: the vegetation indices remain constant at all scales. As mixed oak forest is thought to cover the surface close to 100%, this ROI should give the highest vegetation index values. The garrigue endmember is thought to have the lowest value. Vegetation index values derived from the NDVI, SAVI, MSAVI, MSAVI2 and GEMI in some cases confirm this, however sometimes the bare agricultural field and the pine forest targets yield lower values. The GEMI, however, has much higher values than the other indices. This maybe the result from the objective of the GEMI: to correct for atmospheric interactions. Alternatively, the radiometric calibration of the
Figure 4 shows that the PVI, WDVI and TSAVI show a pattern contrary to that of the other vegetation indices. For these indices, mixed oak forest has the lowest vegetation index values and garrigue the highest. The PVI is an atmospheric sensitive index, and described above, a detailed look should be given to the accuracy of the performed radiometric calibration. The WDVI is calculated using a soil line, which might have been wrongly defined due to the scatter in the data. A sensitivity analysis would indicate whether this would explain the variation in the PVI, WDVI and TSAVI indices. The TSAVI is calculated using a soil adjustment factor (*X*). This *X*- factor used (0.08) is derived from Baret and Guyot (1991) and may not be appropriate in our specific case. The curves show some irregularities, in some cases vegetation index values increase with increasing pixel size, sometimes vegetation index values decrease. Especially around the 250 m. pixel size, the maquis and the agricultural field values become very erratic. Pine vegetation index values show a decrease at 200 m. pixel size, while the other types still have increasing values.

Figure 4 illustrates the relation between NDVI and pixel size for the five different target types: garrigue, maquis, mixed oak forest, pine forest and a bare agricultural field (i.e., an abandoned and ploughed vine yard). For four defined targets (all except for "bare agricultural field") varying spatial resolution from 6 up to 300 m. has little effect on the NDVI and the curves are almost superimposed and distinct NDVI amplitudes can be seen. This result matches well with results from similar studies (Teillet et al. 1997) on a forested region in south-eastern British Colombia. Mixed oak forest has the highest NDVI level (approximately 0.45), maquis and pine forest balance around 0.35, garrigue has values between 0.2-0.25 and the bare soil varies between 0.05 and 0.2. The NDVI for the endmember bare agricultural field tends to converge towards garrigue at larger spatial resolution due to the problem of not "seeing" a single agricultural field (spatial size: 120x180 m) at the MERIS spatial resolution of 300 m.

The relation between the MERIS' and DAIS' NDVI is important because it relates to the spatial correlation between them. In theory one expects to fit a y=x linear through the data (Figure 5), however the best fit (r=0.31) is obtained adding an offset of 0.15. The offset is thought to be the result of the averaging effect imposed by the spatial simulation algorithm.
A Pearson correlation between biomass and each spectral band reveals a modest but significant ($p<0.05$) correlation for most spectral bands from 0.32-0.44 (De Jong *et al.*, 1998). When mathematical functions are fitted through these data of NDVI and biomass, an exponential fit provides the best result. As expected each fit has the shape of an extinction function and becomes saturated at larger vegetation biomass values (Figure 6). As the

correlation between biomass and NDVI for both DAIS as well as MERIS are modest. More work is needed to better understand the scaling effects and biophysical properties at the scale of MERIS in relation to field scale.

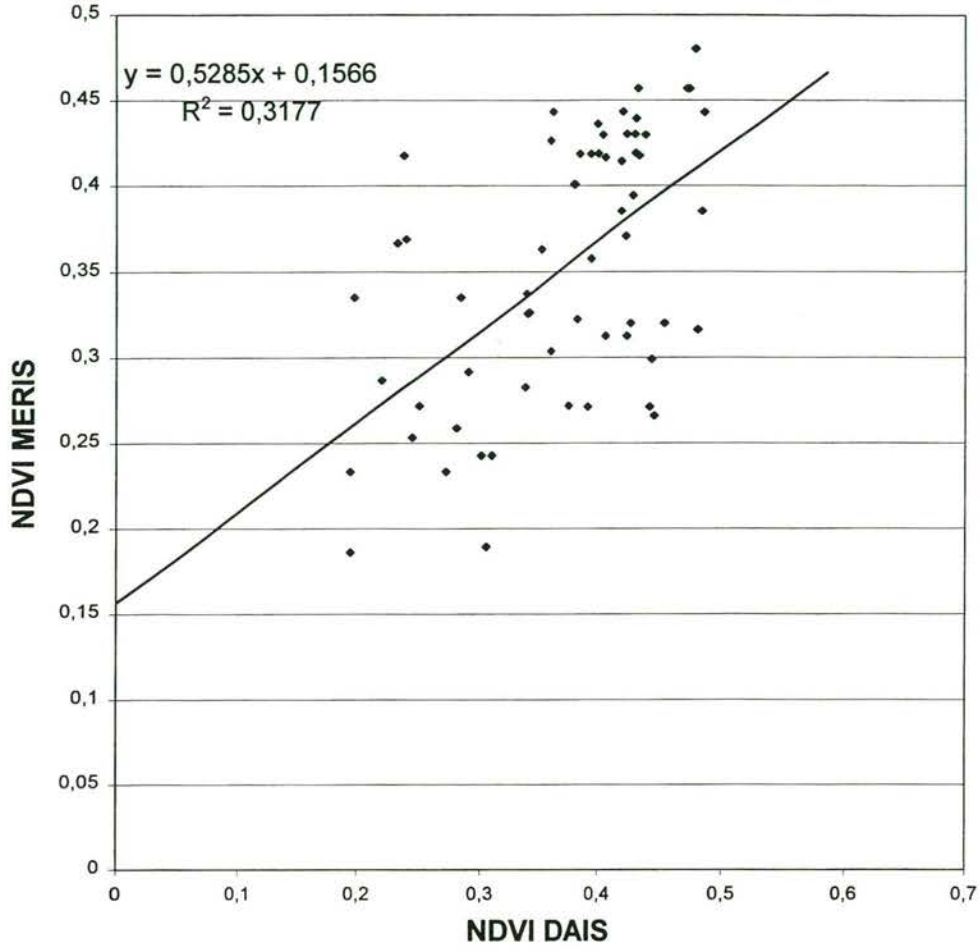

Figure 5. Relation between DAIS NDVI and MERIS NDVI with y=x plot line offset by 0.15 yielding the best possible (but statistically insignificant) fit.

6.6 Conclusions

Simulated MERIS data from airborne DAIS data have been presented as well as an approach for the convolution necessary to obtain the data sets. We have gathered biomass data in the field partly from spectral measurements and have derived standard vegetation products from the image data at variable spatial resolutions. Five regions of interest were defined for the selected target endmember: garrigue, maquis, mixed oak forest, pine forest and bare agricultural field. The vegetation indices, although the differ amongst themselves, show to be remarkable constant with the spatial scale of observation. The NDVI for the endmember bare agricultural field tends to converge towards garrigue at larger spatial resolution due to the problem of "seeing" a single agricultural field (spatial size: 120x180 m) at the MERIS spatial resolution of 300 m. The GEMI, however, has much higher NDVI values than the other vegetation indices which might be caused by the (over)correction for atmospheric influences or by the inappropriate radiometric calibration of the DAIS7915 images. The PVI, WDVI and TSAVI show a pattern contrary to the other vegetation indices where the mixed oak forest

endmember has the lowest values and the garrigue endmember the highest values. The PVI is an atmospheric sensitive index, and as is described above, a detailed look should be given to the accuracy of the performed radiometric calibration. The WDVI is calculated using a soil line and the TSAVI is calculated using a soil adjustment factor (X). Both may have been inaccurate. The best relation between MERIS' and DAIS' NDVI is obtained using a linear model with an offset of 0.15 (r=0.31).

A Pearson correlation matrix between above ground biomass measured in the field and each spectral band reveals a modest but significant ($p<0.05$) correlation for most spectral bands (De Jong et al. 1998). When mathematical functions are fitted through the NDVI and biomass data, an exponential fit gives the best fit showing the extinction and saturation at larger vegetation biomass values.

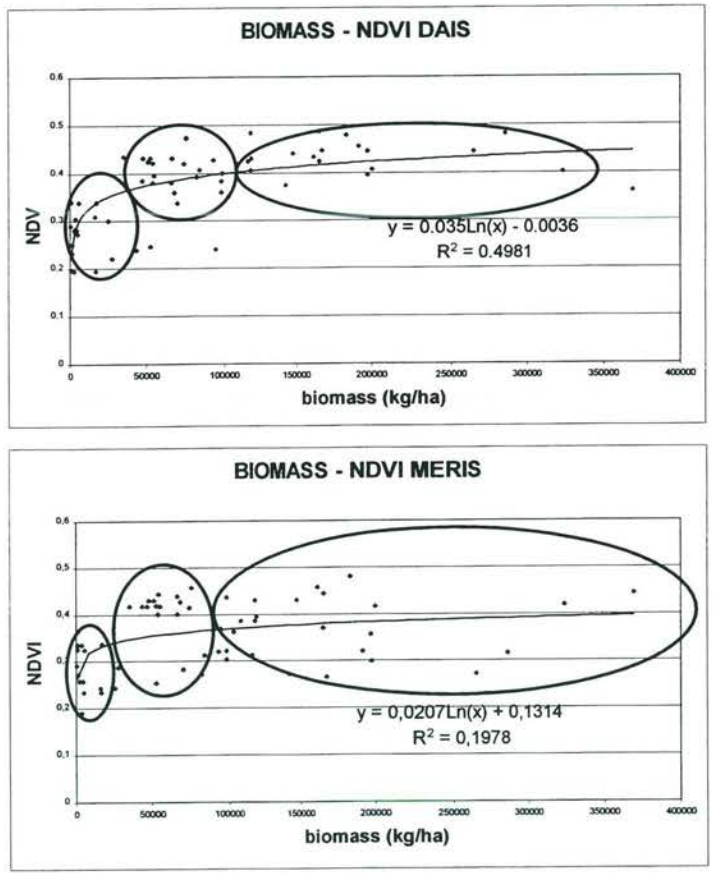

Figure 6. Biomass assessment (AGB) using the original DAIS data (top graph) and the MERIS data (bottom graph). Ellipses (from left to right) identify pixels belonging to the targets garrigue, maquis, and mixed oak forest, respectively, on both graphs.

Chapter 7

The red edge index using the MERIS standard band setting

7.1 introduction

The spectral signature of living plant material is dominated by chlorophyll, the cell structure and the water content, in the VIS, NIR and SWIR region of the electromagnetic spectrum. Imaging spectrometers measure the reflected radiation of vegetation at much detail offering new possibilities to estimate, for instance, important carbohydrates of plants (Elvidge, 1990). Too date, remote sensing of foliar chemical concentrations, other than chlorophyll and water, has not been very successful because the presence of water in living leaf tissue almost completely masks these biochemical absorption features. Recently, Clevers (1999) showed that imaging spectrometry provides additional information at the red edge region, not covered by the information provided by a combination of a NIR and a VIS broad spectral band. This author concluded that a major contribution of imaging spectrometry to applications in agriculture is to be expected.

The region of the red edge concerns the region of the sharp rise in reflectance of green vegetation between 670 and 780 nm., which can be used for studying the chlorophyll content as a measure of plant condition (Horler *et al.*, 1983). Both the position and the slope of the red edge change under stress conditions, resulting into a shift of the slope towards shorter wavelengths (e.g. Horler *et al.*, 1983; Wessman, 1994). The position of the red edge is defined as the position of the main inflexion point of the red-NIR slope often denoted as the red edge index. Reliable detection of any shift in the red edge position requires sampling of the red edge region at about 10 nm. intervals or less, requiring high-resolution spectral measurement in at least four spectral bands between 660 and 780 nm.

Clevers (1994) showed that the leaf area index (LAI) and the leaf chlorophyll content are the main parameters determining the value of the red edge index. The LAI may be estimated from broad-band vegetation indices. Subsequently, the red edge index can be used for estimating the chlorophyll content Clevers *et al.* (1994).

The MERIS resolution of 300 m. over land should be sufficient to monitor the highly heterogeneous terrestrial surfaces at scales required for global change studies (ESA, 1995; Verstraete *et al.*, 1999). Vegetation indices using red and NIR reflectance can be used for estimating the LAI and the fraction of absorbed photosynthetically active radiation (Govaerts *et al.*, 1999). The red edge feature may provide useful information on the physiological status of the vegetation under observation. Verstraete *et al.* (1999) noted that the spectral and spatial resolution of MERIS will be appropriate to derive this red edge index, however, these authors state that much remains to be done in this respect to design algorithms based on MERIS data.

Here we study the red edge index derived from MERIS data using the standard band setting. Thus, the standard band setting provides the bands that are most suitable for monitoring purposes. No attention is paid to the interpretation and application of a red edge index at the spatial scale at which MERIS operates.

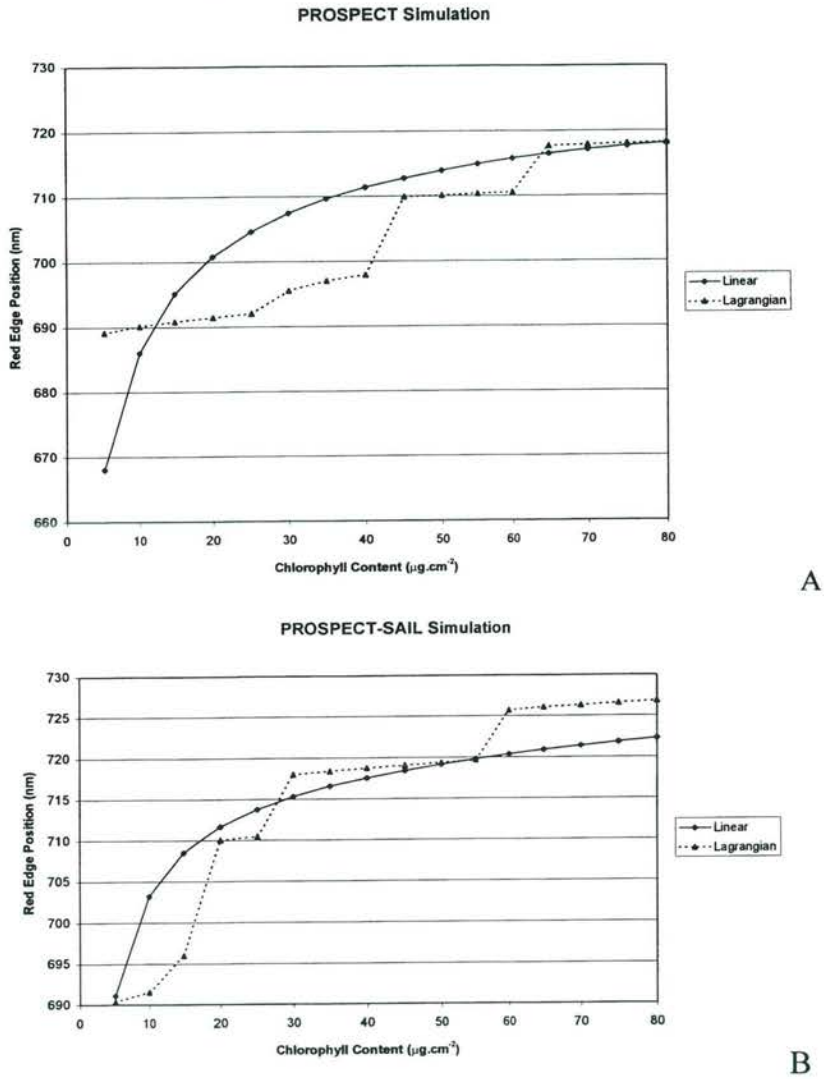

Figure 1. Red edge position as a function of the leaf chlorophyll content for the linear method and for the Lagrangian technique at the leaf level (a) and at the canopy level with an LAI of 2.0 (b) as simulated with a combined PROSPECT-SAIL model.

7.2 Methodology for determining the red edge index

Since the position of the red edge is defined as the inflexion point (or maximum slope) of the red infrared slope, an accurate determination requires a number of spectral measurements in small bands in this region. The red edge position is defined by the maximum first derivative of the reflectance spectrum in the region of the red edge. High-order curve fitting techniques are generally employed to fit a continuous function to the derivative spectrum (Horler *et al.*, 1983; Demetriades-Shah & Steven 1988; Demetriades-Shah *et al.*, 1990). Existing curve fitting techniques, however, are complex and computationally demanding. Recently, Dawson & Curran (1998) presented a technique based upon a three-point Lagrangian interpolation technique for locating the red edge position accurately in coarsely sampled spectra. A

problem may arise when the reflectance spectrum exhibits more than one maximum in its first derivative. Horler *et al.* (1983) identified two components in the first derivative spectrum with peaks around 700 and 725 nm. The red edge index then represented whichever component was dominant, and therefore a red edge shift could involve a jump between the two components, creating a discontinuity in the red edge index. They found that the second component moves to longer wavelengths and becomes more pronounced as the LAI increases.

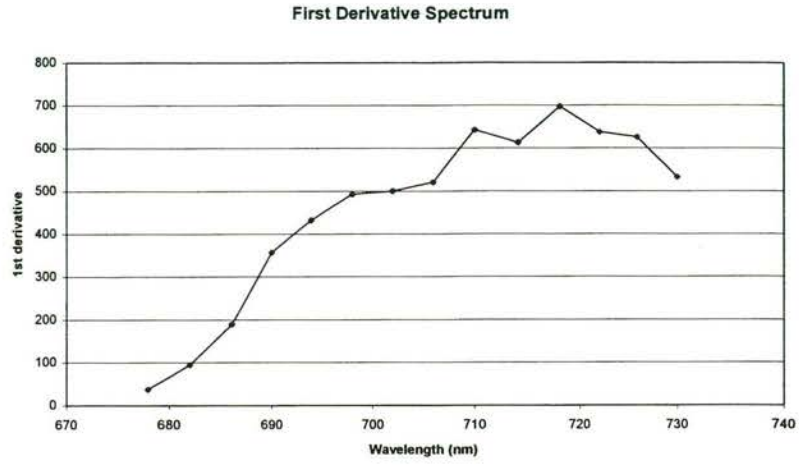

Figure 2. Example of a simulated first derivative spectrum as simulated with a combined PROSPECT-SAIL model.

For practical reasons, fitting a curve to just a few measurements in the red edge region is often applied for approximating the inflexion point. First, a polynomial function may be fitted to the data (Clevers & Büker 1991). Secondly, a so-called inverted Gaussian fit to the red infrared slope may be applied (Bonham-Carter, 1988). Finally, a simple linear model is applied to the red infrared slope (Guyot & Baret, 1988). A comparison of the three methods described above yielded comparable results (Clevers & Büker 1991; Büker & Clevers, 1992). Since the method of Guyot & Baret (1988) uses only four wavelength bands, this method is applicable to a wide range of future sensors. Therefore we chose to use the latter method for this study and to compare it with the Lagrangian technique described by Dawson & Curran (1998).

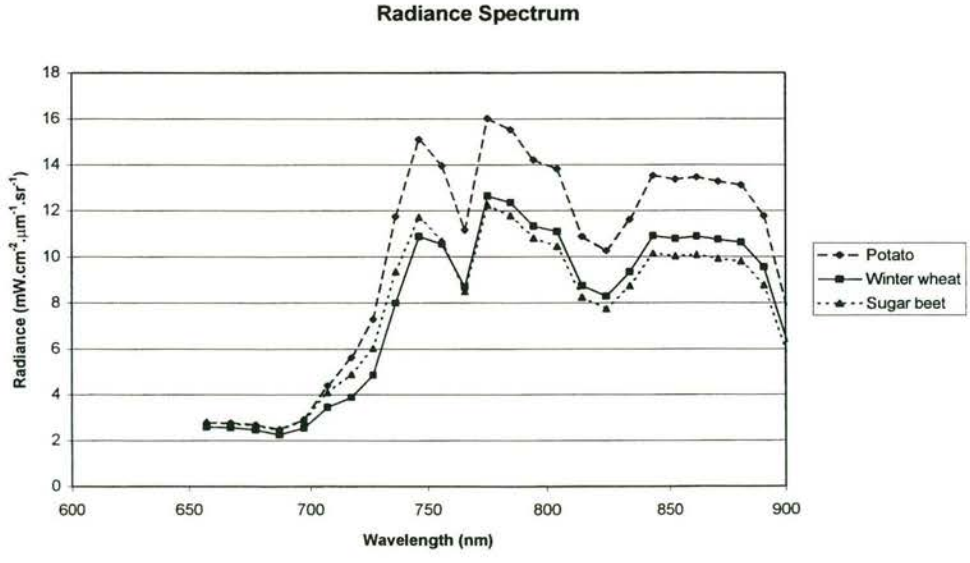

Figure 3. Spectral signature in radiance ($mW.cm^{-2}.\mu m^{-1}.sr^{-1}$) for the three major crops at the Flevoland test area, measured with the AVIRIS sensor on July 5th, 1991.

The linear interpolation as described by Guyot & Baret (1988) assumes that the reflectance curve at the red edge can be simplified to a straight line centred near a midpoint between the reflectance in the NIR near 780 nm. and a reflectance minimum of the chlorophyll absorption feature near 670 nm. First, Guyot & Baret (1988) estimated the reflectance value at the inflexion point. Secondly, these authors applied a linear interpolation procedure between the measurements at 700 and 740 nm. for estimating the wavelength corresponding to the estimated reflectance value at the inflexion point. This method, which will be called the "linear method" is described in the following way:

Calculation of the reflectance at the inflexion point (R_{re}):

$$R_{re} = (R_{670} + R_{780})/2$$

Calculation of the red edge wavelength (λ_{re}):

$$\lambda_{re} = 700 + 40 * ((R_{re} - R_{700})/(R_{740} - R_{700}))$$

where R_{670}, R_{700}, R_{740} and R_{780} are the reflectance values at 670, 700, 740 and 780 nm.wavelength, respectively.

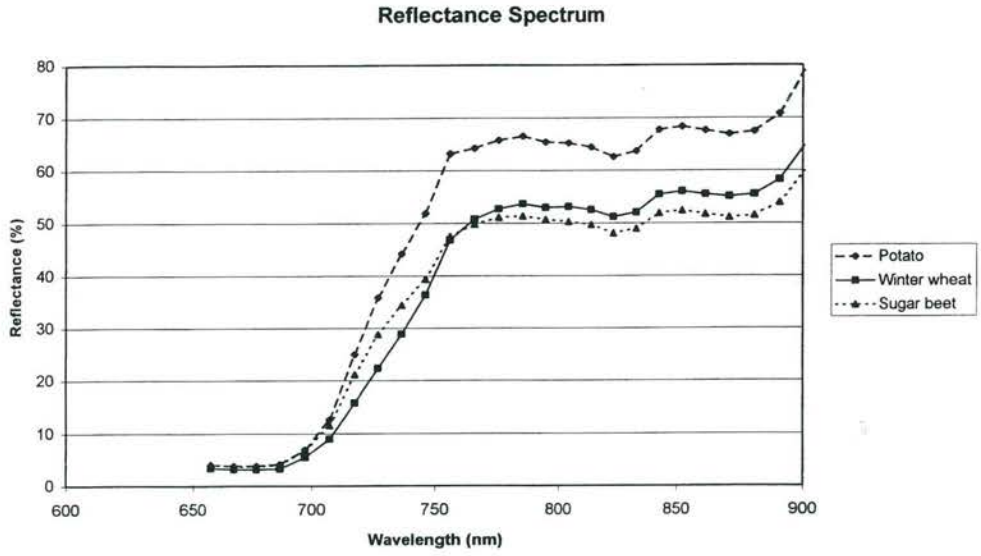

Figure 4. Spectral signature in terms of reflectance for the three major crops at the Flevoland test area, measured with the AVIRIS sensor on July 5th, 1991.

7.3 Data sets

Two different data sets will be used for this study. Simulated data with a combination of the PROSPECT leaf reflectance model and the SAIL canopy reflectance model (data set I) and airborne reflectance spectra of agricultural crops obtained from AVIRIS data. Jacquemoud & Baret (1990) developed a leaf model that simulates leaf reflectance and leaf transmittance as a function of leaf properties: the PROSPECT model (data set II). The PROSPECT model is a radiative transfer (RT) model for individual leaves based on the generalised "plate model" of Allen *et al.* (1969, 1970). This model considers a compact theoretical plant leaf (without air cavities) as a transparent plate with rough plane parallel surfaces. A leaf is composed of a pile of N homogeneous compact layers separated by N-1 air spaces. The compact leaf (N = 1) has no intercellular air spaces or the intercellular air spaces of the mesophyll have been infiltrated with water. The discrete approach can be extended to a continuous approach where N needs not be an integer. PROSPECT allows computing the 400-2500 nm. reflectance and transmittance spectra of very different leaves using only three input variables: the leaf mesophyll structure parameter N, the pigment content and the water content. All three

parameters are independent of the selected wavelength. The output of the PROSPECT model can be used directly as input into the SAIL model. As a result, these models can be combined into one common model.

The one-layer SAIL radiative transfer model (Verhoef, 1984) simulates canopy reflectance as a function of canopy parameters (leaf reflectance and transmittance, LAI and leaf angle distribution), soil reflectance, and ratio diffuse/direct irradiation. The sensor geometry parameters used are solar/view geometry, i.e., solar zenith angle, zenith view angle and sun-view azimuth angle. Bunnik (1978) and Verhoef & Bunnik (1981) give leaf inclination distribution functions used with the SAIL model. The SAIL model has been used in many studies and validated with various data sets (e.g., Goel, 1989).

The ER-2 aircraft of NASA, carrying the airborne visible-infrared imaging spectrometer (AVIRIS), performed a successful flight over the Flevoland test site on July 5th, 1991 (being the middle of the growing season). AVIRIS acquires 224 contiguous spectral bands from 410 to 2450 nm. The spectral resolution and the spectral sampling interval of the sensor are approximately 10 nm. Due to sensor malfunction, spectral information was only available in the 400 nm. to 1860 nm. The ground resolution was 20 m. at a flying height of 20 km. altitude.

Pre-processing of the AVIRIS data included correction for dark current, vignetting and radiometric response and was conducted by the Jet Propulsion Laboratory (JPL). Atmospheric correction was done at JPL using the LOWTRAN 7 atmospheric model, thus yielding surface reflectances (Van Den Bosch & Alley, 1990). The AVIRIS data set was available in radiance as well as in reflectance. Both are used in this study.

The test site was located in Southern Flevoland in the Netherlands, an agricultural area with homogeneous soils reclaimed from the lake IJsselmeer in 1966. The test site comprised ten different agricultural farms, each 45 to 60 ha in size. Main crops were sugar beet, potato and winter wheat. Crop parameters concerning acreage, variety, planting date, emergence date, fertilisation, harvest date, yield and occurring anomalies were collected for the main crops. During the growing season, additional parameters such as soil cover, crop height, development stage and spectral reflectance were measured in the field approximately every ten days.

7.4 Results and discussion

7.4.1 Comparison of the linear method with the Lagrangian technique

First, the simple linear method based on four spectral bands is compared with the three-point Lagrangian technique. Data set I yielded simulated reflectances at the leaf level using the PROSPECT model and at the canopy level using a combined PROSPECT-SAIL model at wavelengths with 4 nm. intervals. The standard simulation (as defined by Clevers & Verhoef, 1993; see also Jacquemoud & Baret, 1990) was applied using a leaf chlorophyll content of 34.24 $\mu g.cm^{-2}$, an N-parameter of 1.832 and a water content of 0.0137 cm. For the canopy, we used a LAI of 2.0, a spherical leaf angle distribution, a soil reflectance of 20%, assuming direct solar irradiation, a solar zenith angle of 45° and nadir viewing. Figure 1 shows the red edge position as a function of the leaf chlorophyll content for the linear method and for the Lagrangian technique at the leaf level (Figure 1a) and at the canopy level (Figure 1b).

These results show a good correspondence between the two methods, particularly at the canopy level. The 'jumps' of the curve for the Lagrangian technique are apparent. These are caused by the fact that the first derivative spectrum has more than one peak. With changing chlorophyll content, different peaks become dominant, causing a discontinuity in the relationship. Similar features appear when plotting the red edge position as a function of LAI. An example of a simulated first derivative spectrum is given in Figure 2.

Data set II comprises imaging spectrometer measurements over an agricultural area. Figure 3 illustrates the radiance spectrum in the red edge region for the three main crops in the area. For the linear method the following AVIRIS spectral bands were used: 667.4 – 697.3 – 736.7 – 785.0 nm. Clevers (1992) showed that the red edge position estimated from these radiance values was similar to the one obtained from spectral reflectance measurements performed in the field using a hand-held radiometer. Notable in Figure 3, a dip in the radiance curve at about 760 nm. can be observed: the well-known absorption feature caused by oxygen in the atmosphere. Also an absorption feature at about 820 nm., caused by water vapour in the atmosphere, is obvious. When including the AVIRIS band at 756.0 nm, and possibly the one at 746.4 nm, in the Lagrangian interpolation technique biased results can be expected when no atmospheric correction is performed. This was confirmed by our results: some crops yielded a red edge position around 734.0 nm. and others around 735.5 nm., while the linear method and field measurements yielded a range roughly between 722 and 735 nm.

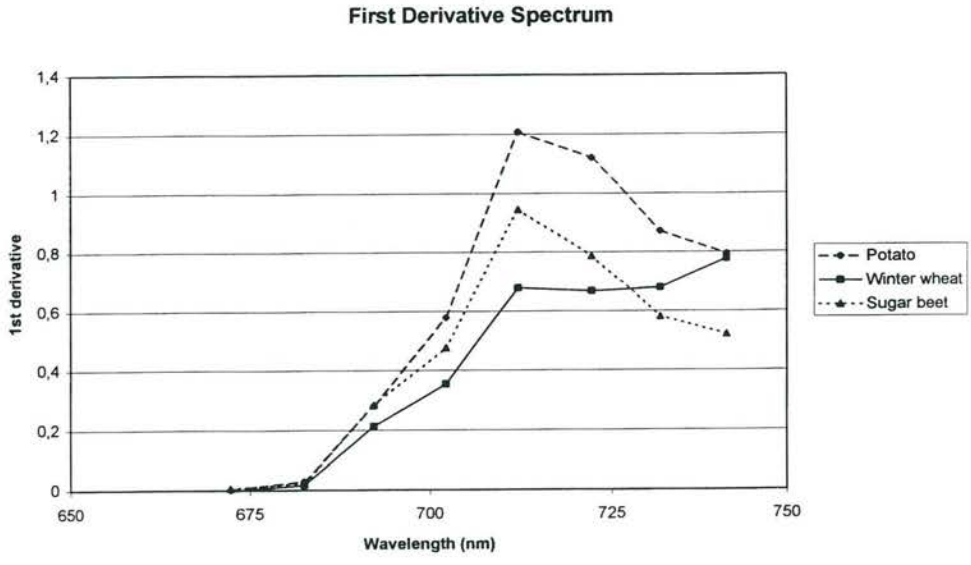

Figure 5. First derivative spectra based on reflectance for the three major crops at the Flevoland test area, measured with the AVIRIS sensor on July 5th, 1991.

Figure 4 illustrates the spectral signature in terms of reflectance for the main three crops in the area after atmospheric correction thus removing the oxygen absorption feature. As a result, the Lagrangian technique should yield more reliable results. When looking at the first derivative spectrum again no unique maximum is observed for some crops within the 700 – 740 nm. range of the red edge region (figure 5). In some cases (e.g., for winter wheat) the maximum slope lies beyond 740 nm. In order to cope with this problem the red edge position was taken as the position of the first (relative) maximum. Figure 6 plots then the red edge position calculated using the Lagrangian technique against the red edge position obtained using the linear method. Although the range in obtained red edge positions for the Lagrangian technique is broader than when calculations were performed on radiance values, the range is still very narrow and values are low (around 715 nm.) when compared with the results of the linear method and with field measurements.

In conclusion we can state that both data sets show that the first derivative spectrum does not have one unique maximum, rendering procedures based on the first derivative spectrum thus are not very suitable for defining the red edge position. The linear method based on four fixed spectral bands is a more robust method.

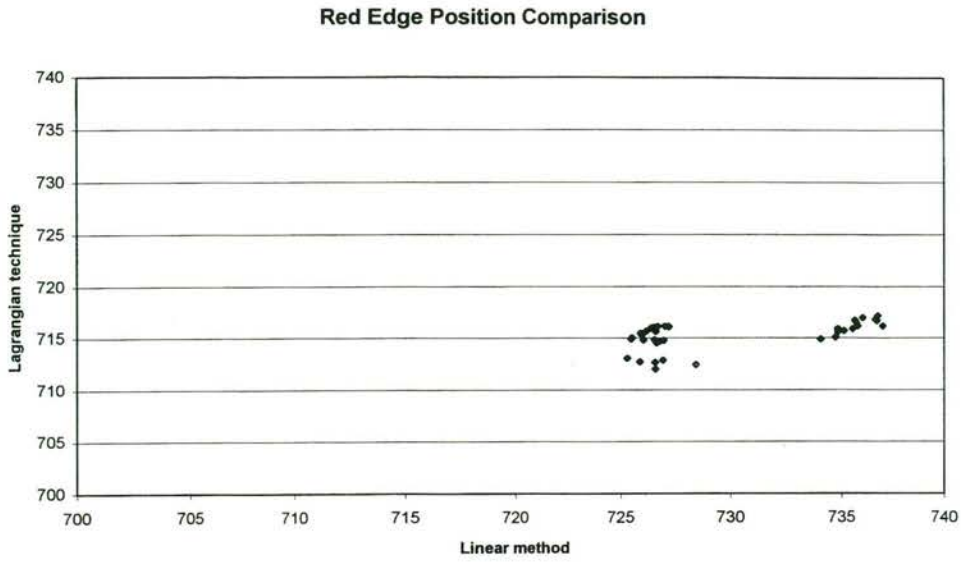

Figure 6. Comparison of the red edge position calculated using the linear method and the one obtained with the Lagrangian technique, Flevoland test area, AVIRIS recording, July 5th, 1991 for all three crops: potato, winter wheat and sugar beet.

7.4.2 Red edge index simulation with MERIS

In the previous subsection the linear method proved to be a robust method for determining the red edge position of vegetation canopies. With the simulated data, a linear interpolation is performed between the wavelengths 700 and 740 nm. With the AVIRIS data set the spectral bands centred at 697.3 and 736.7 nm. were used.

MERIS has also a spectral band in the chlorophyll absorption feature at 665 nm.and at the NIR plateau at 775 nm. These are close to the wavelengths used in the linear method as described by Guyot and Baret (1988). These two channels can be used for estimating the reflectance value at the inflexion point. The next step in the linear method is that this reflectance value at the inflexion point is translated to the corresponding wavelength by a linear interpolation between the reflectances measured at two wavelength positions on the red edge slope. From the MERIS standard band setting the spectral bands centred at 705 and 753.75 nm. are available. In this section it will be tested whether these bands yield useful estimates of the red edge position.

Figure 7 illustrates the red edge position as a function of the leaf chlorophyll content for the linear method using the interpolation between 700 and 740 nm.and for the linear method using the MERIS band setting and interpolating between 705 and 754 nm. for data set I. Both curves exhibit a similar pattern, whereby the MERIS-based linear method shows larger red edge index values, except for index values below 705 nm. For the latter range, considerable deviations between the two methods occur, which primarily can be attributed to the fact that using the MERIS bands we are performing an extrapolation instead of an interpolation. The relationship between the two methods is depicted in Figure 8, showing a linear relationship in this case albeit that it not matches the 1:1 line. In this Figure the relationship is simulated for a canopy with small steps in chlorophyll content and for canopies with various LAI values.

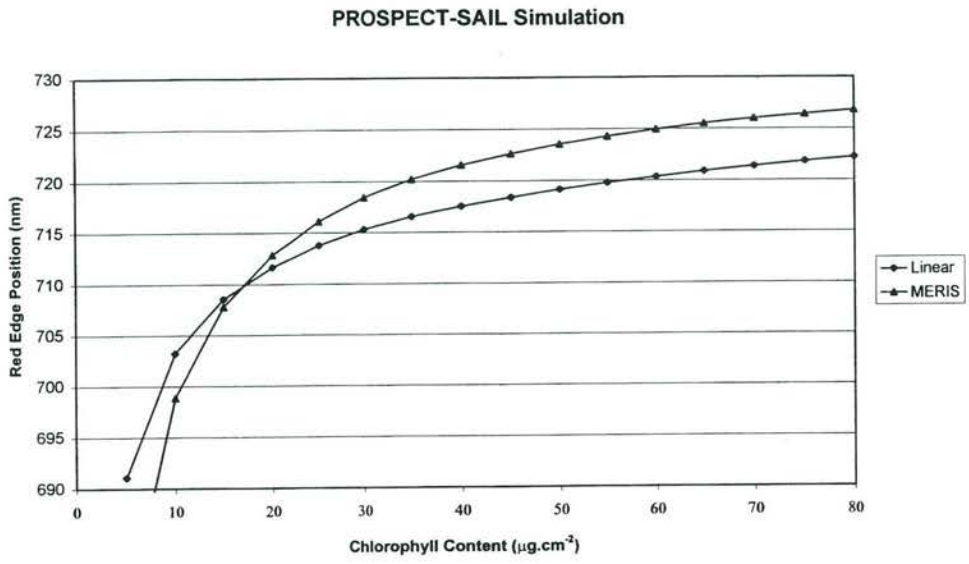

Figure 7. Red edge position as a function of the leaf chlorophyll content for the linear method using the 700 and 740 spectral bands and for the linear method using the MERIS band setting for a canopy with an LAI of 2.0 as simulated with a combined PROSPECT-SAIL model.

This results show that general relationships may be derived from the two methods and that a linear relationship yields a good fit to the data. Using all the data of Figure 8, the regression line yields:

$re_{MERIS} = -409.0 + 1.574 * re_{700\text{-}740}$

$r = 0.996$.

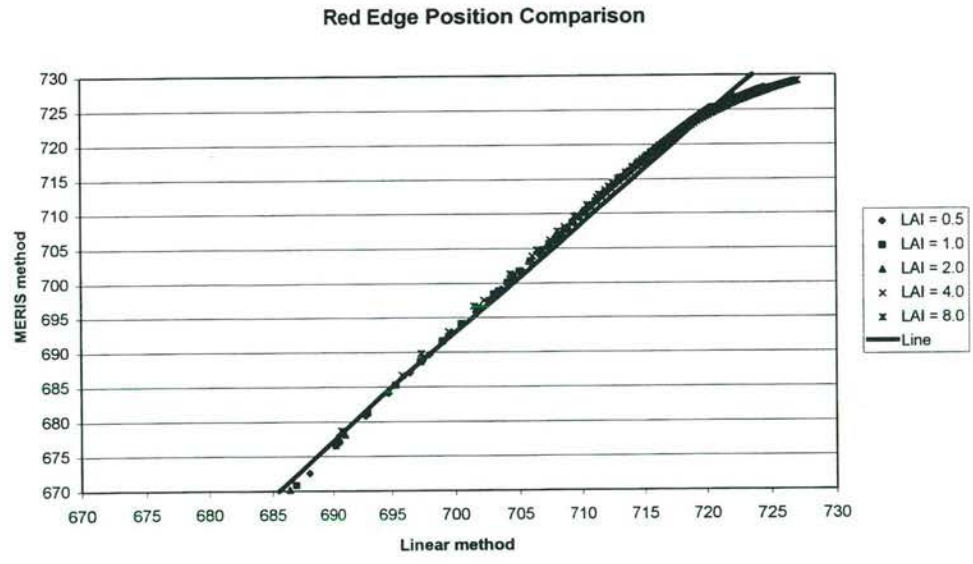

Figure 8. Comparison of the red edge position calculated using the linear method interpolating between 700 and 740 nm. and the linear method using the MERIS spectral bands, thus interpolating between 705 and 754 nm., PROSPECT-SAIL simulation for a canopy with varying leaf chlorophyll content and various LAI values.
The regression line $re_{MERIS} = -409.0 + 1.574 * re_{700\text{-}740}$ is also plotted.

Using data set II, MERIS' spectral bands using the AVIRIS data were created. The bands at 667 and 775 nm. were used for estimating the reflectance at the inflexion point and the bands at 707 nm. and the average of 746 nm. and 756 nm. were used for the linear interpolation.

Figure 9 illustrates the relationship between the red edge position calculated from the interpolation between 697 and 737 nm. and that calculated using the simulated MERIS bands for the main agricultural crops at the Flevoland test site. When we compare this relationship with the regression line found for data set I, a good match is found, however larger deviations occur at high red edge values.

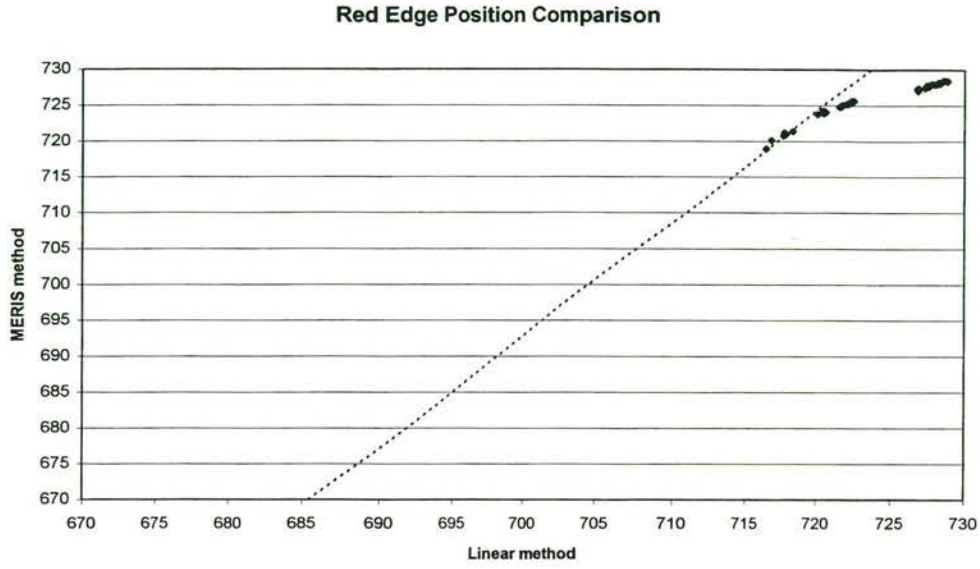

Figure 9. Comparison of the red edge position calculated using the linear method interpolating between 697 and 737 nm.and the linear method using the MERIS spectral bands for the main crops at the Flevoland site, measured with the AVIRIS sensor on July 5th, 1991. The regression line from figure 8 is also plotted.

7.4.3 Upscaling to the MERIS resolution

In section 7.4.2 the red edge index was calculated for the simulated MERIS bands using AVIRIS data at 20 m spatial resolution (Figure 10, cf. Figure 9). A colour composite for the Flevoland test area is depicted Figure 11 (color plate 8). MERIS pixels of 300 m spatial resolution were simulated by taking the average reflectance of 15 x 15 pixels for all AVIRIS spectral bands. The resulting colour composite is also depicted in Figure 11. This image shows that we cannot recognize the individual agricultural fields anymore. However, when there are fields with high biomass (red color in the image) close to each other, we recognize an area with high biomass (red MERIS pixel) in the spatially degraded image. The same is true, for instance, for areas with low or no vegetation cover (the bluish colours).

Figure 10 illustrates the relationship between the red edge position calculated from the interpolation between 697 and 737 nm and that calculated using the simulated MERIS bands for a number of degraded pixels at the Flevoland test site (cf. previous section). When we compare this relationship with the relationship found at 20 m spatial resolution, we see that the data coincide very well and that the relationships match.

From this we may conclude that the red edge index derived for the MERIS spectral bands at the MERIS spatial resolution of 300 m still provides useful information. If the objects at the earth surface are large enough, we may obtain a significant range in red edge values. At the Flevoland agricultural test site individual fields could not be recognized, but MERIS will provide informative red edge values on large units (groups of fields).

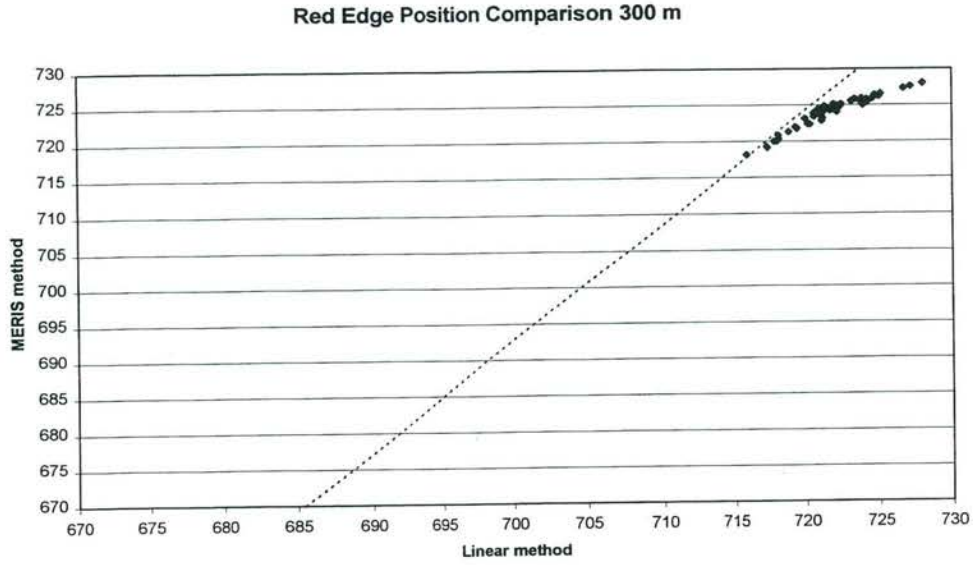

Figure 10. Comparison of the red edge position calculated using the linear method interpolating between 697 and 737 nm and the linear method using the MERIS spectral bands for AVIRIS pixels degraded to 300 m at the Flevoland site. The regression line from figure 8 is also plotted.

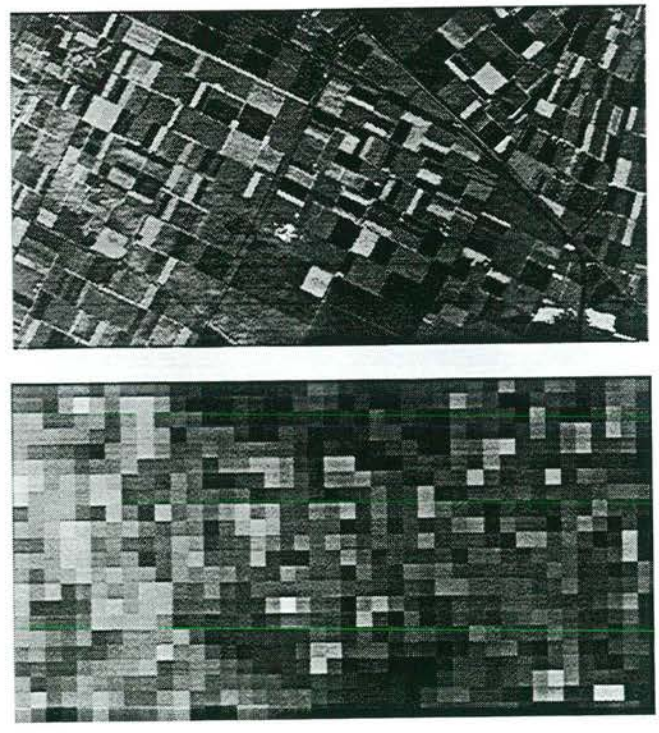

Figure 11. Top: Colour composite of AVIRIS spectral bands 44 (786 nm), 28 (667 nm) and 16 (549 nm) in RGB for the Flevoland test site, July 5th, 1991. Bottom: Colour composite of AVIRIS spectral bands 44, 28 and 16 in RGB, resampled to 300 m, for the Flevoland test site, July 5th, 1991 (color plate 8).

7.5 Conclusions

Both data sets exhibit more than one unique maximum in the first derivative reflectance spectrum, whereby different maximal values become dominant with changing LAI and with changing leaf chlorophyll content. These two variables are the main variables determining the position of the red edge. As a result, the maximum second derivative is not useful as a measure for the red edge index.

The linear method (Guyot & Baret, 1988) assumes a straight slope of the reflectance spectrum around the midpoint between the reflectance at the NIR plateau and the reflectance minimum at the chlorophyll absorption feature in the red. This midpoint is defined as the red edge index, however this point may not coincide with the maximum of the first derivative, but it appears to be a very robust definition and it needs only a very limited number of spectral bands. Thus, this method is very useful for practical applications.

Although the spectral bands of the MERIS standard band setting at the red edge slope are not optimally located, they can be used for applying the linear method for red edge index estimation. The bands to be used are located at 705 and 753.75 nm. However, since the latter band is located close to the atmospheric oxygen absorption feature, an atmospheric correction must be applied previous to calculating the position of the red edge using the MERIS bands. Previous studies (e.g., Clevers, 1994) have shown that for bands located at about 700 and 740 nm., an atmospheric correction is not necessary since the red edge calculated from reflectance data equals the one calculated from radiance data.

Results in this study have show a nearly linear relationship exists between the linear method using either bands at about 700 and 740 nm. and the MERIS bands, albeit that it not coincides with the 1:1 line. This implies instrument-specific red edge indices should be advocated. For MERIS, the above-mentioned linear relationship may be used for translating red edge index values obtained with one method (using the MERIS bands) into values obtained with the other method (based on bands at 700 and 740 nm.). Deviations occur at high red edge index values matching vegetation with a high chlorophyll content and with high LAI values. To cope with this, a non-linear function might be fitted. Another possibility is to fit a second linear relationship for the upper part of the curve. The breakpoint then seems to be located at about 720 nm. for the standard linear method (coinciding with about 725 nm. for the MERIS method). When fitting a linear function for this upper part of the curve (for the simulated data of set I), the regression line yields:

$re_{MERIS} = -243.7 + 0.668 * re_{700\text{-}740}$

$r = 0.980$.

For the remaining part of the curve the relationship given in the previous section can be used. The two regression lines are illustrated in Figure 12 for data set I. When plotting these two regression lines with the results of data set II (Figure 13) reasonable results are found, although the MERIS method underestimates the highest red edge values in comparison to the regression line. Moreover it appears that the determination of the red edge index using the MERIS band setting is less sensitive to variations in chlorophyll content and LAI than the standard linear method using interpolation between 700 and 740 nm.

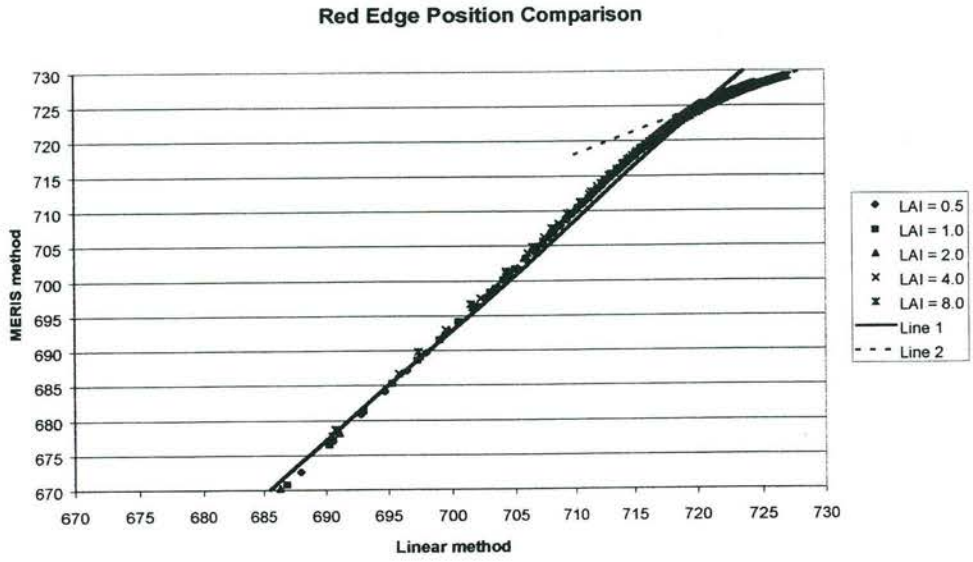

Figure 12. Comparison of the red edge position calculated using the linear method interpolating between 700 and 740 nm.and the linear method using the MERIS spectral bands, thus interpolating between 705 and 754 nm, PROSPECT-SAIL simulation for a canopy with varying leaf chlorophyll content and various LAI values.

The two regression are also plotted: Line 1: $re_{MERIS} = -409.0 + 1.574 * re_{700-740}$

Line 2: $re_{MERIS} = -243.7 + 0.668 * re_{700-740}$

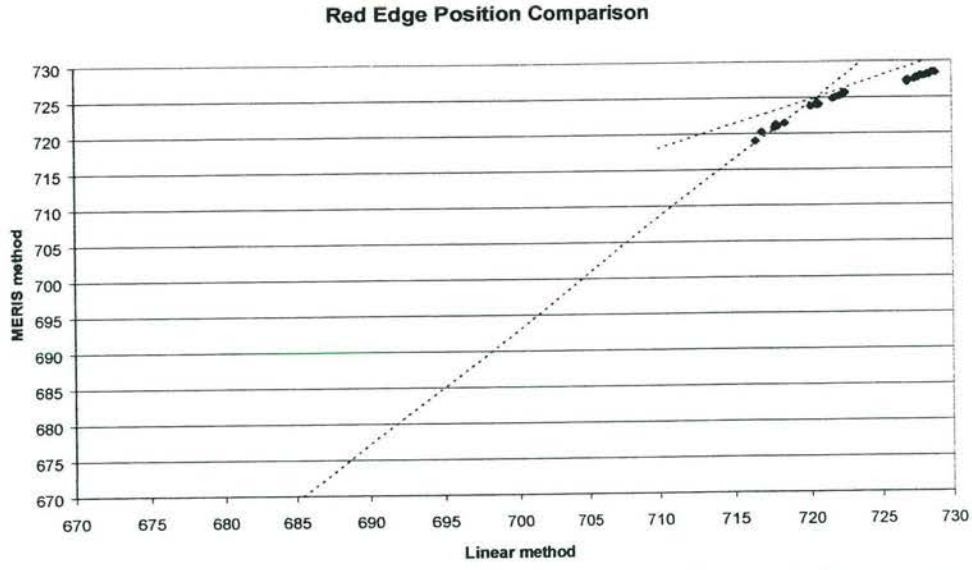

Figure 13. Comparison of the red edge position calculated using the linear method interpolating between 697 and 737 nm.and the linear method using the MERIS spectral bands for the main crops at the Flevoland site, measured with the AVIRIS sensor on July 5th, 1991. The regression lines from figure 12 are also plotted.

This study has shown that the MERIS standard band setting can be used for deriving red edge index values. No attention has been paid to the physical interpretation of red edge index values at the scale level of MERIS. The spatial resolution of MERIS is 300 m., so one hardly will observe single fields or objects of just one vegetation type. MERIS' application concerns more the application at, for instance, the ecosystem level. Highest sensitivity to variations in vegetation variables, such as chlorophyll content and LAI, occurs at the lower values of these variables. One may expect these ranges in variables more at the ecosystem level, particularly when looking at natural ecosystems.

Chapter 8

Scaling to the MERIS resolution: mapping accuracy and spatial variability

8.1 Introduction

The use of spatial statistics embedded in regionalized variables theory for the analysis of remotely sensed data dates back to the pioneering work of P.J. Curran and C.E. Woodcock in the late 1980's. Contemporaneously these authors explored the use of the semivariogram, i.e., a curve showing variance versus sample spacing, to describe patterns in remotely sensed imagery (Woodcock *et al.* 1988a+b; Curran 1988). Since that time, many new applications of geostatistics to aid in image interpretation and enhancement have been developed including: replacement of missing or bad data values (Atkinson *et al.* 1990; Rossi *et al.* 1994), estimating signal to noise (Curran & Dungan 1989), noise removal (Green *et al.* 1988), estimating measurement error (Atkinson 1997), mapping (Dungan *et al.* 1994), classification (Van der Meer 1994) and the use of co-kriging to combine field and image data (Atkinson *et al.* 1994; Van der Meer 1998). A recent summary of results can be found in Stein *et al.* (1998). With the advent of new spaceborne sensors with variable and selectable spatial and spectral resolution the factor of scale and selection of optimal support size in remote sensing becomes a pressing issue. Research in this field dates back to 1987 (Woodcock & Strahler 1987) and has recently been revived (Atkinson & Curran 1995). Related to this, issues of up- and downscaling are common problems combining geostatistical practice and remote sensing (see Stewart *et al.* 1998 for a recent review.

Since the optimal scale of measuring related variables may be dependent on the type and nature of the parameter of study, it is important to evaluate MERIS' potential relative to the scale of observation. In this chapter we present simulated MERIS data derived from airborne imaging spectrometer data sets and derive products useful for land applications at various spatial resolutions. These products are used to assess the mapping accuracy of the variable and indicate the relative optimal spatial resolution to be achieved. This leads to a better understanding of the expected performance of the sensor for different land applications. The work presented in this Chapter should be perceived as a first attempt to a better understanding of the scale of observation on the accuracy of the estimation. More work is needed on this and related issues of scale.

8.2 MERIS image products

As a preliminary analysis of scale effects in MERIS data simulation we used atmospherically corrected GERIS 63 channel imaging spectrometer data from the Almaden study site (see Figure 1 for location) in Central Spain acquired during the EISAC '89 campaign and generated a 15 band MERIS sample data set at various spatial resolutions between the original 12m. resolution and the 300m. MERIS resolution. The Almaden study site is an agricultural test site with typical large scale patches of farm land which was mostly bare during time of acquisition. The area is underlain by two granitic intrusions of leucocratic type. Details on the area and image pre-processing can be found in Fan *et al.* (1997). From the atmospherically corrected GERIS data the channels matching the MERIS bands were extracted. This resulted in a MERIS data cube at the original 12 m. GERIS resolution. This cube was subsequently re-sampled stepwise from 12 m. up to approximately 300 m. following the degradation process described in an earlier Chapter. In order to derive ground abundances of various Earth materials we applied spectral unmixing to the data cube.

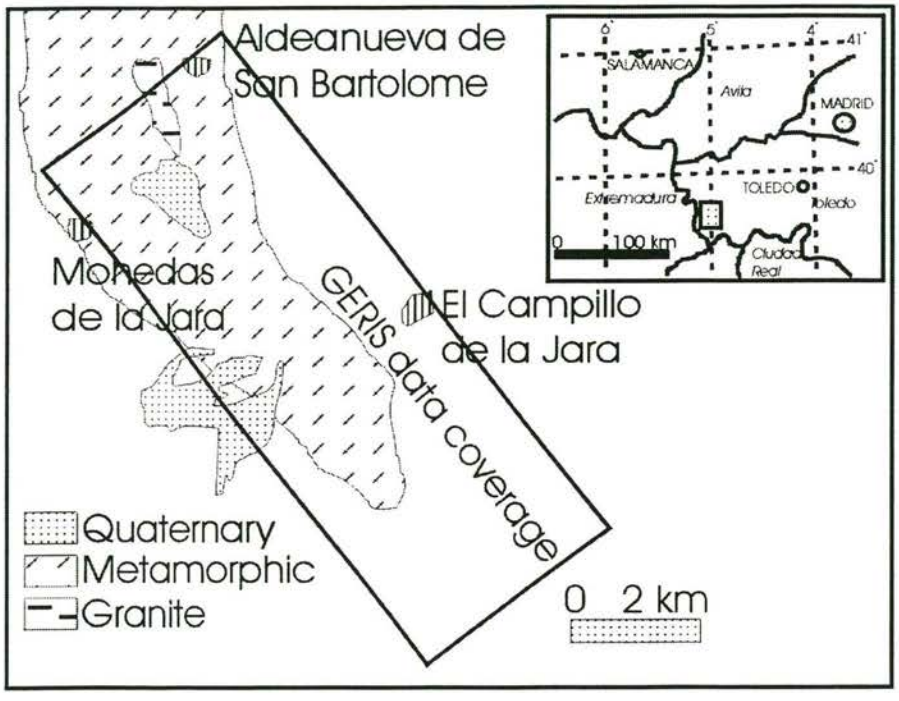

Figure 1. Location of the study area and GERIS data take (box).

We used the 12m. resolution "MERIS" data set to find the purest endmember pixels. We used the Minimum Noise Fraction (MNF) transformation of Green *et al.* (1988) to determine the spectral dimensionality defining the number of end members needed to optimally describe the spectral variability. The MNF transformation is a two-step principal component transformation where during the first step using the noise covariance matrix the noise is decorrelated to have unit variance and no band-to-band correlation. The second principal component transformation results in a data set where components are ranked in terms of noise equivalent radiance. Consider stochastic variables with expectation $E\{\mathbf{Z}\} = 0$ and dispersion $\mathbf{D}\{\mathbf{Z}\} = \Sigma$. New mutually orthogonal variables with maximum signal-to-noise ratio can be constructed as

$$Y_i = a_{i1}Z_1 + \ldots a_{ip}Z_p = a_i^T, i = 1, \ldots, p$$

Assuming additive noise (i.e., $\mathbf{Z}(\mathbf{x}) = \mathbf{S}(\mathbf{x}) + \mathbf{N}(\mathbf{x})$ where **S** and **N** are uncorrelated signal and noise components, respectively) the response equals $\Sigma = \Sigma_S + \Sigma_N$ where Σ_S and Σ_N are

dispersion matrices for **S** and **N**, respectively. The signal-to-noise ratio (estimated from the ratio of mean and variance in a local window) for Y_i that needs to be maximised can be defined as (Lee *et al.* 1990; Nielsen & Larsen, 1994)

$$\frac{VAR\{a_i^T\mathbf{S}\}}{VAR\{a_i^T\mathbf{N}\}} = \frac{a_i^T\Sigma a_i}{a_i^T\Sigma_N a_i} - 1 = \frac{1}{\lambda_i} - 1 \; AND \; \frac{a_i^T\Sigma_N a_i}{a_i^T\Sigma a_i} = \lambda_i$$

the factors λ_i are the eigenvalues of Σ_N with respect to Σ and the factors a_i are the corresponding conjugate eigenvectors. The inherent spectral dimensionality of the data set can be found by examining the eigenvalues and associated MNF images. Some of these MNF images are associated with large eigenvalues and coherent (MNF) eigenimages while the remainder of the MNF bands have near-unity eigenvalues and images dominated by noise. Thus the MNF eigenvalues and eigenimages yield the absolute number of end-members required to model the image spectral response. The locations of the end member pixels in the image data are found using the Pixel Purity Index (PPI; Boardman *et al.* 1995). The PPI is based on the approach developed by Smith *et al.* (1985). This approach regards spectra as points in an *n*-dimensional space (*n* being the number of bands). The body (referred to as simplex) that spans the data points in a *n*=2-dimensional space is a triangle having *n*+1 facets. The purest end-members are found at the locations in this space where the sides of the triangle intersect. This principle can be extended to higher dimensions in a similar way. The PPI approach compares the pixels in a scene with the best fitting simplex and records the number of times a pixel is found at the extreme facets of the simplex. Portraying this as an image of cumulative count values allows identification of the locations in the data space of the initial set of spectrally pure end members. The resulting end member spectra were used as input to a spectral unmixing analysis to gain surface fractional abundance estimates of various ground cover types.

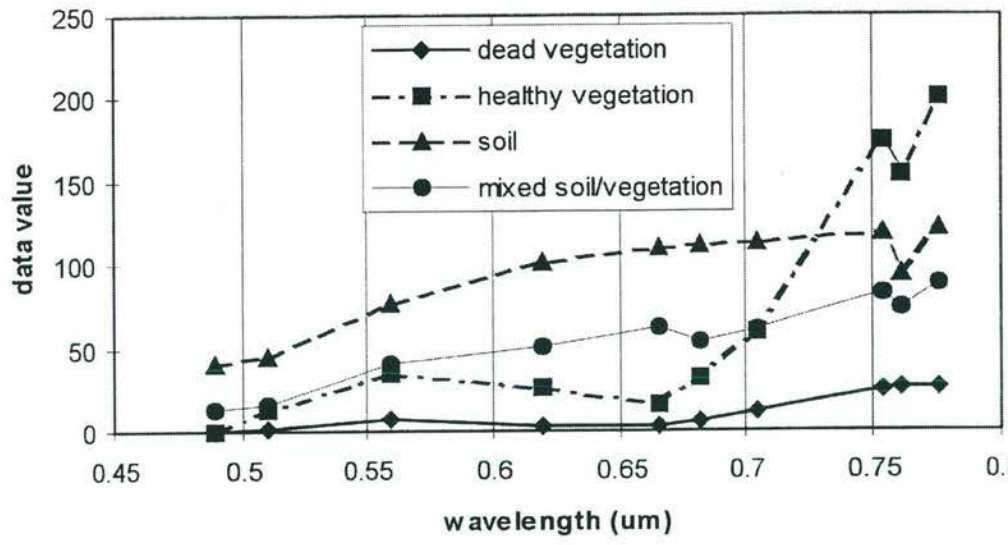

Figure 2. MERIS-type end members derived through pixel purity index.

Examples of some of the MERIS end members derived are shown in Figure 2. The unconstrained spectral unmixing technique we used is further described in Settle & Drake (1993). These authors define a vector of expected pixel signals $\mu_i = \{\mu_{i1}, \mu_{i2} \ldots\ldots \mu_{in}\}^T$ for the n ground cover classes giving an expected mixed pixel signal under strictly linear conditions as

$$f_1\mu_1 + f_2\mu_2 \ldots . f_c\mu_c = Mf$$

The columns of the matrix M are the vectors μ_i which are the end-member spectra. The observed signal of pure pixels will exhibit statistical fluctuations due to sensor noise characterised by a noise variance-covariance matrix N_i. Therefore pixels with the mixture f will

exhibit fluctuations around their mean value Mf characterized by the noise covariance matrix N(f) given by

$$N(f) = f_1 N_1 + f_2 N_2 .... + f_c N_c$$

If the N(f) is independent of f, thus when the noise components are un-correlated, the linear model can be defined according to Settle & Drake (1993) as

$$x = Mf + e$$

where e is the vector of errors satisfying

$$E(e) = 0 \text{ and } E(ee^T) = N$$

This signifies that the expectation of e is zero and that the expectation of noise component is close to the sensor noise component. The final result were end member abundance images for several end members of which we focus our analysis on the "vegetation" and "soil" end member. A first result derived from these end member abundance estimates is shown in Figure 3 where we have calculated the mean difference in the fraction for the different scales (i.e., pixel sizes) as compared to the 12 m. resolution results. From Figure 3 we can observe an inflection point in the behavior of the trends in abundances at 100 m. resolution. By means of geostatistical techniques, we will further analyze the spatial variability in the end member fraction images at the various spatial resolutions to better understand the observed discrepancy illustrated in Figure 3.

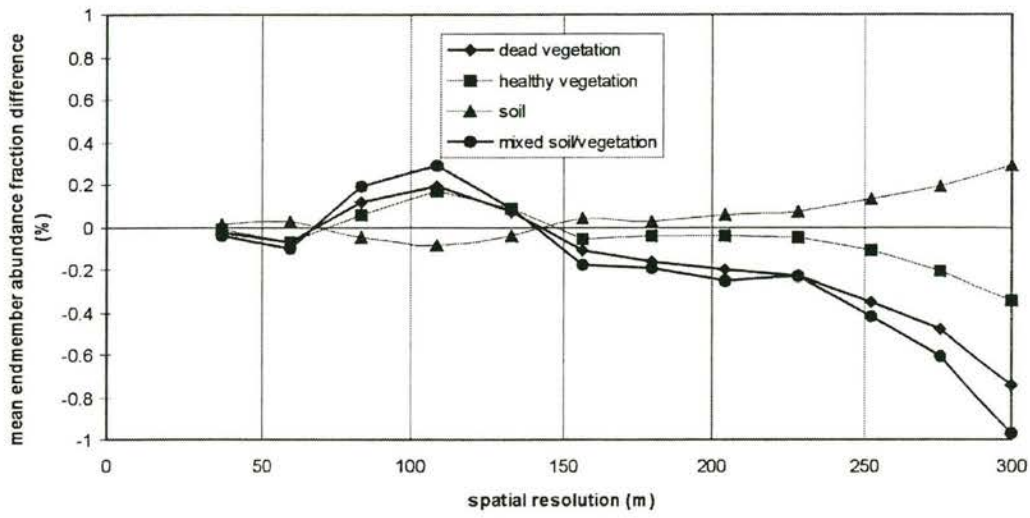

Figure 3. Mean difference of the abundance estimated at coarse resolution as compared to the highest possible resolution of 12 m.

8.3 Spatial variability

Regionalized variable theory assumes that spatial variation of a variable *z* can be expressed as the sum of three components

$$z(x) = m(x) + \varepsilon'(x) + \varepsilon''$$

where *x* is the position, *m(x)* is the structural component (a trend or a mean), $\varepsilon'(x)$ is the term denoting the stochastic, spatially dependent residuals from *m(x)*, and ε'' is a residual, spatially uncorrelated (Gaussian) noise. Once structural effects have been accounted for, the remaining variation is homogeneous in its variation, so that differences between samples should merely be a function of the distance between them. This spatial relationship can be expressed by a variogram (or semivariogram), which is a graph of semivariance versus sample spacing. The

variogram in remote sensing can be estimated from p(h) pairs of observations, $z_v(x_l)$ and $z_v(x_l + h)$ with l=1,2,...,p(h) as

$$\gamma(h) = 1/2p(h)\sum_{l=1}^{p(h)}\{z_v(x_l) - z_v(x_l + h)\}^2$$

Parameters of a fitted mathematical function (the variogram model) may include a range, a nugget and a sill. The range of the variogram indicates a spatial scale of the pattern, the nugget is an indication of the level of uncorrelated noise in the data and the sill reveals the total variation (Figure 4). Variograms of remotely sensed measurements should be interpreted with care. In remote sensing, the support size (the area or volume of the samples) equals the sample spacing. i.e. reflection values are averaged over the pixel size of the measuring device. Furthermore, the sensor's output is always a derivative of the complex composition of radiation from the terrain. Some major points for variogram interpretation are (De Jong & Burrough 1995; Figure 4)

- The range is related to sizes of objects in the terrain (for example patches of shrubs);
- The shape of the variogram is related to variability in size of objects in the terrain;
- The height of the variogram is influenced by the density of coverage of the objects and the spatial differences between the objects;
- Regularisation (coarsening the spatial resolution) reduces the overall variance of the data and blurs fine scale variation; consequently, the sill height will reduce, the range will increase and the nugget will increase;
- Anisotropy in the image is expressed by the variation of variogram parameters with the direction of the transect.

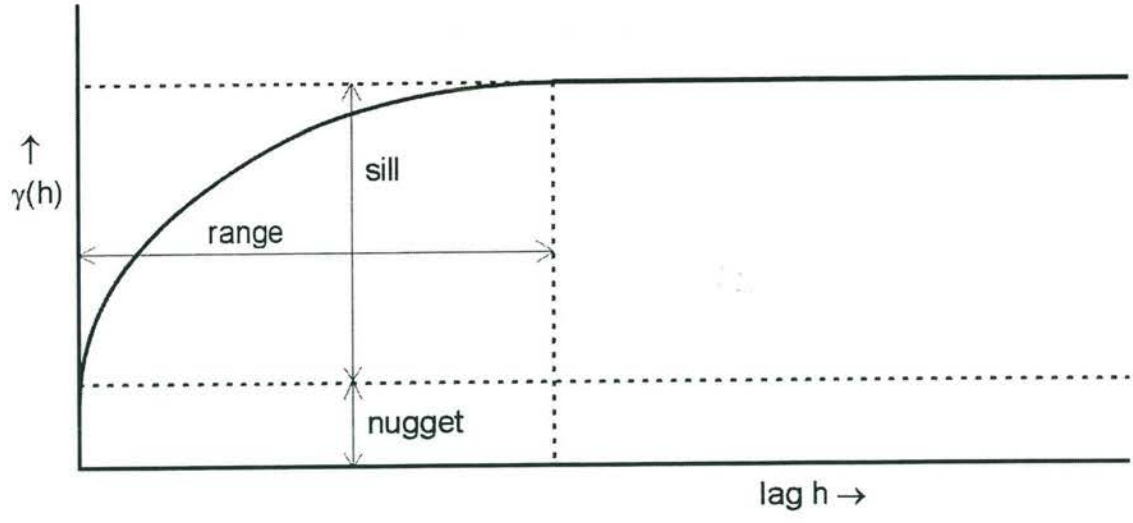

Figure 4. Illustration of a variogram model curve and indication of key parameters describing the model.

An effective way to detect and display anisotropies in the pattern occurring variability is a variogram surface. In this surface the (semi)variance is not only related to the mere distance between two points (the lag), but also to the direction. In calculating the variogram value for pairs of points separated by a vector (h_x, h_y) all pairs are grouped together whose separation is $h_x \pm \Delta x$, $h_y \pm \Delta y$. In this case Δx and Δy are half the support size, i.e. (in a rectangular coordinate system) the pixelsize (Isaaks & Srivastava, 1989). The result is a surface with for each vector a computed (semi)variance.

Variogram surfaces for simulated MERIS band 7 (Figure 5) were analyzed showing a strong directional anisotropy and little change in spatial structure with change in pixel size. Figure 6 shows two variogram surfaces for the end member abundance images for "soil" and

"vegetation" at 300 m. resolution again showing surprisingly little change in spatial structure between these end members.

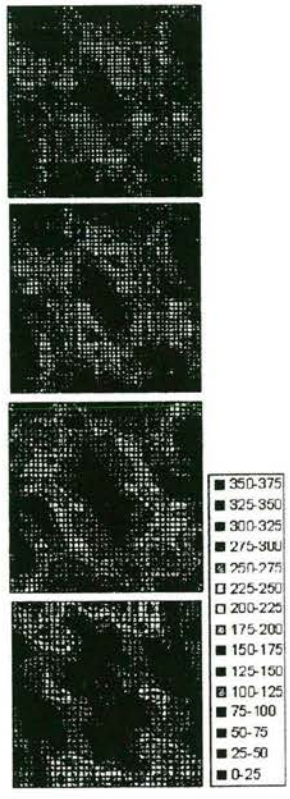

Figure 5. Variogram surfaces at (from top to bottom) 180, 204, 228 and 252 m. resolution for MERIS band 7 showing strong anisotropy.

8.4 Mapping accuracy: optimal sampling sizes.

Woodcock & Strahler (1987) developed a method for selecting an optimal spatial resolution in terms of the spatial variation of an image. Let $z(x_{ij})$ be the value of the pixel located at x_{ij} in the ith row and the jth column of an image. The local variance can be computed over a (2n+1) x (2m+1) window by

$$\sigma_{ij}^2 = 1/(2n+1)(2m+1)\sum_{k=i-n}^{i+n}\sum_{l=j-m}^{j+m}\{z(x_{kl}) - u_{ij}\}^2$$

where u_{ij} is the mean of the (2n+1) x (2m+1) window centered on x_{ij}. The local variance can be computed for varying pixel sizes using degraded image products. A plot of local variance versus pixel size allows selection of the optimal pixel size corresponding to the peak in variability (Figure 7). For the "soil" end member a decrease of local variance with spatial resolution is found thus indicating that the optimal sampling size is equal to the highest possible resolution. For the "vegetation" end member a peak is found at around 100 m. resolution. Thus not only do we observe difference between the sampling resolutions (i.e., pixel size) found to be optimal for different ground cover types, but they also both are smaller than the resolution to be imaged by MERIS (i.e., 300 m.). Another observation made is that the optimal scale for observing different components of spectral mixtures varies depending on the type of mixture. Again, the best possible resolution in all cases is below the envisaged 300 m. field of view.

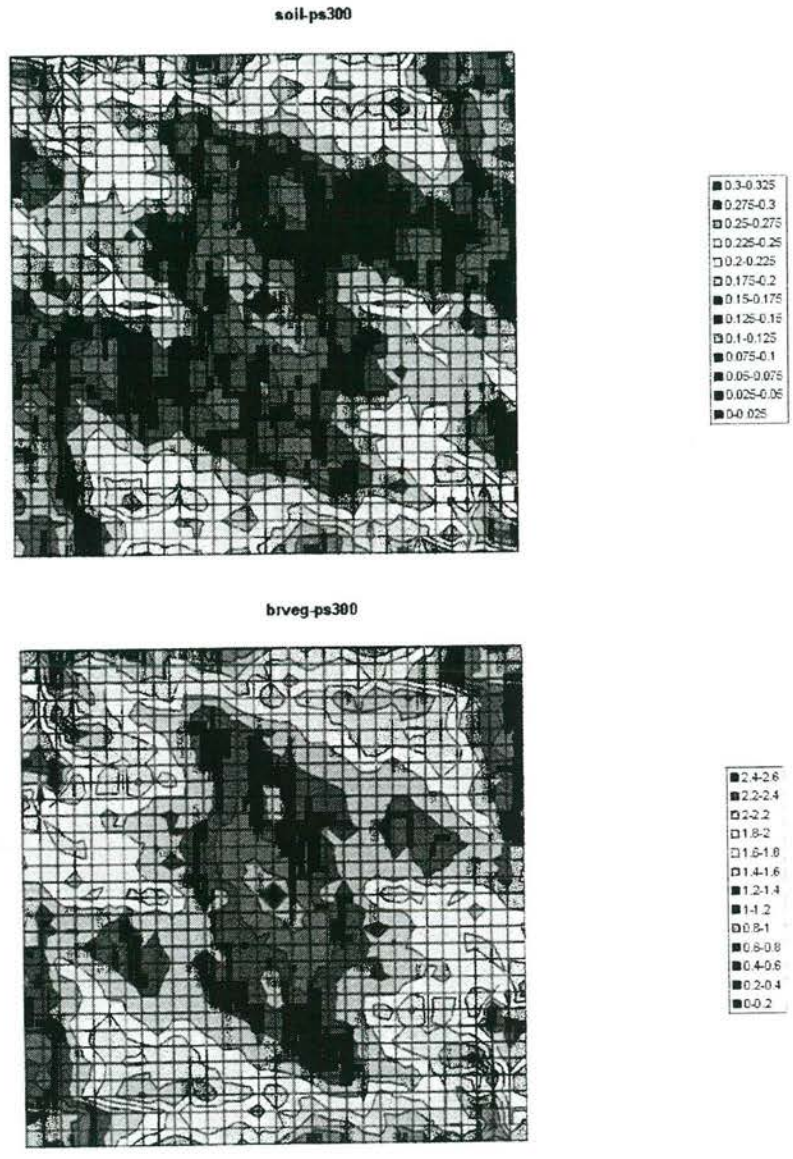

Figure 6. Variogram surfaces for the "soil" end member (top) and the "vegetation" end member (bottom) at the MERIS resolution of 300 m. (color plate 9)

8.5 Conclusions

Given the limitations of currently available airborne imaging spectrometer systems it has been shown that MERIS data can be simulated. In order to evaluate the spatial aspects of this data, variograms and variogram surfaces are calculated for MERIS band 7 and fractional abundance estimates for a "soil" and a "vegetation" endmember. These allow gaining insight into the nature of the data and its spatial dependency showing however little noticeable changes even at a sub-pixel level. However, when evaluating mapping accuracy clearly different optimal sampling sizes are found for the different end members. For both endmembers, the optimal sampling size corresponding to the peak in the local variance curve is found at finer resolution than the pixel size proposed for MERIS. We observe differences between the sampling resolutions (i.e., pixel size) found to be optimal for different ground cover types.

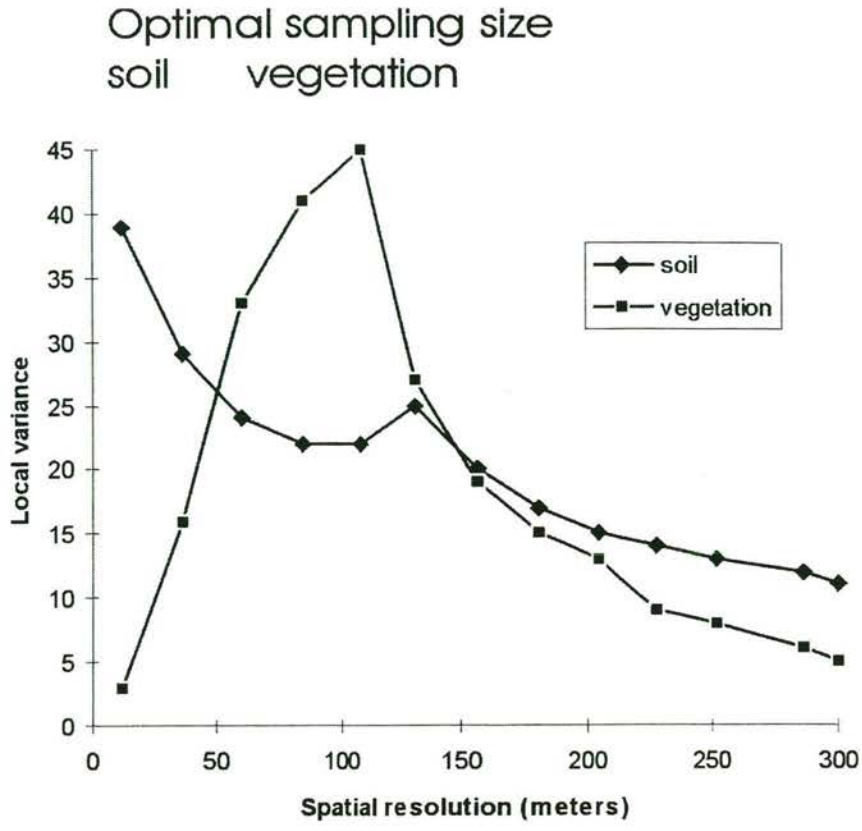

Figure 7. Plot of local variance versus pixel size. The peak of this curve corresponds to the optimal sampling ground resolution (pixel size) for imaging the designated class.

The optimal scale for observing different components of spectral mixtures varies depending on the type of mixture, however, the best possible resolutions in all cases of mixtures studied is below the envisaged 300 m. field of view for the MERIS sensor. The analysis of semivariogram surfaces clearly shows that the spatial distribution of the variance of the mixtures is invariant with scale, thus the observed mapping discrepancies are not related to the data processing but to the observations themselves.

Chapter 9

Final conclusions and recommendations for further studies

9.1 Introduction

The BCRS MERILAND project has been studying simulated images of MERIS. These simulated MERIS images were constructed from airborne spectroscopical imagery acquired by DAIS, GERIS and AVIRIS. The spatial resolution of these airborne images was degraded to the spatial resolution of MERIS. An important constraint of the simulated images was that the nominal spectral resolution of MERIS is much better than the actual spectral resolution of most of the previous mentioned airborne sensors. Consequently, within the MERILAND project it was difficult to assess the spectral performance of MERIS and the value of the high spectral resolution of MERIS.

9.2 Final conclusions

The use of ESA's Medium Resolution Imaging Spectrometer (MERIS) for various land applications has been investigated in this project. MERIS will provide 15 bands (although the system can be fully programmed) in the 400-900 nm. range at 300m resolution over land. The main objectives are directed toward oceanography, for land various vegetation products are envisaged. Existing airborne imaging spectrometer data sets including HyMAP (the Hyperspectral Mapper) data, DAIS (the Digital Airborne Imaging Spectrometer) and GERIS (the GER 63 channel imaging spectrometer) were used to simulate both spatially as well as spectrally the MERIS band set. None of these airborne sensors matches the spectral and radiometric characteristics of MERIS, hence the simulated image data sets provide a poor representation of the expected MERIS radiometric characteristics. The spatial characteristics can be optimally simulated. Furthermore, the study of simulation provides insights into up- and downscaling to the MERIS resolution. A MERIS spectral library containing field spectral measurements (at full and MERIS spectral resolution) of relevant ground cover has been compiled (MERISPEC) within the framework of the project. MERIS potential for land applications including soil mineralogy, vegetation indices and red edge positioning were examined. Soil mineralogical mapping, not a MERIS science objective, can yield relative abundance estimates of iron content and highlight iron bearing soils from non-iron bearing soils. No detailed mineralogical or soil constituent mapping can be done using MERIS. A

large number of standard vegetation indices including those that correct for soil background effects were prototyped using the MERIS specifications. These indices, although they differ amongst eachother, provide relatively constant estimates at varying spatial resolutions from 12m. up to the MERIS spatial resolution. A comparison of the MERIS NDVI and the DAIS (airborne equivalent) NDVI shows a good correlation. Comparisons of the MERIS NDVI to above ground biomass measured at field scale allows broad ground cover types such as garrigue, maquis and mixed oak forests to be classified, however at a relatively low accuracy. A red edge positioning algorithm has been developed for MERIS using PROSPECT-SAIL simulations for a canopy with a varying leaf chlorophyll content as input and using Airborne Visible/Infrared Imaging Spectrometer data (AVIRIS). Both experiments show that the MERIS standard band set can be used for deriving red edge index values. When evaluating the relation between optimal spatial sampling and spatial resolution for various land products such as soil type and vegetation it is concluded that the optimal spatial resolution for characterizing these ground cover types is at smaller spatial resolutions than the 300m. provided by MERIS. However it should be noted that statistically optimal does not necessary has to be the mission goal of the instrument.

9.3 Other related satellite missions

The first satellite imaging spectrometer to be expected was the LEWIS Hyperspectral Imager (HSI) from TRW company which was launched in 1997 but failed. It covered the 0.4-1.0 μm range with 128 bands and the 0.9 - 2.5 μm range with 256 bands of 5 nm and 6.25 nm band width respectively. Several other instruments are in the design stage. The turn of the millennium marks the onset of a new era in imaging spectrometry where we see the first satellite-based instruments being operational. A number of orbital imaging spectrometer missions are planned or being prepared currently. NASA is supporting the Japanese Advanced Spaceborne Thermal Emission and Reflectance Radiometer (ASTER), a high spectral resolution imaging spectrometer planned launched on December, 18, 1999 on the EOS AM1 now known as TERRA platform. The instrument is designed with three bands in the visible and near-infrared spectral range with a 15m spatial resolution, six bands in the short wave infrared with a 30m spatial resolution, and five bands in the Thermal infrared with a 90m spatial resolution. The VNIR and SWIR bands have a spectral resolution in the order of 10 nm. Simultaneously, a single band in the near-infrared will be provided along track for stereo capability. The swath width of an image will be 60km with 136km crosstrack and a temporal resolution of <16 days. Data products for ASTER are listed in Table 1.

Also on the TERRA is the Moderate resolution imaging spectroradiometer (MODIS) is planned as a land remote sensing instrument with high revisting time. MODIS is mainly designed for global change research. The MODIS instrument provides high radiometric sensitivity (12 bit) in 36 spectral bands ranging in wavelength from 0.4 μm to 14.4 μm. Two bands are imaged at a nominal resolution of 250 m at nadir, with five bands at 500 m and the remaining 29 bands at 1,000 m. MODIS achieves a 2,330-km swath and provides global coverage every one to two days. The optical system consists of a two-mirror off-axis a focal telescope which directs energy to four refractive objective assemblies; one for each of the VIS, NIR, SWIR/MWIR and LWIR spectral regions covering a total spectral range of 0.4 to 14.4 μm. Spectrally and radiometrically MODIS provides similar data products to MERIS.

Within the framework of the New Millennium Program NASA is launching the Hyperion on NMP Earth Observation (EO)-1. The Hyperion instrument (build by TRW) provides provides a high resolution hyperspectral imager capable of resolving 220 spectral bands (from 0.4 to 2.5 μm) with a 30 meter resolution. The instrument images a 7.5 km by 100 km land area per image and provides detailed spectral mapping across all 220 channels with high radiometric accuracy. EO-1 will fly in a 705 km circular, sun-synchronous orbit at a 98.7 degree inclination. This orbit allows EO-1 to match within one minute, the Landsat 7 orbit and collect identical images for later comparison on the ground. Once or twice a day,

sometimes more, both Landsat 7 and EO-1 will image the same ground areas (scenes). All three of the EO-1 land imaging instruments will view all or sub-segments of the Landsat 7 swath. Given the very narrow swath width and high spectral resolution and sampling, the hyperion will be a useful sensor for calibration of MERIS products, however be of limited value to global data assimilation projects.

Level	Product	Description
1B	Registered radiance at sensor	1A data with radioimetric and geometric coefficients applied
2	Decorrelation stretch	Enhanced color composites for each telescope
2	Brightness temperature	Radiance at the sensor converted to temperarture
2	Surface radiance-VNIR,SWIR	Radiance corrected for atmospheric effects
2	Surface radiance-TIR	Radiance corrected for atmospheric effects
2	Surface reflectance-VNIR,SWIR	Derived from surface radiance with topographic corrections
2	Surface kinetic temperature	Temperature-emissivity separation algorithm applied t atmospherically corrected surface radiance data.
2	Surface emissivity	Temperature-emissivity separation algorithm applied t atmospherically corrected surface radiance data.
4	Digital elevation model	DEM produced by stereo correlation of nadir and aft Band data

Table 1: ASTER data products.

DLR is currently operating the Modular Optoelectronic (MOS) Scanner from the shuttle mission. MOS is a spaceborne imaging pushbroom spectrometer in the visible and near infrared range of optical spectra (400 - 1010 nm) which was specially designed for remote sensing of the ocean-atmosphere system. MOS-PRIRODA and MOS-IRS instruments are identical providing 17 spectral channels with medium spatial resolution in the VIS/NIR. The advanced instrument built for the IRS spacecraft has one additional channel in the SWIR at 1.6μm. In terms of radiometric characteristics MOS and MERIS are almost identical, the difference being the operational altitude and the spatial resolution (300m. versus 500m.).

Other planned satellite hyperspectral sensor systems include ARIES, NEMO and orbiew-4. The planned Australian Resource Information and Environment Satellite (ARIES) will provide contiguous coverage from 400-1050nm (VNIR) with a minimum of 20nm band spacing and contiguous coverage from 2000-2500 (SWIR-2) with a minimum of 16nm band spacing. The pixel size is 30m. at nadir with 15km swath width. Two sets of 3 bands centred at 940 and 1140nm with minimum band spacing of 16nm for atmospheric correction. In total 105 bands will be acquired. The main aims of the system are directed toward mineral exploration and vegetation studies. The Naval EarthMap Observer (NEMO) is a space-based remote sensing system planned for launch in mid-2000 and aimed at collecting broad-area, synoptic, and unclassified Hyperspectral Imagery (HSI) for Naval Forces and the Civil Sector. A hyperspectral Coastal Ocean Imaging Spectrometer (COIS) will provide moderate spatial resolution with a 30/60 meter ground sample distance (GSD) at a 30 km swath width with high spectral resolution of 10 nanometers with a spectral range of 400 to 2500 nanometers. OrbView-4's imaging instrument developed by Orbimage will provide one-meter panchromatic imagery and eight-meter hyperspectral (24 m. to be released to the public) imagery with a swath width of 8 km as well as 200 channel hyperspectral imagery with a swath width of 5 km. The satellite will revisit each location on Earth in less than three days with an ability to turn from side-to-side up to 45 degrees from a polar orbital path. The spectral range is 400-2500nm.

9.4 Recommendations for further studies

In the new proposed study we will finally have the opportunity to work with real MERIS data. The analyses of real MERIS data in the proposed study will take full benefit of its high spectral resolution and will focus on the same topics: land cover and land cover changes, identification of ecozones and estimation of biophysical parameters of the land surface needed, e.g., for agricultural and environmental applications (including climate change issues). Due to political measures in the European Union and political changes in Eastern Europe, currently LUC changes occur on short time spans. The subsidy policy of the European Union influences the cropping systems in the EU. Due to differences in crops and cropping systems, the effects are different for Western and Southern Europe. Moreover, in many regions in Southern Europe land degradation poses serious effects on land cover and land use. In Eastern Europe changes are even larger due to the effects of privatisation and agrarian reform. Difficult economic conditions make actual and reliable information on land use and land cover (LUC) and on biophysical parameters of both vegetation and soils difficult to obtain and in recent years this situation resulted in decreasing agricultural production and in increasing environmental problems (like erosion). For monitoring purposes information on both land cover classification and quantitative estimation of land surface properties over large areas is essential.

Remote sensing offers the possibility to obtain both actual and reliable data on the land surface. The thematic detail of this data is determined by the spectral and spatial resolution of the imagery, which in practice limits the possibilities to detailed assessments of high spatial resolution images (30 m. and higher resolutions) or global assessments of low spatial resolution images (1100 m. and lower resolutions). The coverage of the images is in general varying inversely to their spatial resolution, i.e. high resolution images cover small areas, thus hampering detailed assessments of large areas. A lot of research towards LUC classifications and estimation of biophysical parameters at various scale levels has been performed thus far, but yet no good methodology has evolved for linking the various scale levels. Particularly the huge resolution gap between low and high spatial resolution images has been the cause.
Medium resolution satellite data, like MERIS data, are expected to be very important in future in filling the gap between the low resolution satellite data and the high resolution satellite data. For land applications MERIS has great potential for mapping and monitoring the land surface over large areas such as Europe. Because the area of a MERIS pixel is more than ten times smaller than an AVHRR pixel, it is expected that a significantly larger amount of detail can be identified than by using AVHRR-like data. In addition, it is expected that the high spectral resolution of MERIS will be another important feature.

To make optimal use of all available information, data from different aggregation levels have to be integrated by using both upscaling and downscaling approaches. Geostatistical techniques like co-kriging offer possibilities which have not been fully explored yet. By combining data from two aggregation levels with different, but partly overlapping, geographical extents co-kriging allows for extrapolation. Besides geostatistical information such as auto-correlation can be used for change detection, allowing for efficient monitoring.

Abbreviations and acronyms

4GL	Fourth Generation Programming Language
ASTER	Advanced Spaceborne Thermal Emission and Reflectance Radiometer
ATBD	Algorithm Theoretical Basis Document
ATCOR	Atmospheric Correction software
ASD	Analytical Spectral Devices
AVHRR	Advanced Very High Resolution Radiometer
AVIRIS	Airborne Visible/Infrared Imaging Spectrometer operated by NASA JPL
CASI	Compact Airborne Spectrographic Imager
CCD	Charged Coupled Device
CCSM	Cross Correlogram Spectral Matching
DAIS7915	79 channel Digital Airborne Imaging Spectrometer operated by DLR
DDV	Dense dark vegetation
DEMON	DEsertification MONitoring, project
DGPS	Difference Global Positioning System
DLR	Duetsche Forshungsanstalt fuehr Luft- und Raumfahrth e.V.
ENVISAT	ESA's Environmental Satellite
ENVI	Environment for Visualizing Images
ERS	ESA's Earth Resources Satellite
ESA	European Space Agency
GCP	Ground Control Point
GPS	Global Positioning System
FFT	Fast Fourier Transforms
FOV	Field of View
FR	Full Resolution Mode
FWHM	Full-width-half-maximum
GEMI	Global Environmental Monitoring Index
GER	Geophysical Environmental Research Corporation
GERAIS	GER 63 channel Airborne Imaging Spectrometer
GERIS	GER 63 channel Imaging Spectrometer (as above)
HyMAP	Hyperspectral Mapper
IDL	Interactive Data Language
IFOV	Instrument Field of View
JPL	Jet Propulsion Laboratory
JRC	Joint Research Center
LAI	Leaf area index
LOWTRAN	Low resolution transmittance code
LUT	Look-up table
MAIS	Modular Airborne Imaging Spectrometer
MAPP	MERIS Applications and Regional Products Project
MCA	Multi Criteria Analysis
MedSpec	A spectral database of Mediterranean environments
MERILand	MERIS Potential for Land Applications
MERIS	ESA's Medium Resolution Imaging Spectrometer
MERISPEC	A spectral database for MERIS
MMI	MERIS mineral index
MODIS	Moderate Resolution Imaging Spectrometer

MODTRAN	Moderate Resolution Transmittance Code
NASA	National Aeronautics and Space Administration
NIR	Near infrared wavelength region
MNF	Minimum Noise Fraction
MOA	Mean Orbital Altitude
MSAVI	Modified Soil Adjusted Vegetation Index
NCT	Nodal Crossing Time
NDVI	Normalized Difference Vegetation Index
Nm	Nanometer
PAGB	Photosynthetically active green biomass
PAR	Photosynthetically active radiation
PDOP	Position dilution of precision
PSF	Point spread (response) function
PVI	Perpendicular Vegetation Index
RMS	Root mean square
RT	Radiative transfer
ROI	Region of Interest
RR	Reduced Resolution Mode
SAVI	Soil Adjusted Vegetation Index
S/N	Signal to noise ratio
SNR	Signal to noise ratio
SRF	Spectral response function
SWIR	Shortwave Infrared wavelength region
TOA	Top of atmosphere
TSAVI	Transformed Soil Adjusted Vegetation Index
VI	Vegetation Indices
VIS	Visible wavelength region
VNIR	Visible to near infrared wavelength region
WDVI	Weighted Difference Vegetation Index
XRD	X-ray diffraction

Symbols used

μ	Band center
σ	Standard deviation (equivalent to the FWHM)
λ	Wavelength position of a channel
$R_i(\lambda)$	Channel spectral response function
$\rho_{res}(\lambda_i)$	Re-sampled spectrum
$\rho\ (\lambda)$	Continuous spectrum
$e_b(x,y)$	Electronic signal for band *b* at location given by coordinate (x,y)
$s_b(\alpha,\beta)$	Input signal
α	Constant over which physical signal is weighted
β	Constant over which physical signal is weighted
r_m	The cross correlation at match position *m* for CCSM
λ_t	The test spectrum for CCSM
λ_r	The reference spectrum for CCSM
N	The number of overlapping positions (spectral bands) for CCSM
m	The match position for CCSM
n	Degree of freedom for CCSM
R_M	The pixel cross correlation at match position *m* for CCSM
R'_M	The reference cross correlation at match position *m* for CCSM
$z(x_{ij})$	Value of pixel located at x_{ij} in the ith row and the jth column of a image
u_{ij}	The mean of the (2n+1) x (2m+1) window centered on x_{ij}.
h	Height of trees
d	Diameter of trees
N	Counts of trees
R_{re}	Vegetation red edge inflexion point
λ_{re}	Wavelength of the vegetation red edge
w_1	Kriging weight
Ψ	Lagrange multiplier used in kriging
γ	Semivariance
C	Covariance matrix of observation points
D	Covariance matrix of observations versus estimated point
ε_r	Kriging mean residual error
σ^2_r	Kriging variance
c_0	Variogram nugget values
c_1	Variogram sill value
a	Variogram range value
Z(x)	Stochastic variable
E(Z)	Expectation of Z(x)
D(Z)	Dispersion of Z(x)
$\sum_S$	Signal matrix
$\sum_N$	Noise matrix
λ_i	Eigenvalues of matrix $\sum_N$

a_i	Conjugate eigenvectors of $\sum_N$
μ_i	Endmember spectra of endmember i
f_i	Fraction of endmember i
e	Vector of errors

References

Abrams, M. & Hook, S.J. 1995. Simulated ASTER data for geologic studies. *IEEE Transactions on Geoscience and Remote Sensing,* **33**: 692-699.

Adams, J.B. 1974. Visible and near-infrared diffuse reflectance: Spectra of pyroxenes as applied to remote sensing of solid objects in the solar system. *Journal of Geophysical Research,* **79**: 4829-4836.

Adams, J.B. 1975. Interpretation of visible and near-infrared diffuse reflectance spectra of pyroxenes and other rock forming minerals. In*: Infrared and Raman Spectroscopy of Lunar and Terrestrial Materials*, C. Karr (ed.),.Academic Press, New York: pp: 91-116.

Allen, W.A., Gausman, H.W., Richardson, A.J. & Thomas, J.R. 1969. Interaction of isotropic light with a compact plant leaf. *Journal of the Optical Society of America*, **59**: 1376-1379.

Allen, W.A., Gausman, H.W. & Richardson, A.J. 1970. Mean effective optical constants of cotton leaves. *Journal of the Optical Society of America*, **60**: 542-547.

Asrar G. (ed.), 1989. *Theory and applications of optical remote sensing*. John Wiley & Sons Ltd., New York, 734p.

Atkinson, P.M. & Curran, P.J. 1995. Optimal size of support for remote sensing investigations: defining an optimal sampling strategy. *IEEE Transaction on Geoscience and Remote Sensing,* **33**: 768-776.

Atkinson, P.M., Curran, P.J. & Webster, R. 1990. Sampling remotely sensed imagery for storage, retrieval and reconstruction. *Professional Geography*, **37**: 345-353.

Atkinson, P.M., Webster, R. & Curran, P.J. 1994. Cokriging with airborne MSS imagery. *Remote Sensing of Environment,* **50**: 335-345.

Atkinson, P.M. 1997. On estimating measurement error in remotely-sensed images with the variogram. *International Journal of Remote Sensing,* **18**: 3075-3084.

Baret, F., Guyot, G. & Major, D. 1989. TSAVI: a vegetation index which minimizes soil brightness effects on LAI and APAR estimation. In: *Proceedings of the 12th Canadian Symposium on Remote Sensing and IGARSS'90.*Vancouver, Canada, 10-14 July 1989: 4pp.

Baret, F. & Guyot, G. 1991. Potentials and limits of vegetation indices for LAI and APAR assessment. *Remote Sensing of Environment,* **35**: 161-173.

Bézy, J.L., Morel, M., Rast, M. & Bardey, P. 1990. Signal detection of MERIS in oceanographic applications. In: *Proceedings of the Space and Sea Colloquium,* Paris, September 24-26 1990, ESA-SP 312: pp.285-290.

Bézy, J.L., Rast, M., Delwart, S., Merheim-Kealy, P. & Bruzzi, S. 1996. The ESA Medium Resolution Imaging Spectrometer (MERIS). *Backscatter* **7**(3): 14-19.

Boardman, J.W., Kruse, F.A. & Green, R.O. 1995. Mapping target signatures via partial unmixing of AVIRIS data. In: *Proceedings of the Fifth JPL Airborne Earth Science Workshop*, JPL Publication 95-1, Vol.1: pp. 23-26.

Bolin, B., Doos, B., Jager, J. & Warrick, R.1986. The Greenhouse Effect, Climate Change, and Ecosystems. *Scope* **29**, John Wiley & Sons Ltd., New York, 541 pp.

Bonham-Carter, G.F. 1988. Numerical procedures and computer program for fitting an inverted gaussian model to vegetation reflectance data. *Computers and Geosciences*, **14**: 339-356.

Bricaud, A. & Morel, A. 1995. MERIS Potential for Ocean Colour Studies in the Open Ocean. In: *Proceedings of the 21st Annual Conference of the Remote Sensing Society, RSS 95, Remote Sensing in Action,* P.J. Curran & Y.C. Robertson (eds.), 11-14 September 1995, University of Southampton: pp.133-140.

Brown, L. & Wolf, E. 1984. *Soil Erosion: Quiet Crisis in the World Economy. Worldwatch Paper*, No. 60, Worldwatch Institute, Washington DC, 49 pp.

Buckton, D., O'Mongain, E. & Danaher, S. Designing optimal spectral indices: a feasibility and proof of concept study. *International Journal of Remote Sensing*, **20**: 1841-1851.
Büker, C. & Clevers, J.G.P.W. 1992. *Imaging spectroscopy for agricultural applications.* Report LUW-LMK-199206, Dept. Landsurveying and Remote Sensing, Wageningen Agricultural University, The Netherlands.

Bunnik, N.J.J. 1978. *The multispectral reflectance of shortwave radiation by agricultural crops in relation with their morphological and optical properties.* PhD Thesis, Mededelingen Landbouwhogeschool Wageningen 78-1, Wageningen, The Netherlands.

Burns, R.G. 1970. *Mineralogical Application to Crystal Field Theory.* Cambridge University Press, Cambridge, 224 p.

Burrough, P.A. 1986. *Principles of Geographic Information Systems for Land Resources Assessment.* Oxford University Press, New York, 147 p.

Chang, S., Westfield, M.J., Lehmann, F., Oertel, D. & Richter, R. 1993. A 79 - Channel Airborne Imaging Spectrometer. In: Proceedings of SPIE, Vol. 1937: pp. 164 - 172.

Clark, R.N., King, T.V.V., Kleijwa, M., Swayze, G.A. & Vergo, N. 1990. High spectral Resolution Reflectance Spectroscopy of Minerals. *Journal of Geophysical Research,* **95**: 12653-12680.

Clark, R.N., Livo, K.E. & Kokaly, R.F. 1998. Geometric Correction of AVIRIS Imagery Using On-Board Navigation and Engineering Data. In: *Summaries of the 7th Annual JPL Airborne Earth Science Workshop.* R.O.Green (ed.), January 12-14 1998: 9 pp.

Clevers, J.P.G.W. 1988. The derivation of a simplified reflectance model for the estimation of Leaf Area Index. *Remote Sensing of Environment,* **25**: 53-69.

Clevers, J.G.P.W. 1992. *Modelling and synergistic use of optical and microwave remote sensing. Report 4: Influence of leaf properties on the relationship between WDVI and LAI: a sensitivity analysis with the SAIL and the PROSPECT model.* Report 92-14, BCRS, Delft.

Clevers, J.G.P.W. 1994. Imaging spectrometry in agriculture - Plant vitality and yield indicators. In: *Imaging Spectrometry - A Tool for Environmental Observations*. J. Hill & J. Mégier (eds.), Kluwer Academic Press, Dordrecht: pp. 193-219.

Clevers, J.G.P.W. 1999. The use of imaging spectrometry for agricultural applications. *ISPRS Journal of Photogrammetry and Remote Sensing*, in press.

Clevers, J.G.P.W. & Büker, C. 1991. Feasibility of the red edge index for the detection of nitrogen deficiency. In: *Proceedings 5th Int. Coll. Physical Measurements and Signatures in Remote Sensing*, Courchevel, ESA SP-319: pp. 165-168.

Clevers, J.G.P.W., Büker, C., Van Leeuwen, H.J.C. & Bouman, B.A.M. 1994. A framework for monitoring crop growth by combining directional and spectral remote sensing information. *Remote Sensing of Environment*, **50**: 161-170.

Clevers, J.G.P.W. &Verhoef, W. 1993. LAI estimation by means of the WDVI: a sensitivity analysis with a combined PROSPECT-SAIL model. *Remote Sensing Reviews*, **7**: 43-64.

Collins, W. & Chang, S. 1990. The Geophysical Environmental Research Corp. 63 Channel Airborne Imaging Spectrometer and 12 Band Thermal Scanner. In: Proceedings of SPIE, Vol. 1298: pp. 62-71.

Curran, P.J. 1988. The semivariogram in remote sensing: an introduction. *Remote Sensing of Environment*, **24**: 493-507.

Curran, P.J. & Dungan, J.L. 1989. Estimation of signal-to-noise: a new procedure applied to AVIRIS data. *IEEE Transaction on Geoscience and Remote Sensing*, **27**: 630-628.

Curran P.J., Dungan, J.L., Macler, B.A. & Plummer, S.E. 1991. The effect of a Red Leaf Pigment on the relationship between Red Edge and Chlorophyll concentration. *Remote Sensing of Environment*, **35**: 69-76.

Cutter, M.A., Lobb, D.R., Ramon, Y., Ratier, G. & Bézy, J. 1989. A Medium Resolution Imaging Spectrometer for the European Polar Orbiting Platform. In: *Advanced Optical Instrumentation for Remote Sensing of the Earth's Surface from Space (SPIE)*, Vol. **1129**: pp.107-116.

Dawson T.P. & Curran, P.J. 1998. A new technique for interpolating the reflectance red edge position. *International Journal of Remote Sensing*, **19**: 2133-2139.

De Jong, S.M. & Burrough, P.A. 1995. A fractal approach to the classification of Mediterranean vegetation types in remotely sensed images. *Photogrammetric Engineering and Remote Sensing*, **61**: 1041-1053.

De Jong, S.M., Scholte, K., van der Meer, F., Sommer, S. & Lacaze, B. 1998. The DAIS7915 La Peyne experiment: using airborne imaging spectrometry for land degradation survey and modeling. In: *Operational remote sensing for Sustainable Development*. G.J.A. Nieuwenhuis, R.A. Vaughan and M. Molenaar (eds.), A.A. Balkema, Rotterdam: pp. 247-253.

Demetriades-Shah T.H. & Steven, M.D. 1988. High spectral resolution indices for monitoring crop growth and chlorosis. In: *Proceedings 4th Int. Coll. Spectral Signatures of Objects in Remote Sensing*, Aussois, France, ESA SP-287: pp. 299-302.

Demetriades-Shah T.H., Steven, M.D. & Clark, J.A. 1990. High resolution derivative spectra in remote sensing. *Remote Sensing of Environment*, **33**: 55-64.

Doerffer, R, Sörensen, K. & Aiken, J. 1995. MERIS: Potential for Coastal Zone Application. In: *Proceedings of the 21st Annual Conference of the Remote Sensing Society, RSS 95, Remote Sensing in Action.* P.J. Curran and Y.C. Robertson (eds.), 11-14 September 1995, University of Southampton: pp.166-175.

Dungan, J.L., Peterson, D.L. & Curran, P.J. 1994. Alternative approaches for mapping vegetation quantities using ground and image data. In: *Environmental information management and analysis: ecosystem to global scales*. W. Michener, S. Stafford & J. Brunt (eds.). Taylor & Francis, London: pp. 237-261.

Elvidge, C.D. 1990. Visible and near infrared reflectance characteristics of dry plant materials. *International Journal of Remote Sensing*, **11**: 1775-1795.

Elvidge, C.D. & Lyon, R.J.P. 1985. Influence of rock-soil spectral variation on the assessment of green biomass. *Remote Sensing of Environment,* **17**: 265-279.

ESA, 1995. *MERIS: The Medium Resolution Imaging Spectrometer*. Report SP-1184, ESA, Paris.

ESA, 1997. *Envisat-1 Mission & System Summary*. Report ESTEC-ESA, Noordwijk, The Netherlands, p. 84.

Fan, L., van der Meer, F. & Bodechtel, J. 1997. Geological information extraction from airborne hyperspectral data and field spectral data in a heavily soil and vegetation covered area. In: *Proceedings of the Third International Airborne Remote Sensing Conference and Exhibition*, 7-10 July 1997, Copenhagen, Denmark, Vol. I: pp. 665-672.

Fischer, J. & Santer, R. 1995. Remote Sensing of Atmospheric Properties. A Perspective View of MERIS Applications. In: *RSS 95, Remote Sensing in Action, Proceedings of the 21st Annual Conference of the Remote Sensing Society*, P.J. Curran and Y.C. Robertson (eds.), 11-14 September, University of Southampton: pp.149-156.

Floret C., Galan, M.J., Le Floc'h, E., Rapp, M. & Romane, F. 1989. Organisation de la Structure, de la Biomasse et de la Minéralomasse d'un Taillis Overt de Chêne Vert (Quercus ilex L.) *Acta Oecologica*, **10**: 245-262.

Gobron, N., Pinty, B., Verstraete, M. & Govaerts, Y. 1999. The MERIS Global Vegetation Index (MGVI): description and preliminary application. *International Journal of Remote Sensing,* **20(9)**: 1917-1927.

Goel, N.S. 1989. Inversion of canopy reflectance models for estimation of biophysical parameters from reflectance data. In: *Theory and Applications of Optical Remote Sensing*, G. Asrar (ed.), John Wiley & Sons, New York: pp. 205-251.

Govaerts, Y.M., Verstraete, M.M., Pinty, B. & Gobron, N. 1999. Designing optimal spectral indices: a feasibility and proof of concept study. *International Journal of Remote Sensing*, **20**: 1853-1873.

Green, A.A., Berman, M., Switzer, P. & Craig, M.D. 1988. A transformation for ordering multispectral data in terms of image quality with implications for noise removal. *IEEE Transactions on Geoscience and Remote Sensing*, **26(1)**: 65-74.

Green, A.A. & Graig, M.D. 1985. Analysis of aircraft spectrometer data with logarithmic residuals. NASA-JPL Publication 85-41: pp. 111-119.

Grove, C.I., Hook, S.J. & Paylor II, E.D. 1992. Laboratory Reflectance Spectra of 160 minerals, 0.4 to 2.5 Micrometers. NASA-JPL Publication 92-2, Pasadena: 300 pp.

Guyot G, & Baret, F. 1988. Utilisation de la haute resolution spectrale pur suivre l'etat des couverts vegetaux, In: *Proceedings of the 4th International Colloquium on Spectral Signatures of Objects in Remote Sensing*, Aussios, France, 18-22 January 1988, ESA SP-287: pp. 279-286.

Hecht, S. & Cockburn, A. 1989. *The Fate of the Forest*. Verso, London, 266 pp.

Heinemans, Th. & Fischer, J. 1995. Aerosol Remote Sensing over Oceans. *Advances in Space Research*, **16**(10): 99-102.

Horler, D.N.H., Dockray, M. & Barber, J. 1983. The red edge of plant leaf reflectance. *International Journal of Remote Sensing*, **4**: 273-288.

Huete, A.R. 1988. A Soil-Adjusted Vegetation Index (SAVI). *Remote Sensing of Environment*, **25**: 295-309.

http://envisat.estec.esa.nl/: ENVISAT homepage

http://www.frw.ruu.nl:80/fg/demon.html: DEMON homepage

http://www.asdi.com/asd/prod/fs_fr.html: ASD homepage

http://makalu.jpl.nasa.gov.html/adf.html: AVIRIS homepage

http//www.estec.esa.nl/envisat/Satellite/Instruments/MERIS/: MERIS homepage

Hudgon, S.J. Moore, G., Bale, A.J., Dyer, K.R. & Aiken, J. 1994. An operational approach to determining suspended distributions in the Humber estuary by airborne multi-spectral imagery. In: *Proceedings of the First International Airborne Remote Sensing Conference*, Strassbourg, France, Vol.**3**: pp.10-20.

Hunt, G.R. 1977. Spectral signatures of particulate minerals in the visible and near-infrared. *Geophysics*, **42**: 501-513.

Hunt, G.R. & Salisbury, J.W. 1970. Visible and near-infrared spectra of minerals and rocks, I. Silicate Minerals. *Modern Geology*, **1**: 283-300.

Isaaks, E.H. & Srivastava, R.M. 1989. *Introduction to Applied Geostatistics*. Oxford University Press, New York: pp. 279-290.

Janssen, I. & van der Kolff, G. 1997. Co-operation between Belgium, Germany and The Netherlands regarding MERIS. *Remote Sensing Nieuwsbrief*, **20(75)**: 16-17.

Jacquemoud S. & Baret, F. 1990. PROSPECT: a model of leaf optical properties spectra. *Remote Sensing of Environment*, **34**: 75-91.

Justice, C.O., Markham, B.L., Townshend, J.R.G. & Kennard, R.L. 1989. Spatial degradation of satellite data. *International Journal of Remote Sensing*, **10(9)**: 1539-1561.

Kramer, H.J. 1996. *Observation of the Earth and Its Environment* (3rd edition). Springer-Verlag, Berlin, 960pp.

Kaufman, Y.J., Wald, A.E., Remer, L.A., Gao, B.C., Li, R.R. & Flynn, L. 1997. The MODIS 2.1-μm channel-correlation with visible reflectance for use in remote sensing of aerosol. *IEEE Transactions on Geoscience and Remote Sensing,* **35**: 1286-1298.

Kleverlaan, K. 1989. Neogene history of the Tabernas basin (SE Spain) and its Tortonian submarine fan development. *Geologie & Mijnbouw*, **68**: 421-432.

Lacaze B., Casselles, V., Coll, C., Hill, J., Hoff, C., de Jong, S.M., Mehl, W., Negendank, J.F.W., Riezebos, H.Th., Rubio, E., Sommer, S., Teixeira Filho, J. & Valor, E. 1996. *Integrated Approaches to Desertification Mapping and Monitoring in the Mediterranean Basin*. Final Report DeMon-1 Project. Joint Research Center EUR 16448 EN: 165 pp.

Lee, J.B., Woodhyatt, S., and Berman, M., 1990, Enhancement of high spectral resolution remote-sensing data by a noise-adjusted principal components transform. *IEEE Transactions on Geoscience and Remote Sensing*, **28**, 295-304.

Merheim-Kealy, Delwart, P.S. & Arino, O. 1995. The MERIS Ground Segment and its Data Products. In: *Proceedings of the 21st Annual Conference of the Remote Sensing Society RSS 95, Remote Sensing in Action.* P.J. Curran and Y.C. Robertson (eds.), 11-14 September 1995, University of Southampton: pp.141-148.

Merheim-Kealy, P., Huot, J.P., and Delwart, S. 1999. The MERIS ground segment. *International Journal of Remote Sensing*, **20(9)**: 1703-1712.

Meyer, P. 1994. A parametric approach for the geocoding of Airborne Visible/Infrared Imaging Spectrometer (AVIRIS) data in rugged terrain. *Remote Sensing of Environment*, **49(2):**118-130.

Morel, M., Bézy, J.L., Montagner, F., Morel, A. & Fischer, J. 1993. Envisat's Medium-Resolution Imaging Spectrometer: MERIS. *ESA-Bulletin*, **76**: 40-46.

Nielsen, A.A., and Larsen, R., 1994, Restoration of GERIS data using the Maximum Noise Fractions Transform. In *Proceedings of the First International Airborne Remote Sensing Conference and Exhibition (ERIM),* Strassbourg, France (Ann Arbor: ERIM International): pp. 557-568.

Pereira J.M.C., Oliviera, T.M. & Paúl, C.P. 1993. Fuel Mapping in a Mediterranean Shrubland Using Landsat TM imagery. In*: Satellite Technology and GIS for Mediterranean Forest Mapping and Fire Management*, P.J. Kennedy and M. Karteris (eds.), Technical JRC Report EUR15861 EN: pp. 97-106.

Pinty, B., Leprieur, C. & Verstraete, M.M. 1993. Towards a quantitative interpretation of vegetation indices. Part I: Biophysical canopy properties and classical indices. *Remote Sensing Reviews,* **7**: 127-150.

Pinty, B. & Verstraete, M.M. 1991. Bidirectional reflectance and surface albedo: Physical modeling and inversion. In: *Proceedings of the 5th International Colloquim – Physical measurements and signatures in remote sensing,* Courchevel, France, January 14-18 1991 (ESA SP-391, May 1991): pp. 383-386.

Qi, J., Chehbouni, A., Huete, A.R. & Kerr, Y.H. 1994. Modified Soil Adjustedf Vegetation Index (MSAVI). *Remote Sensing of Environment,* **48**: 119-126.

Rast, M. & Bézy, J.L. 1990. ESA's Medium Resolution Imaging Spectrometer (MERIS): mission, system and applications. In: *Procedings SPIE*, **1298**: pp. 114-126.

Rast, M., Bézy, J.L. & Bruzzi, S. 1999. The ESA Medium Resolution Imaging Spectrometer MERIS – a review of the instrument and its mission. *International Journal of Remote Sensing*, **20**: 1681-1702.

Rast, M., Bézy, J.L., Morel, M. & Fanton d'Andon, O. 1991. The performance of the ESA Medium Resolution Imaging Spectrometer (MERIS). In: *Physical Measurements and Signatures in Remote Sensing Proceedings of the 5th International Colloquium*. J.J. Hunt (ed.), 14-18 January 1991, Courchevel, France, ESA SP-319: pp.147-152.

Rast, M. & Bézy, J.L. 1995. The ESA Medium Resolution Imaging Spectrometer (MERIS): Requirements to its Mission and Performance of its System. In: *Proceedings of the 21st Annual Conference of the Remote Sensing Society, RSS 95, Remote Sensing in Action.* P.J. Curran and Y.C. Robertson (eds.), 11-14 September 1995, University of Southampton: pp.125-132.

Richardson, A.J. & Wiegand, C.L. 1977. Distinguishing vegetation from soil background information. *Photogrammetric Engineering and Remote Sensing,* **43**: 1541-1552.

Richter, R. 1996. Atmospheric correction of DAIS hyperspectral data. *Computers & Geosciences,* **22**: 785 - 793.

Rossi, R.E., Dungan, J.L. & Beck, L.R. 1994. Kriging in the shadows: geostatistical interpolation for remote sensing. *Remote Sensing of Environment*, **49**: 32-40.

Santer, R., Carrere, V., Dubuisson, P. & Roger, J.C. 1999. Atmospheric correction over land for MERIS. *International Journal of Remote Sensing*, **20**: 1819-1840.

Scholte, K., Gieske, A., Van der Meer, F., Bakker, W., Skidmore, A., Clevers, J., Epema, G. & De Jong, S. 1999. Geometric correction of DAIS 7915 imaging spectrometer data using a Moving Average kriging based approach. In preparation.

Schowengerdt, R.A., 1997. *Remote Sensing – models and methods for image processing* (2nd edition). Academic Press, Boston, 522 pp.

Settle, J.J. & Drake, N.A. 1993. Linear mixing and the estimation of ground cover proportions. *International Journal of Remote Sensing* **14**, 1159-1177 (1993).

Smith, M.O., Johnston, P.E. & Adams, J.B. 1985. Quantitative determination of mineral types and abundances from reflectance spectra using principal component analysis. *Journal of Geophysical Research,* **90**: 797-804.

Stein, A., Bastiaanssen, W.G.M., de Bruin, S., Cracknell, A.P., Curran, P.J., Fabbri, A.G., Gorte, B.G.H., van Groenigen, J.W., van der Meer, F. & Saldaña, A. 1998. Integrating spatial statistics and remote sensing. *International Journal of Remote Sensing*, **19:** 1793-1814.

Stewart, J.B., Engman, E.T., Feddes, R.A. & Kerr, Y.H. 1998. Scaling up in hydrology using remote sensing: summary of a workshop. *International Journal of Remote Sensing*, **19**: 181-194.

Strobl, P., Nielsen, A., Lehmann, F., Richter, R. & Mueller, A. 1996. DAIS System Performance, First results from the 1995 Evaluation Campaigns, In: *Proceedings of the 2nd International Airborne Remote Sensing Conference and Exhibition, San Francisco*, Vol.**2**: pp. 325-334.

Strobl, P., Richter, R., Lehmann, F., Mueller, A., Zhukov, B. & Oertel, D. 1996. Pre-processing for the Airborne Imaging Spectrometer DAIS 7915. In: *Proceedings SPIE*, Vol. **2758**: pp. 375-382.

Teillet, S. & Staenz, K. 1992. Atmospheric Effects Due to Topography on MODIS Vegetation Index Data Simulated From AVIRIS Imagery over Mountainous Terrain. *Canadian Journal of Remote Sensing,* **18**: 443-441.

Teillet P.M, Staenz, K. & Williams, D.J. 1997. Effects of spectral, spatial, and radiometric characteristics on remote sensing vegetation indices of forested regions. *Remote Sensing of Environment,* **61**: 139-149.

Tucker, C.J. 1979. Red and photographic infrared linear combinations for monitoring vegetation. *Remote Sensing of Environment,* **10**: 127-150.

UNCOD 1977. *Desertification: Its Causes and Consequences*. Pergamon Press, Oxford, 448 pp.

Van den Bosch, J. & Alley, R. 1990. Application of LOWTRAN 7 as an atmospheric correction to Airborne Visible/Infrared Imaging Spectrometer (AVIRIS) data. In: *Proceedings of the second Airborne Visible/Infrared Imaging Spectrometer (AVIRIS) Workshop*, R.O. Green (ed.), JPL-Publication 90-54: pp. 78-81.

Van der Meer, F. 1994. Extraction of mineral absorption features from high-spectral resolution data using non-parametric geostatistical techniques. *International Journal of Remote Sensing*, **15**: 2293-2214.

Van der Meer, F. 1998. Mapping dolomitization through a co-regionalization of simulated field and image-derived reflectance spectra; a proof-of-concept study. *International Journal of Remote Sensing*, **19**: 1615-1620.

Van der Meer, F. & Bakker, W. 1997a. CCSM: Cross Correlogram Spectral Matching. *International Journal of Remote Sensing*, **18(5)**: 1197-1201.

Van der Meer, F. & Bakker, W. 1997b. Cross Correlogram Spectral Matching (CCSM): application to surface mineralogical mapping using AVIRIS data from Cuprite, Nevada. *Remote Sensing of Environment*, **61(3)**: 371-382.

Van der Woerd, H. & Dekker, A. 1997. De MERIS workshop. Remote Sensing Nieuwsbrief, **20(77):** 47-48.

Verhoef, W. 1984. Light scattering by leaf layers with application to canopy reflectance modelling: the SAIL model. *Remote Sensing of Environment*, **16**: 125-141.

Verhoef, W. & Bunnik, N.J.J. 1981. Influence of crop geometry on multispectral reflectance determined by the use of canopy reflectance models. In*: Proceedings Int. Coll Signatures of Remotely Sensed Objects*, Avignon, France: pp. 273-290.

Verstraete, M.M., Pinty, B. & Curran, P.J. 1995. MERIS Potential for Land Applications. In: *Proceedings of the 21st Annual Conference of the Remote Sensing Society, RSS 95,*

Remote Sensing in Action. P.J. Curran and Y.C. Robertson (eds.), 11-14 September 1995, University of Southampton: pp.157-165.

Verstraete, M.M., Pinty, B. & Curran, P.J. 1999. MERIS potential for land applications. *International Journal of Remote Sensing*, **20**: 1747-1756.

Wessman, C.A. 1994. Estimating canopy biochemistry through imaging spectrometry. In: *Imaging Spectrometry - A Tool for Environmental Observations*, J. Hill and J. Mégier (eds.), Kluwer Academic Press, Dordrecht: pp. 57-69.

Woodcock, C.E. & Strahler, A.H. 1987. The factor of scale in remote sensing. *Remote Sensing of Environment,* **21**: 311-332.

Woodcock, C.E., Strahler, A.H. & Jupp, D.L.B. 1988a. The use of variograms in remote sensing I. Scene models and simulated images. *Remote Sensing of Environment,* **25**: 323-348.

Woodcock, C.E., Strahler, A.H. & Jupp, D.L.B. 1988b. The use of variograms in remote sensing II. Real digital images. *Remote Sensing of Environment*, **25**: 349-379.

Bibliography

Clevers, J.G.P.W., de Jong, S.M., Epema, G.F., Scholte, K., Van der Meer, F., Bakker, W.H. & Skidmore, A.K. 2000. Derivation of the red edge index using the MERIS standard band setting. *International Journal of Remote Sensing*, Submitted.

Clevers, J.G.P.W., de Jong, S.M., Epema, G.F., Scholte, K., Van der Meer, F., Bakker, W.H. & Skidmore, A.K. 1999. The use of the MERIS standard band setting for deriving the red edge index. In: *Proceedings of the ISSSR*, Las Vegas, Nevada, U.S.A..

De Jong, S.M., Scholte, K., van der Meer, F., Sommer, S. & Lacaze, B. 1998. The DAIS7915 La Peyne experiment: using airborne imaging spectrometry for land degradation survey and modeling. In: *Operational remote sensing for Sustainable Development*. G.J.A. Nieuwenhuis, R.A. Vaughan & M. Molenaar (eds.), A.A. Balkema, Rotterdam: pp. 247-253.

De Jong, S.M., van der Werff, H., van der Meer, F. & Scholte, K. 1998. The DAIS 7915 Peyne experiment: using airborne imaging spectrometry for surveying minerals in vegetated and fragmented Mediterranean landscapes. In: *1st EARSel workshop on imaging spectroscopy.* M. Schaepman, D. Schlapfer & K. Itten (eds.), Zurich, 4-6 October 1998: pp. 341-347.

Van der Meer, F., Bakker, W., Scholte, S., Skidmore, A., Clevers, J., Epema, G. & de Jong, S. 1998. ESA's medium resolution imaging spectrometer for land applications. Presented at the Fourth National Earth Science Congres (NAC IV), 7 & 8 May 1998, Veldhoven, the Netherlands.

Van der Meer, F., Bakker, W., Scholte, S., Skidmore, A., Clevers, J., Epema, G. & de Jong, S. 1998. Simulating data from ESA's Medium Resolution Imaging Spectrometer for land applications. In: *Operational remote sensing for Sustainable Development*. G.J.A. Nieuwenhuis, R.A. Vaughan & M. Molenaar (eds.), A.A. Balkema, Rotterdam: pp. 219-224.

Van der Meer, F., Scholte, K., de Jong, S. & Dorresteijn, M. 1998. Scaling to the MERIS resolution: mapping accuracy and spatial variability. In: *1st EARSel workshop on imaging spectroscopy.* M. Schaepman, D. Schlapfer & K. Itten (eds.), Zurich, 4-6 October 1998: pp. 147-153.

Van der Meer, F., Bakker, W., Scholte, K., Skidmore, A., de Jong, S., Dorresteijn, M., Clevers., J. & Epema, G. 2000. Scaling to the MERIS Resolution: mapping accuracy and spatial variability. *Geocarto International*,.15(1): 1-11.

Van der Meer, F., Bakker, W., Scholte, K., Skidmore, A., de Jong, S., M., Clevers., J. & Epema, G. 1999. MERIS potential for mapping (soil) mineralogy. *International Journal of Applied Earth Observation and Geoinformation*, In press.

Van der Meer, F., Bakker, W., Scholte, S., Skidmore, A., Clevers, J., Epema, G. & de Jong, S. 1998. ESA's Medium Resolution Imaging Spectrometer for land applications. In: *Proceedings of the 24th annual conference and exhibition of the remote sensing society,*

Developing International Connections RSS'98. P.J.A. Burt, C.H. Power & P.M. Zukowskyj (eds.), 9-11 September 1998, Greenwich, U.K.: pp. 231-237.

Van der Meer, F., Bakker, W., Scholte, K., Skidmore, A., De Jong, S., Clevers, J. & Epema, G. 1998. MERILand: potential for land applications. *Remote Sensing Nieuwsbrief*, **83**: 32-34.

Van der Meer, F., Scholte, K., de Jong, S. & Dorresteijn, M. 1999. Simulation of MERIS data: aspects of scale and variability. In: *Proceedings of the 13th Thematic Conference and Workshops on Applied Geologic Remote Sensing, ERIM.* Vancouver, Canada, 1-3 March 1999, Vol. I, pp. 142-149.

Van der Meer, F. & De Jong, S. 1999. One-day symposium Imaging Spectrometry. BCRS Nieuwsbrief 85: 59-61.

Appendix 1

MERISPEC spectral database

A1.1 Structure

A1.1.1 The logical structure

The MERISPEC (Spectral Library) database contains data on the spectral properties of different objects in the La Peyne area in southern France. The subjects vary from spectral data of pure leaves to data on surfaces covered with various objects. Three hierarchical levels are foreseen: groups, themes and layers. Groups display the highest level of objects. For example, all data related to mixed Oak Forest are grouped into group 'forest', coded 'FO'. A group can be subdivided into different themes on the basis of date of measurement. Finally, layers consist of one feature of interest, e.g. pure oak leave data is stored into layer 'focpolpu', the codes in the name read: 'forest, canopy, oak leave, pure'. Excel spreadsheets are created where all data of each object is stored.

A1.1.2 The directory structure

The logical hierarchy of data is reflected in the directory structure on the computer system. For each group a directory exists. Within a directory each theme is described in a sub-directory and hence each layer is placed in a sub-directory of a theme directory. Most directories are named with a two character code, so forest data will be stored in directory 'FO' of the reference environment of the system. This 'FO' directory contains two subdirectory '1606' and '1806' which are, in turn, subdivided into directories containing the layer information (Table 1).

A1.2. The Forest Group

Spectral measurements of mixed Oak Forest yield input in this group.

A1.2.1 The 1606 Theme

Data of canopy and litter of a mixed Oak Forest site, measured on the 16th of June 1998, are put into this directory. Data on pure samples as well as real canopy measurements are available.

Layer name	Description
Focpqi	Forest, canopy, Quercus ilex
Foliqitw	Forest, litter, Quercus ilex, twigs
Focppi	Forest, canopy, pine
Folipitw	Forest, litter, pine twigs
Foliqismde	Forest, litter, Quercus ilex, stem, dead
Foli	Forest, litter
Focpqipu	Forest, canopy, Quercus ilex leave, pure
Foliqilede	Forest, litter, Quercus ilex, leaves, dead
Foslwe	Forest, slate, weathered
Foqzwe	Forest, quarts, weathered

A1.2.2 The 1906 Theme

The following canopy species are collected on the 19th of June 1998: *Quercus pubescens*, *Quercus ilex*, *arbutus unedo* and a pinus species.

Layer name	Description
Focpqi	forest, canopy, Quercus ilex
Fpcpqipu	forest, canopy, Quercus ilex, pure
Focpqp	forest, canopy, Quercus pubescens
Focpqppu	forest, canopy, Quercus pubescens, pure
Foliqileye	forest litter, Quercus ilex, leave, yellow
Foliqilebr	forest litter, Quercus ilex, leave, brown
Fobawe	forest, basalt, weathered
Fomogr	forest, moss, green
Foba	forest, basalt, small piece

A1.3. The Garrigue Group

Spectral measurements at different sites in the study area covered by a garrigue type of forest are stored into this directory.

A1.3.1 The 1806 Theme

The different shrubs, herbs and surface materials measured are the following:

Layer names	Description
Gacpau	garrigue, canopy, arbutus unedo
Gacpqi	garrigue, canopy, Quercus ilex
Gahegs	garrigue, herbs, grass
Gashqi	garrigue, shrubs, Quercus ilex
Gashau	garrigue, shrubs, arbutus unedo
Gasher	garrigue, shrubs, Erica arboreta
Galitwqide	garrigue, litter, twigs, Quercus ilex, dead

A1.3.2 The 1906 theme

Layer names	Description
Gashpi	garrigue, shrubs, pine
Gashqi	garrigue, shrubs, Quercus ilex
Gashau	garrigue, shrubs, Arbutus unedo
Gaheer	garrigue, herbs, Erica arborea
Gahepf	garrigue, herbs, purple flowers
Galitwqide	garrigue, litter, twigs, Quercus ilex, dead
Gahegs	garrigue, herbs, grass
Gasust	garrigue, surface, stoney
Gasu	garrigue, surface (red soil, twigs, stones)

A1.3.3 The 2106 Theme

Layer names	description
Gashpigr	garrigue, shrubs, pine, green
Gashpism	garrigue, shrubs, pine, small pieces
Gashqi	garrigue, shrubs, Quercus ilex
Gasherfl	garrigue, shrubs, Erica arborea, flowers
Gasherflye	garrigue, shrubs, Erica arborea, flowers, yellow
Gasherflgr	garrigue, shrubs, Erica arborea, flowers, green
Gashbltw	garrigue, shrubs, blackberry, twigs
Gashblle	garrigue, shrubs, blackberry, leave
Gashblbl	garrigue, shrubs, blackberry, blossom
Gahepf	garrigue, herbs, purple flower

A1.3.4 The 2306 Theme

Layer names	Description
Gacpqi	Garrigue, canopy, Quercus ilex
Gacppi	Garrigue, canopy, pine
Gasherye	Garrigue, shurbs, Erica arborea, yellow
Gashergr	Garrigue, shrubs, Erica arborea, green
Galimogb	Garrigue, shurbs, Erica arborea, greenbrown

GROUP	THEME directories			Layers and support data
FO (Forest)			1606	Focpqi, foliqitw, focppi, folipitw, foliqismde, foli, focpqipu, foliqilede, foslwe, foqzwe
			1906	focpqi, fpcpqipu, focpqp, focpqppu, foliqileye, foliqilebr, fobawe, fomogr, foba
GA (Garrigue)			1806	gacpau, gacpqi, gahegs, gashqi, gashau, gasher, galitwqide
			1906	gashpi, gashqi, gashau, gaheer, gahepf, galitwqide, gahegs, gasust, gasu
			2106	gashpigr, gashpism, gashqi, gasherfl, gasherflye, gasherflgr, gashbltw, gashblle, gashblbl, gahepf
			2306	gacpqi, gacppi, gasherye, gashergr, galimogb
MA (Maquis)			1706	masherflye, mashertwde, mashertwgr, macpqi, mashpi, macpau, macpaulegr
			2106	macpoa1, macpao2, macpao3, macpao4, macpao4_2, d174, mali, maliaosm, masa, mabawe, malimoge, malimogg, malimodg
OT (Other)			1706	erflde, erflye, ersmgr
	TR (Transect)			gatr1906, rfbs0207, rfbs2006, rfvi0207, vivi, bsvi
RF (Reference)	FO (forest)			rffocpau1, rffocpqp, rffocpau2, rffocpqi, rffocppi, rffoqilede, rffotwqide
	GA (Garrigue)			rfgashau1, rfgasher, rfgalimodg, rfgalimolg, rfgahegsye, rfgashau2, rfgashqi, rfgahegs
	RF (reference)			rfbs
	ST (stones)			rfstbx, rfstdo, rfstco, rfstas
	WA (water)			rfwas1, rfwava1, rfwava2, rfwava3
			2006	rfbs
ST (Stones)	BA (Basalt)	FR (Fresh)		bafrmt, bafrpa, bafrro, bafrtt
		OT (Other)		bamo
		WH (Weathered)		bawhmt, bawhpa, bawhro, bawhtt, babe
	BX (Bauxite)	BC (Blanc)		bxbcbr, bxbcmi
		TR (Transect)	1906	bxmitr
			2906	bxmitr
		WH (Weathered)		bxbe, bxcrmi, bxmubr, bxremi, bxwimi
	CA (Carbon)			cacabe, cagebe
	CU (Copper)	FR (Fresh)		cufrye
		TR (Transect)		cutr
		WH (Weathered)		cuwhye
	DO (Dolomite)	FR (Fresh)		dofrcimr, dofrd8mr, dofrmi, dofrmi.xls
		MO (Moss)		domoor, domowi, domobk
		TR (Transect)	2306	domitr, domitr.xls
			2906	domitr, domitr.xls
		WH (Weathered)		dowhcimr, dowhd8mr, dobe, dosuwm
	FY (Flysch)	FR (Fresh)		flscfr, fyfrbe
		WH (Weathered)		flscwh, fywhbe
	GI (Gneiss)			gibe
	LM (Lime)	FR (Fresh)		lifrcr
		WH (Weathered)		liwhcr
	LS (Limestone)	FR (Fresh)		lsfrbr, lsfrmu, lsfrvs
		WH (Weathered)		lsbe, lswhbr, lswhmu, lswhvs
	QZ (Quarzite)			qzva
	SL (Slate)	FR (Fresh)		slfrbr
		RU (Rusty)		slrubr
		WH (Weathered)		slwhhbr, slwhva
	SS (Sandstone)	FR (Fresh)		ssfrva
		WH (Weathered)		sswhva1, sswhva2, ssyemi
	TU (Tuff)	FR (Fresh)		tufrco, tufrd146
		WH (Weathered)		tuwhco, tuwhd146
VI (Vine)			1706	vivitr, vibstr, vilegr, vigpgr, vivijs, vibsjs
			2006	vivirf, vibsrf, vismrf, vigpgrrf
	AS (Astruc)			vivias, vibsas, visaas

Table 1. MERISPEC database structure and content.

A1.4 The Maquis Group

Two different maquis type of forest sitets are recognized in the field and the collected spectral measurements are put in this group.

A1.4.1 The 1706 Theme

Layer names	Description
Masherflye	maquis, shrubs, Erica arborea, flowers, yellow
Mashertwde	maquis, shrubs, Erica arborea, twigs, dead
Mashertwgr	maquis, shrubs, Erica arborea, twigs, green
Macpqi	maquis, canopy, Quercus ilex
Mashpi	maquis, shrubs, pine
Macpau	maquis, canopy, arbutus unedo
Macpaulegr	maquis, canopy, arbutus unedo, leaf, green

A1.4.2 The 2106 Theme

Layer names	Description
Macpoa1	maquis, canopy,
Macpoa2	maquis, canopy,
Macpoa3	maquis, canopy,
Macpoa4	maquis, canopy,
Macpoa4_2	maquis, canopy,
D146	maquis, dark asphalt
Mali	maquis, litter
Maliaosm	maquis, litter, oak stem
Masa	maquis, shade
Mabawe	maquis, basalt, weathered
Malimoge	maquis, litter, moss, grey
Malimolge	maquis, litter, moss, ligth-grey
Malimogg	maquis, litter, moss, greygreen
Malimodg	maquis, litter, moss, darkgreen

Appendix 2

Geometric Correction of DAIS-7915 data

A2.1 Introduction

Within the framework of the Meriland project in many examples positional accuracy was needed to link the field observations to results derived from the DAIS data and simulated MERIS data; hence the DAIS images should be geocorrected to an accuracy of a few pixels. nlike satellite images, airborne images are influenced by roll, pitch yaw, velocity and direction changes of the moving platform. Registration to a map base using classical control point registration methods with polynomial image warping in this case does not generally result in geometrically well corrected images. Investigations by Meyer (1994) and Clark *et al.* (1998) have shown that the use of gyroscopic flight data and Digital Elevation Models (DEM) is essential. Meyer (1994) designed and implemented a procedure for geocoding Airborne Visible / Infrared Spectrometer (AVIRIS) data in rugged terrain in Switzerland. To correct for the unstable flight line, the attitude movements, and the topographic distortions, a parametric approach was developed which does not require ground control points (GCPs) input and can be applied without human interaction. To achieve reliable geometric accuracy, both a radar tracking system data and a digital elevation model are required. In general the results showed good correspondence between digitised maps and image data with a mean RMS-error ranging from 0.12 pixel (2m) to 0.19 (4m).

The DAIS was flown (Figure 1 shows the strip used) on a Dornier 228 TwinProp at approximately 3km altitude in the La Peyne area. In the aircraft three gyroscopes are mounted to collect data on the yaw, roll and pitch. Due to failure of one of the gyroscopes during the first flight, detailed aircraft data was not available. The question was therefore whether in the absence of these data, acceptable georeferencing and resampling of the image was possible. The only way to achieve a good geometric correction of the DAIS image is through the selection of a set of GCPs. Initial attempts at geometric correction using GCPs and 1st to 3rd order standard polynomial transformations proved unsatisfactory. Obviously, aircraft movements, such as pitch, yaw, roll and altitude and course changes, lead to more complex image transformations than can be handled by these standard procedures. Therefore, a new method was developed which only requires a set of GCPs, associated with the image pixel positions. The method is based on a geostatistical analysis and subsequent kriging of the residual positional error in the GCP data set after a standard affine transformation. Because this error is a two-dimensional vector, the analysis has to be applied applied in two directions. The kriging process of the residual error vectors leads to a good insight into the deviations caused by the actual flight track. Furthermore, a larger secondary set of kriged GCPs can be

generated, from which an improved image geocorrection can be obtained through standard methods.

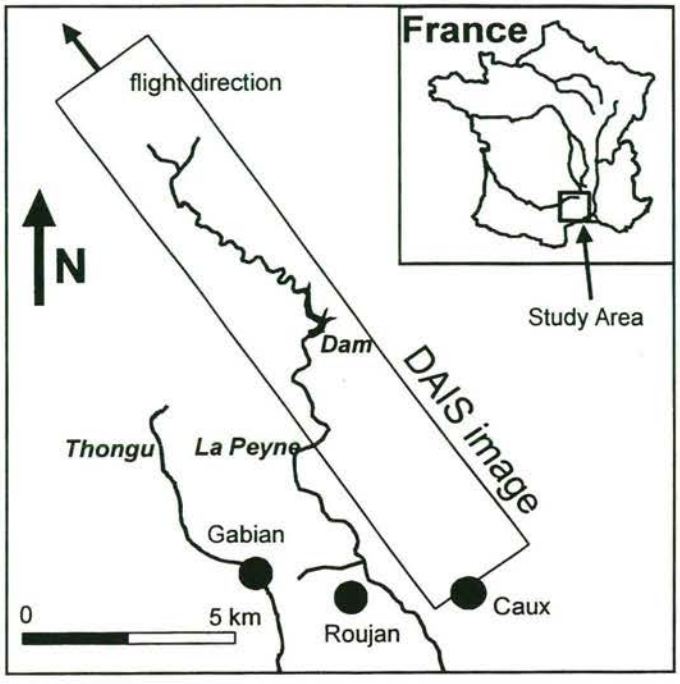

Figure 1. Location map showing the DAIS strip along the Peyne River catchment.

A2.2 Theory and methods

A2.2.1 Geometric correction; current practice

The most commonly applied method to correct for geometric distortion is by comparing the position of specific points in the image with the corresponding co-ordinates of these points on a map (GCPs). Based on a selection of points (normally between 4-10) geometric transformation functions can be computed and used to fit the image on the map co-ordinates. For satellite imagery first order geometric transformation functions are sufficient, while airborne images in general require higher order transformations. The next step is then to compute DN values for the newly defined image grid. As this grid will generally not fit exactly on the old pixel positions, an interpolation of the DN values is usually required. Several methods are available for the final resampling process.

To understand application of geostatistics in the present context of geometric correction, a good understanding is required of the different error categories leading to both systematic and random deviations.

1. **Airplane**: As described by Clark *et al.* (1998) navigation data show that pitch (direction of the nose of the plane up and down) and yaw (direction of the nose to the left or right) vary by a couple of degrees on a typical flight. Roll around the aircraft axis in the direction of the flight is typically less than a degree. Variations in aircraft altitude and velocity (relative to the cross-track scanner sampling velocity) produce aspect-ratio differences in the image pixel size. Finally, deviations from the set course may lead to substantial image distortion.
2. **Elevation ground / Sensor angle**: The distance from the aircraft to the ground is not constant in most environments due to topography and when viewing off-nadir (Figure 2.). An increasing or decreasing distance from the scanning mirror sensor to the land surface

causes a shift in the total cross track distance. Both effects are significant and require correction even if the aircraft stability and motions were ideal.

3. **Location error** : A number of errors occur due to map inaccuracies, uncertainty in GPS co-ordinate acquisition and identification of points on maps and images.

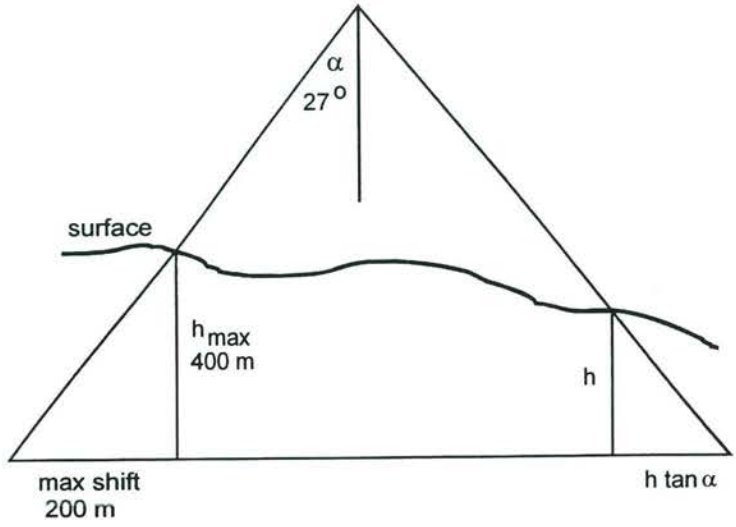

Figure 2. Geometric errors due to DAIS scanning mirror sensor and elevation differences.

DAIS is flown about 3 km altitude with cross-track scanlines of 512 pixels. Scanline length is about 3 km. The altitude of the study area varies from about 100m to 450m above sealevel. Hence the scan angle α is 27° with a maximum possible shift of about 200 m , or 30 pixels (see Figure 2).

A2.2.2 Geostatistical approach

As discussed in the previous section, the errors are due to (1) airplane motion, (2) elevation differences in the scanned area and (3) errors in location of ground control points. The crucial question to be studied in the present geostatistical analysis is whether the three categories of errors can be thought of as a single set of errors, i.e. as spatially coherent set with a distinct sill and range, applicable to both x- and y-coordinates. Obviously the spatial correlation of the errors due to airplane motion (1) is different from the error correlation caused by location of ground control points (3). However, in view of the absence of data on airplane motion and terrain elevation, it is not possible to make an *a priori* distinction between the three error categories.

A set of 124 GCP's were collected from 1:25000 topographical maps of the study area (Lambert UTM, 3615, 2643 and 2543 IGN, 1990) and registered on the DAIS image. The three topographical maps were scanned, georectified and glued. Inspection of the map joints revealed errors of up to 25 m (4 pixels) as a result of the joining process and inaccuracies in the maps. The root mean square error σ is defined as:

$$\sigma = \sqrt{\frac{\sum (x_i - \xi_i)^2 + \sum (y_i - \eta_i)^2}{2(n - df)}}$$

where (x_i,y_i) are the map (GCP) coordinates, (ξ_i,η_i) the image coordinates, n the number of tie points and df the degrees of freedom associated with the transformation method (for example, df=3 for a standard affine transformation). Table 1 summarizes the results obtained with standard transformations.

Table 1. Summary of results obtained with standard transformations.

number of GCPs	origin	transformation	RMS (pixels)
124	map	affine	34
124	map	2nd order bilinear	17
124	map	3rd order	14

The results of Table 1 illustrate the generally large errors obtained with standard transformations. The complexity of image corrections due to airplane motion leads to the need for a different type of analysis.

A scatter plot of the errors in x and y co-ordinates after a standard affine transformation (Figure 3a) shows a directional dependence of the errors: in a direction perpendicular to the flight, the errors are much larger than in the direction parallel to the airplane track. Analysis of the spatial correlation produced semi-variograms like Figure 4, showing the presence of a trend. The errors were therefore rotated in such a way that the average flight direction is pointing along the y-axis (Figure 3b). The new error y co-ordinates are now those parallel to the average course, whereas the new x co-ordinates correspond to errors perpendicular to the flight direction. The semi-variogram analysis of the rotated x-errors (Figure 4) again clearly shows the presence of a trend in the data. This trend is shown in Figure 5 as a V-shaped line, when the perpendicular error set is plotted as a function of the distance along the track. It probably represents the plane's actual track, possibly coupled with a roll correction.

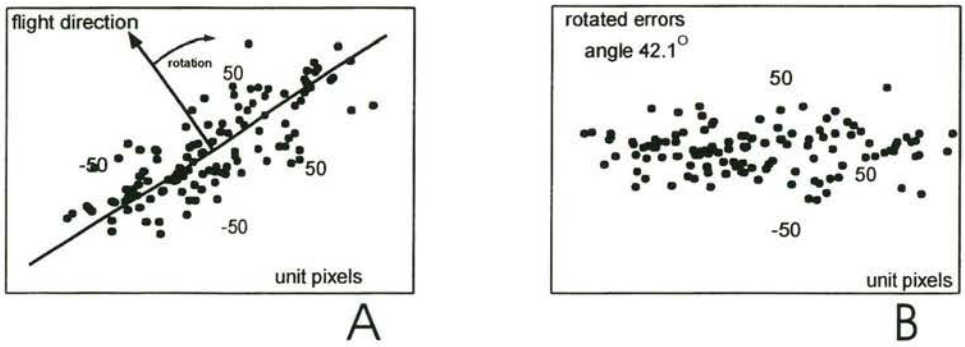

Figure 3. (A) Residual errors in x- and y-direction after affine transformation and (B) residual errors rotated by 42.1 degrees into directions parallel and perpendicular to the average flight direction.

After correction for this V-shaped linear trend, an error set was found with a clear spatial correlation. Figure 6 summarizes the results. In the parallel direction a gaussian semi-variogram was found with nugget 0, range 250 pixels and sill 300 px^2, whereas in the perpendicular direction a gaussian variogram was found with the same nugget and range. However, in the latter case a higher sill of 500 px^2 was determined. Finally, the cross-variogram shows that the two error sets are independent. The semi-variograms of Figure 6 justify application of ordinary kriging in two directions. At short range there is a distinct spatial correlation in the residual errors, whereas there is a trend in the errors perpendicular to the course. This trend, however, can be taken into account by application of ordinary kriging with a limited search radius. The error rotation has shown that in the present case the trend effect mainly affects the perpendicular error set. After removal of the trend, the spatial

correlation of the errors is nearly identical to that of the parallel error set, for which no trend removal was required.

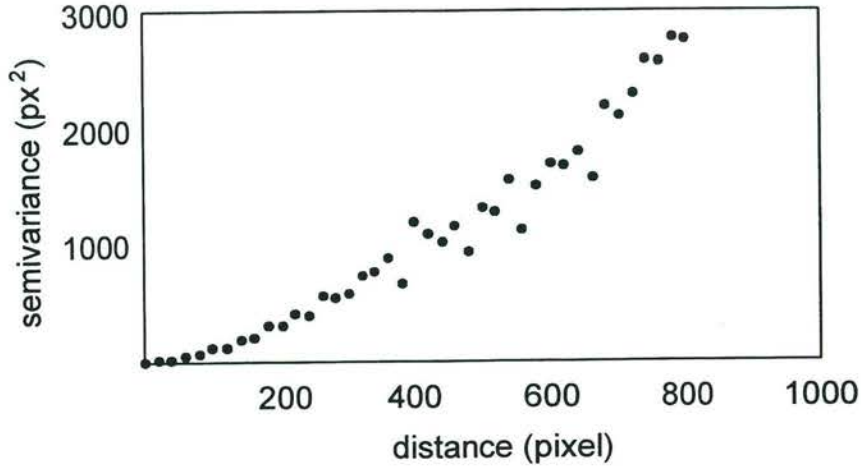

Figure 4. Semi-variogram of the rotated residual error perpendicular to the flight direction.

As is mentioned above aircraft data require higher order transformations and hence more assumes that the spatial variation of any variable can be expressed as the sum of three major components: (1) structural component (mean or constant trend), (2) random spatially correlated component and (3) random noise. The conditions, involved in this method, stationarity of difference and variance of differences, define the intrinsic hypothesis of the regionalized variable theory. This means that once structural effects have been accounted for, the remaining variation is homogeneous in its variation so that differences between sites are a merely a function of the distance between them. If the conditions specified by the intrinsic hypothesis are fulfilled, than the semivariance can be estimated from sample data. A plot of the semivariance against the distance is known as the experimental variogram. The variogram is an essential step on the way to determining optimal weights for interpolation. In the simples possible situation only three known GCPs (1, 2 and 3) will be used to make a kriged estimate of a GCP value at point p. Three weights, w_1, w_2 and w_3 (which sum up to 1) must be found, resulting in four equations with three unknown results. The lagrange multiplier, Ψ, is added to ensure that the resulting set of weights has the minimum possible estimation error. The complete set of simultaneous equations has the following appearance:

$$w_1\gamma(h_{11}) + w_2\gamma(h_{12}) + w_3\gamma(h_{13}) + \Psi = \gamma(h_{1p})$$
$$w_1\gamma(h_{12}) + w_2\gamma(h_{22}) + w_3\gamma(h_{23}) + \Psi = \gamma(h_{2p})$$
$$w_1\gamma(h_{13}) + w_2\gamma(h_{23}) + w_3\gamma(h_{33}) + \Psi = \gamma(h_{3p})$$
$$w_1 + w_2 + w_3 + 0 = 1$$

The first step carried out is a matrix inversion, to define the set of weights that minimize the error variance. This is often referred to as the ordinary kriging system , and this can be written in matrix notation as

$$C * w = D$$

where C is the covariance matrix of the observations and D is the covariance matrix for the estimated points versus the observables.

$$\begin{bmatrix} C_{11} & \dots & C_{1n} & 1 \\ . & \dots & . & . \\ C_{n1} & \dots & C_{nn} & 1 \\ 1 & \dots & 1 & 0 \end{bmatrix} * \begin{bmatrix} w_1 \\ . \\ w_n \\ \mu \end{bmatrix} = \begin{bmatrix} C_{10} \\ . \\ C_{n0} \\ 1 \end{bmatrix}$$

To solve for the weights, the equation is multiplied on both sides by C^{-1}, the inverse of the left-hand side covariance matrix:

$$C * w = D$$

$$C^{-1} * C * w = C^{-1} * D$$

$$I * w = C^{-1} * D$$

$$w = C^{-1} * D$$

Moving Neighbourhood Kriging is similar to ordinary kriging, it only does not assume that the random variables in the random function model all have the same mean and variance. Moving Neighbourhood kriging uses a search radius to try to have the mean residual error (ε_r) equal to zero and aims to minimize the variance of the error (σ^2_r) of point measurement predictions. These assumptions allow us to develop a relationship between the model variogram and the model covariance. In terms of the variogram the kriging system can be written as

$$\gamma_{i0} = \sum_{j=1}^{n} w_j \gamma_{ij} + \mu \qquad \forall i = 1,\ldots,n$$

with the modelled error variance given by

$$\sigma_r^2 = \sum_{i=1}^{n} w_i \gamma_{i0} + \mu$$

Using the variogram co-ordinates can be predicted for unsampled locations. This is done in a two steps. First the X-co-ordinates are predicted, then the Y co-ordinates. By calculating the resulting vector from the X and Y co-ordinate values the resulting GCP file is created.

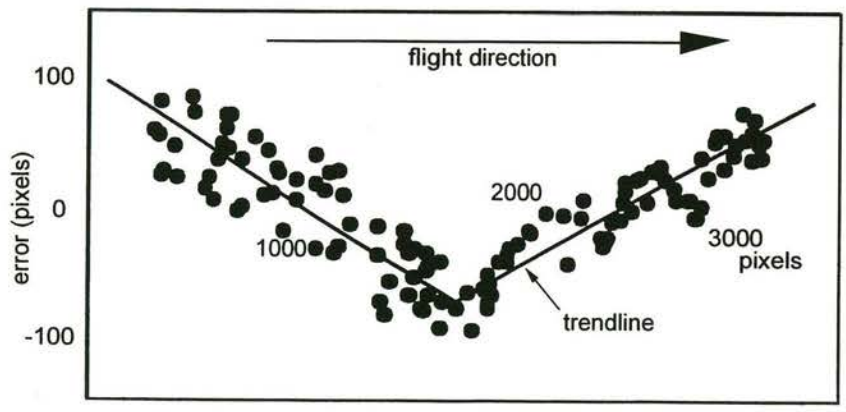

Figure 5. V-shaped trend in the errors perpendicular to the flight direction.

Under the assumption that the gaussian semi-variogram model applies to both x- and y-coordinates, the data can now be kriged independently in both directions by applying ordinary kriging methods with a limited search radius to account for long range trend effects. A special program was written in Delphi 4 Pascal to implement the two-dimensional aspects of the analysis. The search radius was established at 250 pixels (about 1500 m) after several trials. Figure 7 shows the resulting two-dimensional error pattern on a regular grid, where the arrows indicate the direction of the correction vectors in the different parts of the image. The figure shows quite convincingly the complex nature of the shifts required to map the image pixels back to UTM coordinates, as a result of two turns in the flight path, the first one probably bringing it off course and the second one bringing it back on course. It is not clear

whether the first was due to changing wind speed or inadvertent course changes by the pilot. However, the kriging process maps the necessary image corrections very neatly.

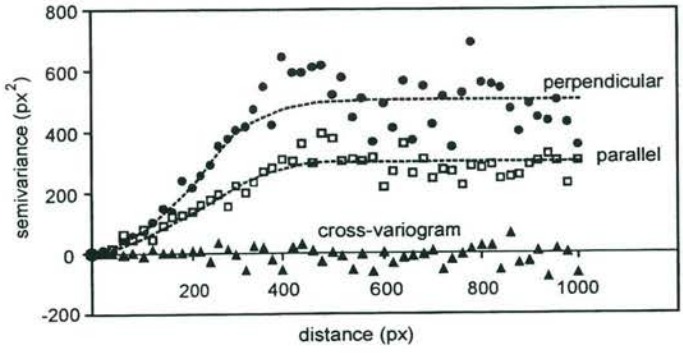

Figure 6. Semi-variogram of the errors parallel and perpendicular to the flight direction. In both directions a gaussian semi-variogram is found. The cross-variogram indicates that the two error sets are spatially independent.

To verify the results and to obtain an independent estimate of the accuracy of the method a second set of 55 ground control points was obtained with a differential GPS instrument (2-10 m accuracy). The corresponding image pixels were kriged in the same way as before, leading to a set of 55 corrected UTM coordinates. These were then compared with the GPS coordinates, producing a root mean square error of 5 pixels (about 30 m) with a factor 3 improvement on the 3rd order transformation. It should be noted that this is a rigorous test, because the coordinates of the original set of 124 GCP's were taken from the glued topographical maps, which have their own errors as mentioned before.

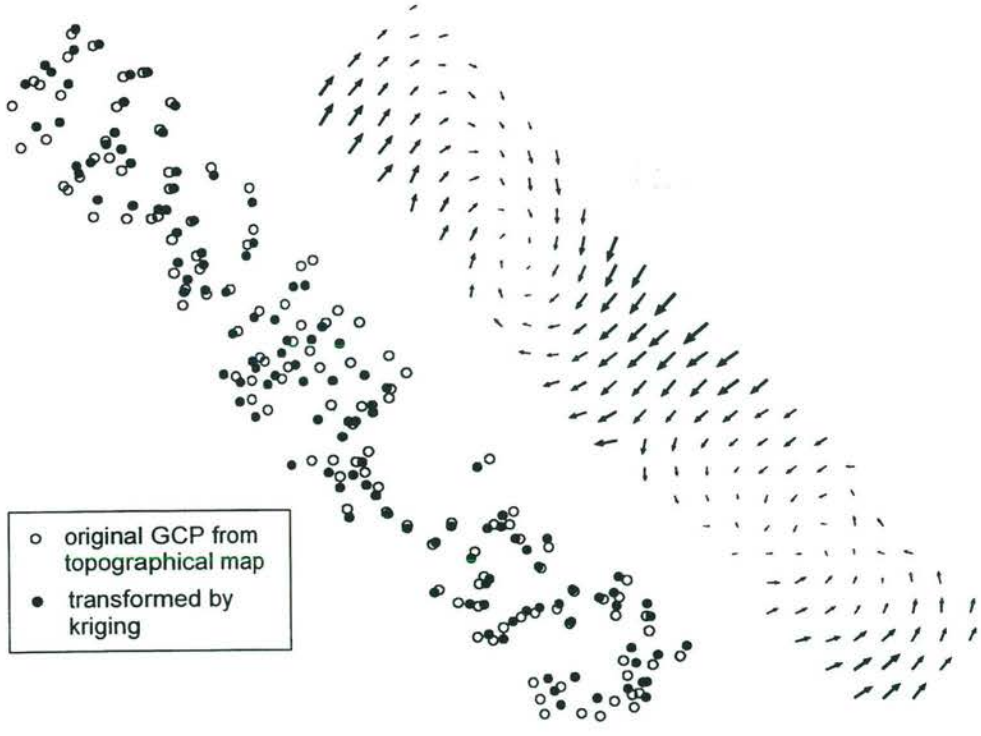

Figure 7. Left hand figure shows the original set of 124 GCPs together with the points corrected by kriging. The right hand figure shows the kriged correction vectors on a regular grid.

As a final step, resampling of the image is required to produce an accurate geometric restoration. This can be done in several ways. For example, the method described here can be used to generate a large number of grid control points with corrected coordinates after which standard resampling methods may be applied. It also seems possible to resample the image directly through the geostatistical transformation procedure, although some further smoothing may then be required. Figure 8 shows an example of the image corrected through generation of a large number of corrected grid points.

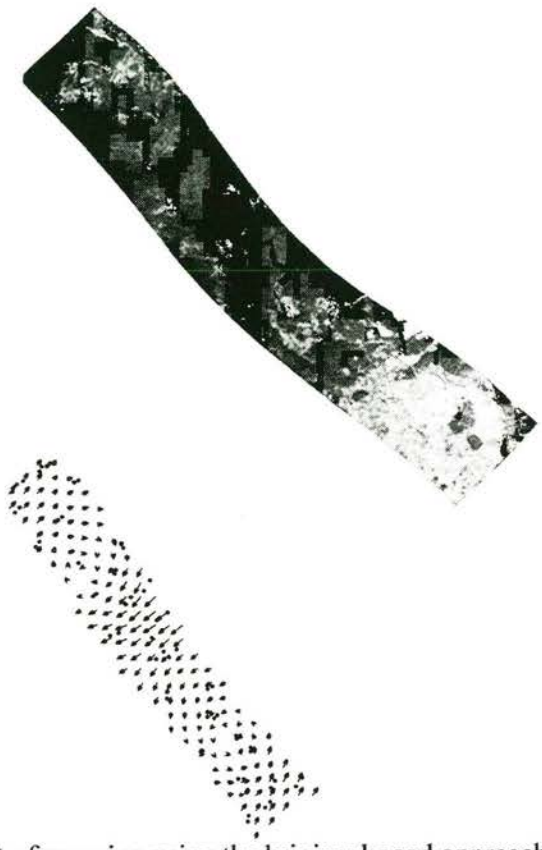

Figure 8. Result of warping using the kriging-based approach (color plate 10).

A2.3 Conclusions

The analysis has shown that reasonable image correction is possible, even under the difficult circumstances of images produced by a cross-track scanning mirror sensor on board of an aircraft flying at low altitude without navigational data and without a digital elevation map.
The bivariate kriging method described here, strictly uses a set of ground Control Points (GCPs). However, this type of approach can only be successful if the aircraft's deviation from a straight course and its attitude movements are relatively small the set of Ground Control Points represent terrain elevation sufficiently close. It follows that in rugged mountainous terrain and/or with sudden aircraft movements, these conditions would probably not be met.

In the present case, the semivariogram analysis of the residual error set has convincingly shown that the combination of errors due to flight and terrain may be described by independent gaussian models for directions parallel and perpendicular to the aircraft's average course. These variogram models can therefore be applied successfully in predicting the spatial error at any pixel position through ordinary kriging. It was shown through the use of an independent DGPS control set that the error was reduced by a factor 3 as compared to a 3rd order standard tiepoint method . In general this method could also be applied to orthophoto

correction when only a set of GCPs is available. Again the condition is that the ground control points should adequately represent the terrain. Further theoretical extension of this bivariate kriging method may be required, for example in the case where the semivariograms and the cross-variogram indicate that the error sets are not independent.

Appendix 3

Color plates

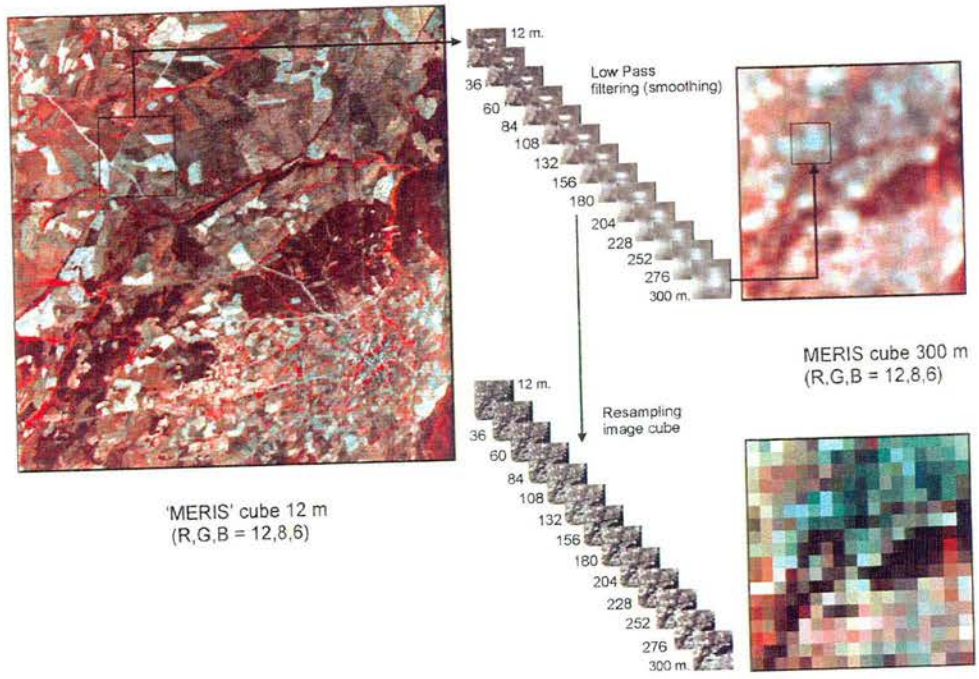

Color plate 1. Figure 6 of Chapter 3

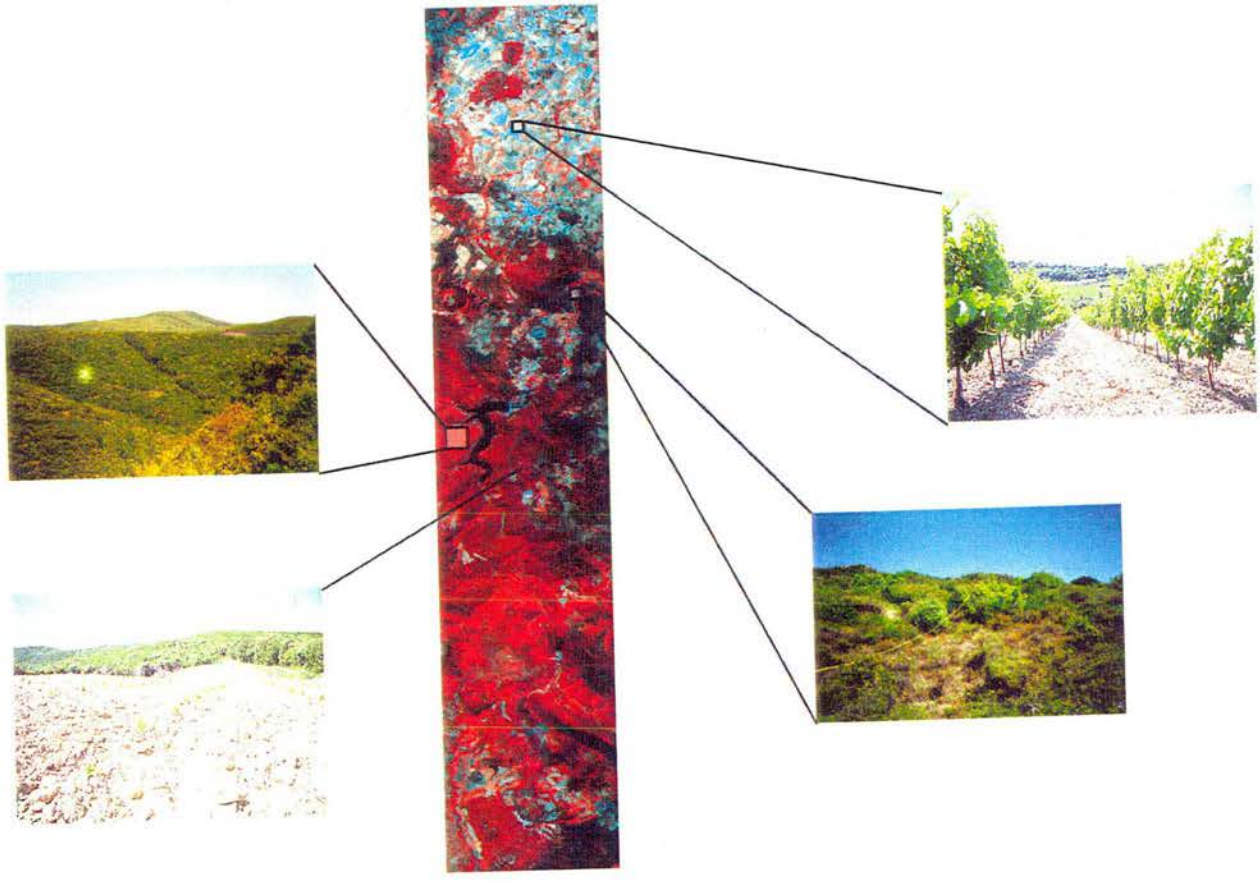

Color plate 2. Figure 4 of Chapter 4.

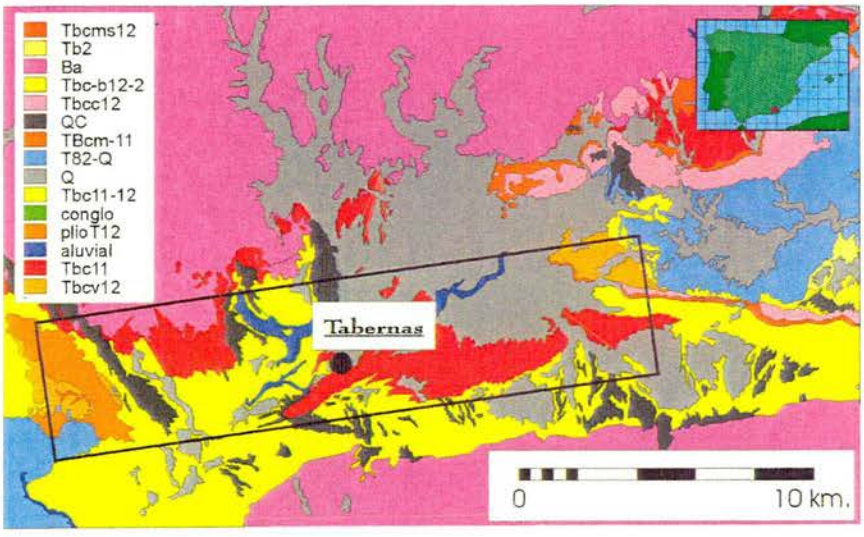

Color plate 3. Figure 2 of Chapter 5.

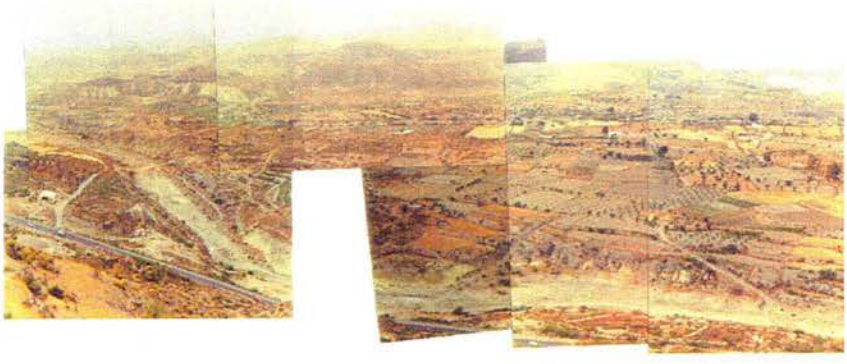

Color plate 4. Figure 3 of Chapter 5.

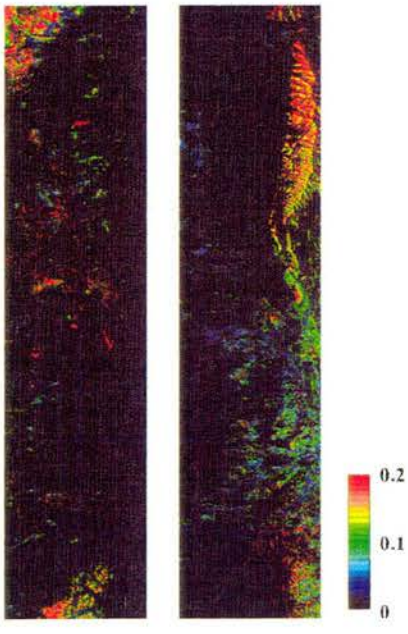

Color plate 5. Figure 6 of Chapter 5.

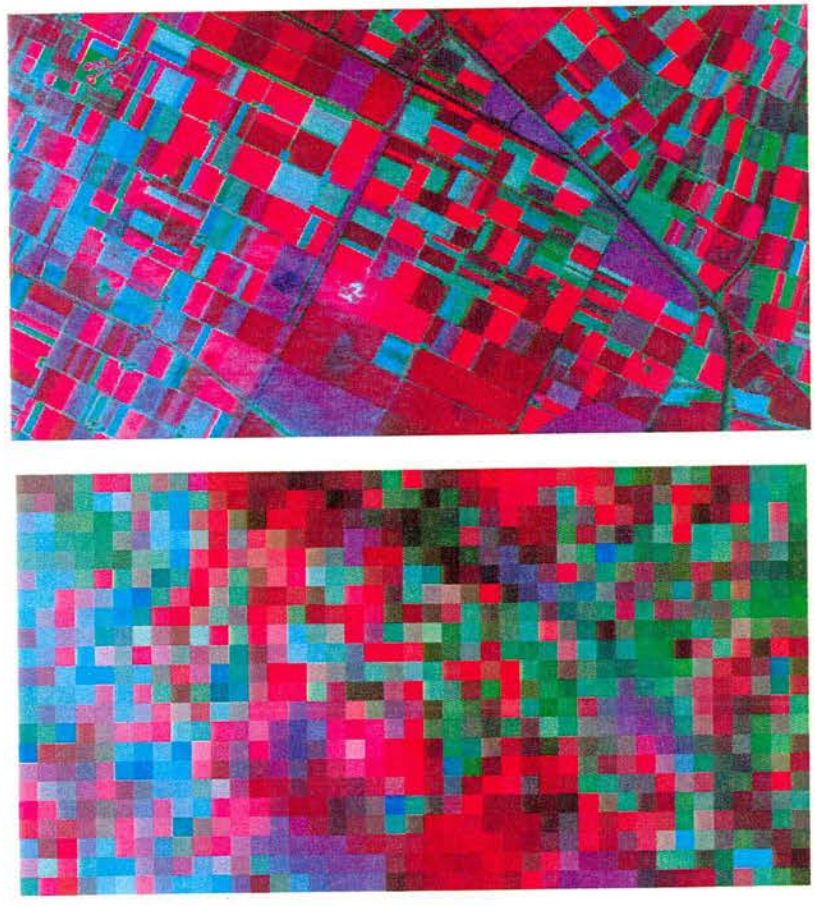

Color plate 8. Figure 11 of Chapter 7.

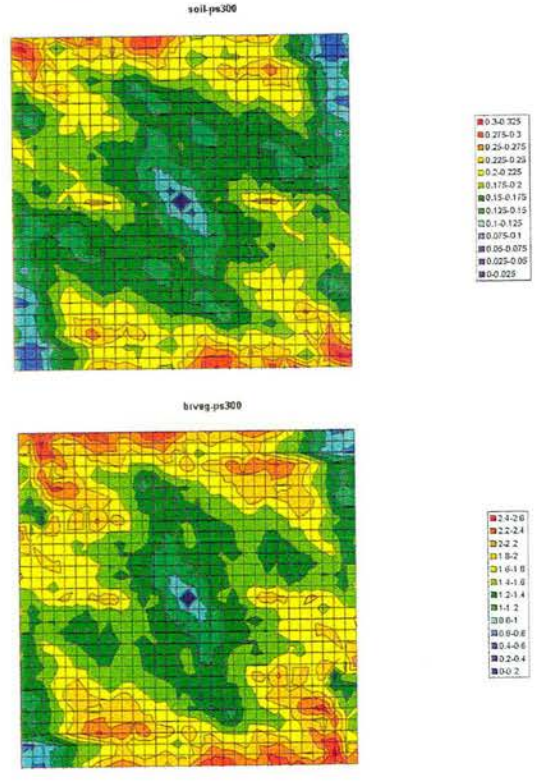

Color plate 9. Figure 6 of Chapter 8.

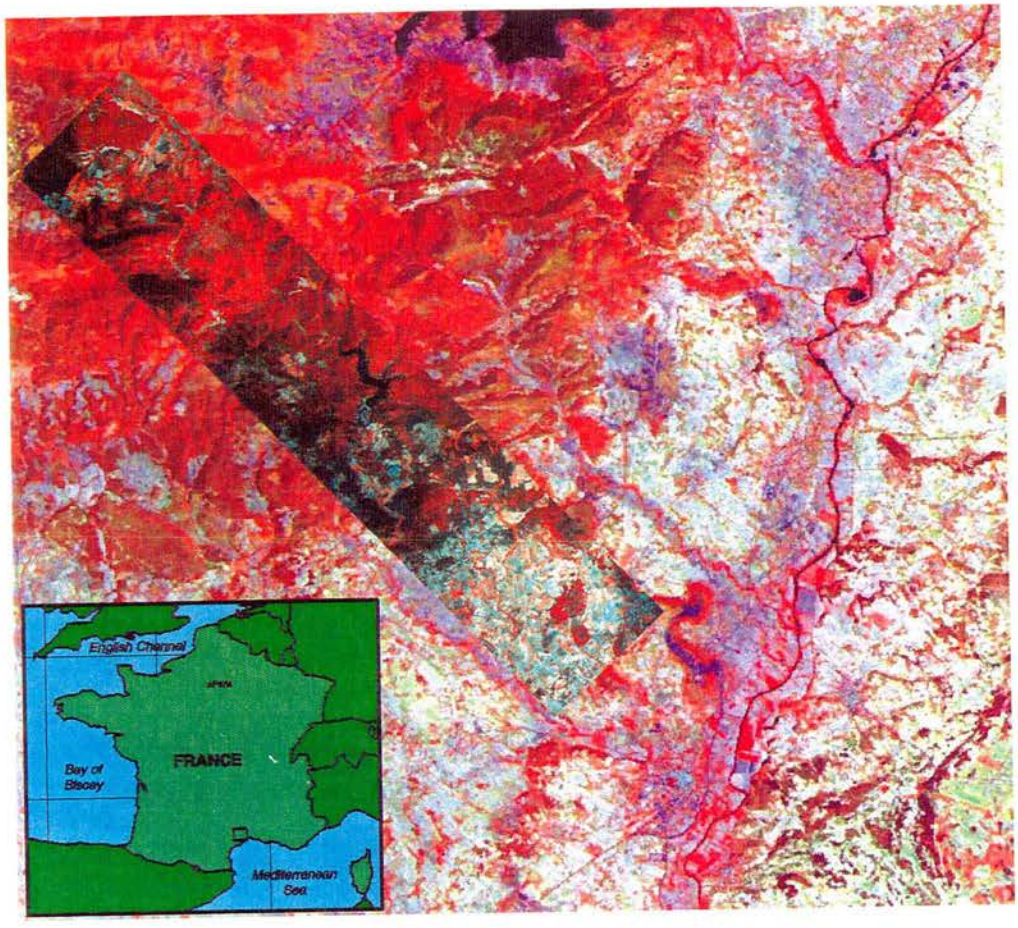

Color plate 6. Figure 1 of Chapter 6.

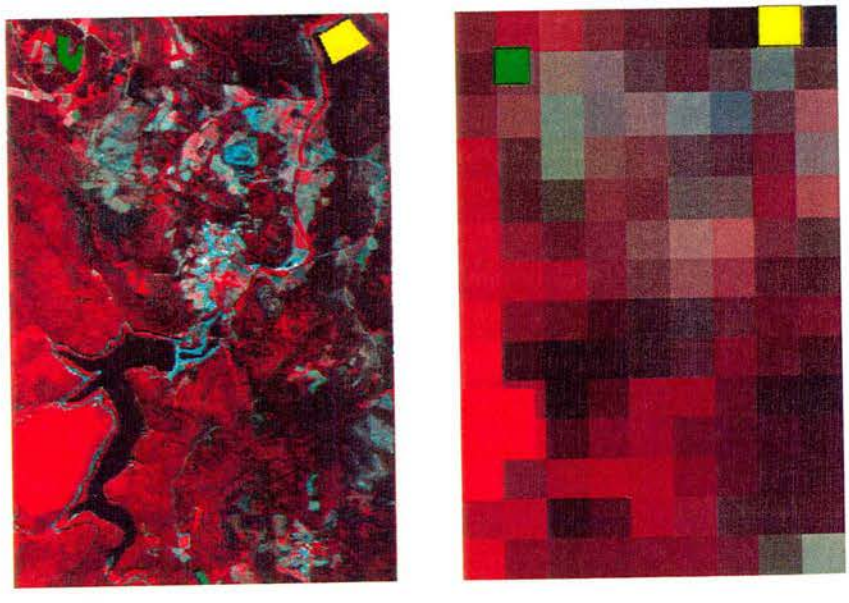

Color plate 7. Figure 2 of Chapter 6.

Color plate 10. Figure 8 of Appendix 2.

The User Support Programme 1996-2005 (USP-2) is implemented under the responsibility of the Netherlands Remote Sensing Board (BCRS) and the Space Research Organization of The Netherlands (SRON).

The objectives of the USP-2 are: to support Dutch users of information from future European earth observation systems in the development of applications for operational and scientific use; to develop the required national infrastructure and to support users in developing countries with applications for the purpose of sustainable development, in connection with activities carried out by ESA and EUMETSAT.

The USP-2 is financed from the national space budget. During the period 1996-2000 the USP-2 element under the responsibility of the BCRS is executed in connection with the National Remote Sensing Programme 1996-2000.

Publication of:

Netherlands Remote Sensing Board (BCRS)
Programme Bureau
Rijkswaterstaat Survey Department

P.O. Box 5023
2600 GA Delft
The Netherlands
Tel.: +31 (15) 269 11 11
Fax: +31 (15) 261 89 62
E-mail: p.b.bcrs@mdi.rws.minvenw.nl
BCRS homepage: http://www.minvenw.nl/rws/mdi/bcrs